1290

UNIVERSIDADE D
COIMBRA

Babar Mujtaba

ROCK FRAGMENTS AND SURFACE-SUBSURFACE HYDROLOGICAL PROCESSES AT PLOT AND HILLSLOPE SCALES: LABORATORY AND NUMERICAL SIMULATIONS

Doctoral Thesis in Civil Engineering, Hydraulics, Water Resources and Environment, supervised by Professor João Luís Mendes Pedroso de Lima and submitted to the Department of Civil Engineering of the Faculty of Sciences and Technology, University of Coimbra.

December 2021

FCTUC DEPARTAMENTO DE ENGENHARIA CIVIL
FACULDADE DE CIÊNCIAS E TECNOLOGIA
UNIVERSIDADE DE COIMBRA

Rock fragments and surface-subsurface hydrological processes at plot and hillslope scales: Laboratory and numerical simulations

Babar Mujtaba

Doctoral Thesis in Civil Engineering, Hydraulics, Water Resources and Environment, supervised by Professor João Luís Mendes Pedroso de Lima and submitted to the Department of Civil Engineering of the Faculty of Sciences and Technology, University of Coimbra.

December 2021

“Only a few know,

how much one must know

to know how little, one knows”

- Werner Heisenberg

Acknowledgements

I would like to express my appreciation and respect to my supervisor, Professor João Pedroso de Lima, whose knowledge, creativity and resourcefulness nurtured my interest in scientific research and in the interesting field of hydrology. Professor João directly contributed to my success, providing me the much-needed guidance and support.

To Professor Isabel Pedroso de Lima, I am thankful for her effort, positive criticism, and patience. I would never be a good researcher without Professor Isabel's help. My sincere thanks also go to Doctor Ladislav Holko and Doctor Hana Hlaváčiková from Institute of Hydrology, Slovak republic, for providing their valuable knowledge and guidance, which was vital for the achievement of this thesis.

I am also thankful for the positive environment given by all the professors, researchers, and colleagues of the research lab I was part of in the University of Coimbra. To Professor José Lopes de Almeida, Professor Alexandre Silveira and Professor Rita Fernandes de Carvalho, for the expertise and motivation they gave me in all these years. To Cleene, Lara Santos, Marcelle, Mihaela for their help in the laboratory experiments. To Rafael, Mousinho and Nazmul for their friendship and fun moments. To the laboratory technician Mr. Joaquim Cordeiro, for his helpful suggestions and creativity in the development of scientific instruments used in the experiments.

Last but not least, I express my deepest gratitude to my parents, Ghulam Mujtaba and Nargis Mujtaba for their love, prayers, unconditional support and sacrifice, without them I could never achieve my dreams. I am also grateful to my wife, Usra. Without her understanding, patience and support, I would have never finished my PhD.

Financial and institutional support

The author is grateful to the MARE - Marine and Environmental Sciences Centre, as a host institution. The research presented in this thesis was supported by the following projects:

- Project HIRT - Modelling surface hydrologic processes based on infrared thermography at local and field scales (PTDC/ECM-HID/4259/2014 – POCI-01-0145-FEDER-016668), funded by FCT, Portugal, and FEDER,
- Project ASHMOB - Wildfire ASH MOBilization by wind and water erosion (02/SAICT/2017), within the PT2020 Partnership Agreement and Compete 2020 co-funded by FEDER,
- Erasmus+ mobility programme,
- COST Action CA16219, HARMONIOUS - Harmonization of UAS techniques for agricultural and natural ecosystems monitoring”, financed by the European Cooperation in Science and Technology (COST), through the EU Framework Programme Horizon 2020.

The author also acknowledges the Institute of Hydrology, Slovak Academy of Sciences, Bratislava, Slovak republic, for the field data used in the study, presented in Chapter 4.

Abstract

Rainfall-induced surface runoff combined with soil erosion is one of the most important surface hydrological processes and its harmful impact on the environment and communities has been studied for decades. Understanding and modelling surface hydrological processes is vital for engineers, scientists, and policymakers to be able to develop water management and soil conservation strategies. Therefore, mathematical models that can predict the impact of surface hydrological processes on the environment require good quality measured hydrological data. Cost-effective innovative techniques are needed to obtain the good quality hydrological data from field and laboratory experiments. Furthermore, the presence of rock fragments in soils is a major soil property. Identifying the relationship between the rock fragments and surface-subsurface hydrological processes is a major challenge but one that is essential for the development of soil water conservation measures for the rock-fragment abundant soils.

The present thesis focuses on two main objectives. The first is to improve understanding of the impact rock fragments have on surface-subsurface hydrological processes at plot and hillslope catchment scale. The second is concerned with the development of innovative measuring techniques and mathematical models related to surface hydrological processes.

The research for the first objective started by comparing the influence of soil surface geometry and different distributions of surface rock fragment cover on runoff and soil loss under controlled laboratory conditions. Three different patterns of a constant surface rock fragment cover were tested for a single rainfall intensity event on converging and diverging plane soil surfaces at constant hillslope gradient. The study suggested that the understudied soil surface geometries had more influence on soil erosion than different distribution patterns of a specific percentage of rock fragment surface cover. The next study compared the simulated soil water response of stony soils with measured catchment runoff at hillslope scale. Rainfall-induced soil water response was simulated at three mountain catchment sites using the Hydrus-2D single porosity model. The soils at these sites had 10-65% stoniness. Soil hydraulic parameters employed in the numerical simulations, i.e. the saturated hydraulic conductivity and parameters of the soil water retention curves, were obtained by the Representative Elementary Volume approach (REVa) and by the inverse modelling with Hydrus-1D model (IMa). Shapes of the simulated soil water outflow hydrographs were similar to the measured catchment runoff ones for about a half of rainfall events. Furthermore, soil hydraulic parameters derived by REVa produced more realistic shapes of soil water hydrographs than the IMa ones.

The research for the second objective started by testing the capability of a new thermal tracer (cold oil droplets) to measure the velocities of shallow overland flows (<2 mm depth) using the infrared-based particle tracking velocimetry (PTV) technique under controlled laboratory conditions without rainfall. This new approach was compared with dye tracing and the conventional PTV technique (polystyrene beads as tracer and optical video camera) in a quasi-laminar flow regime. The results showed that the infrared-based and conventional PTV techniques estimated velocities were closer to mean velocities measured through volumetric discharge method than were those given by the dye tracing method. This research stressed the potential of the infrared-based PTV technique to estimate the velocities of shallow water bodies due to its tracer's prominent visibility and independence from lighting conditions. Lastly, a 1D physically-based overland flow model that uses cascade plane theory for the estimation of rainfall-induced surface runoff, infiltration and soil erosion on converging and diverging plane surfaces was developed. The model’s simulations were evaluated by the measured data collected under controlled laboratory conditions. Satisfactory results indicated that the model could help to improve the modelling techniques for overland flow and soil erosion on convergent and divergent plane surfaces.

Keywords: Soil rock fragments, Laboratory experiments, Soil erosion, Subsurface flow, Soil water flow modelling, Infrared thermography, Particle tracking velocimetry, Soil erosion modelling.

Resumo

O escoamento superficial e o transporte sólido, induzidos pela precipitação, são importantes processos hidrológicos estudados há décadas, sendo o seu impacto muitas vezes prejudicial no meio ambiente e nos aglomerados populacionais. Compreender e modelar os processos hidrológicos de superfície é vital para que engenheiros, cientistas e decisores políticos possam desenvolver estratégias de gestão de água e conservação do solo. É por isso que os modelos matemáticos que podem prever o impacto dos processos hidrológicos de superfície no meio ambiente requerem dados hidrológicos de qualidade. São necessárias técnicas inovadoras e económicas para obter dados hidrológicos de boa qualidade em experiências de campo e de laboratório. A presença de pedras é uma propriedade importante do solo. Identificar a relação entre as pedras e fragmentos de rocha e os processos hidrológicos subsuperficiais é um grande desafio, mas é essencial para o desenvolvimento de medidas de conservação da água do solo para esses solos pedregosos.

A presente tese concentra-se em dois objetivos principais. O primeiro é melhorar a compreensão do impacto que as pedras têm nos processos hidrológicos de superfície e subsuperficiais à escala de parcela e da bacia de drenagem. O segundo está relacionado ao desenvolvimento de técnicas inovadoras de medição e ao desenvolvimento de modelos matemáticos relacionados aos processos hidrológicos de superfície.

A pesquisa relativamente ao primeiro objetivo começou por comparar a influência da geometria da superfície do solo e diferentes distribuições da cobertura de fragmentos de rocha no escoamento superficial e perda de solo, em condições controladas de laboratório. Três padrões diferentes de cobertura de pedras em superfícies planas, convergentes e divergentes, foram testados para uma chuvada tipo. Esse estudo concluiu que a geometria da superfície do solo tinha mais influência que os padrões de distribuição das pedras na severidade do processo de erosão. O estudo seguinte comparou a resposta da água no solo de solos pedregosos com o escoamento medido de bacia de drenagem, à escala da encosta. A resposta da água no solo induzida pela chuva foi simulada em três locais da bacia hidrográfica usando o modelo Hydrus-2D. Os solos nesses locais tinham pedregosidade entre 10-65%. Os parâmetros hidráulicos do solo usados nas simulações numéricas, ou seja, a condutividade hidráulica saturada e os parâmetros das curvas de retenção de água no solo, foram obtidos pela abordagem do Volume

Elementar Representativo (REVa) e pela Modelagem Inversa com o modelo Hydrus-1D (IMa). As formas dos hidrogramas de água do solo simulados foram semelhantes às medidas formas dos hidrogramas de escoamento superficial das bacias para cerca de metade dos eventos de chuva. Além disso, os parâmetros hidráulicos do solo derivados do REVa produziram formas mais realistas de hidrogramas da água do solo do que os do IMa.

A pesquisa para o segundo objetivo começou por testar a capacidade de um novo traçador térmico (gotas de óleo arrefecidas) para estimar as velocidades de escoamentos superficiais pouco profundos (<2 mm de profundidade) usando a técnica de velocimetria de rastreamento de partículas (PTV), baseada em infravermelho, sob condições controladas de laboratório. Esta nova abordagem foi comparada com o método do traçado colorido e a técnica PTV convencional (usando grânulos de poliestireno como traçador e uma câmara de vídeo) num regime de escoamento quase laminar.

Os resultados mostraram que as velocidades estimadas das técnicas PTV convencionais e as baseadas no infravermelho estavam mais próximas das velocidades médias obtidas pelo método de volumétrico do que as velocidades do método de traçado colorido. Esta pesquisa enfatizou o potencial da técnica PTV baseada no infravermelho para estimativa das velocidades de escoamentos pouco profundos devido à alta visibilidade do traçador e independência das condições de iluminação. Por último, foi desenvolvido um modelo de escoamento superficial 1D, fisicamente baseado, que usa a teoria da cascata de planos para a estimativa do escoamento superficial, infiltração e erosão hídrica do solo em superfícies convergentes e divergentes. As simulações do modelo foram avaliadas comparando os resultados numéricos com dados medidos em laboratório. Os resultados indicaram que o modelo podia ajudar a aprimorar a modelação do escoamento superficial pouco profundo e a erosão do solo em superfícies planas convergentes e divergentes.

Palavras-chave: Fragmentos de rocha do solo, Experiências de laboratório, Erosão do solo, Escoamento hipodérmico, Modelação do escoamento de água no solo, Termografia por infravermelhos, Velocimetria de rastreamento de partículas, Modelação da erosão hídrica do solo.

Table of Contents

List of Figures

List of Tables

1. Introduction

1.1. Motivation and framework

Rainfall induced surface runoff and the associated soil erosion is a natural occurring phenomenon which can contribute to the destruction of aquatic ecosystem by transporting chemical pollutants into freshwater (e.g. Kronvang et al., 2007; Owens et al., 2008; Scherer et al., 2012), to degradation of agricultural lands by removing the fertile nutrient rich top surface of soil bed (Creamer and Baldwin, 2000), to flooding by decreasing the hydraulic capacity of man-made hydraulic structures and natural streams through sediment deposition and to rainfall induced landslides by excessive pore water pressure and soil water content. Therefore, understanding and modelling of surface runoff and soil erosion is vital for engineers, scientists, and policy makers for the development of water management and soil conservation strategies.

Mathematical models are a cost effective and flexible tool to predict beforehand the environmental impact of different surface hydrological processes under various climate change and land use scenarios. Laboratory and field experiments are required for the validation of a numerical model. The robustness of any model predictions depends on the quality of measured data and the complexity of surface hydrological parameters involved. Measurement techniques for these parameters faces many obstacles such as high costs, portability constrains, calibration problems in certain conditions and low resolution. Therefore, scientists and engineers are always pursuing innovative techniques to obtain good hydrological data with fewer hurdles.

Soils containing considerable amount of rock fragments (soil particles larger than 2 mm in diameter), commonly known as stony soils are found in mountainous and forested areas of the world. According to Poesen and Lavee (1994), there are about 30% of such soils in Western Europe; in the Mediterranean region stony soils cover around 60% of the territory. Rock fragments resting on soil surface have an ambivalent effect on surface hydrological processes. On the one hand, some studies showed that surface rock fragments decrease surface runoff volume, reduce soil erosion and enhance water infiltration (e.g. de Figueiredo and Poesen, 1998; Mandal et al., 2005; Mayor et al., 2009) while, the other studies (e.g. Iverson, 1980; Wilcox et al., 1988; Jordán et al., 2010) found a positive relation of surface rock fragment with runoff and soil erosion. A quantitatively accurate description of the relationship between surface rock fragments and surface hydrological processes is difficult to define due to the influence of several interacting factors such as soil physical–chemical properties, soil structure, initial soil water content, rainfall characteristics, land and vegetation cover, hillslope gradient, soil surface geometry and spatial scale. Moreover, lateral subsurface flow plays an important role in runoff formation at mountainous hillslopes (Bachmair and Weiler, 2011). Presence of rock fragment content has a great impact on soil structure and soil water characteristics; thus, making soil water flow processes to understand in stony soils more difficult than in non-stony soils (e.g. Hlaváčiková et al., 2014, 2016, 2018). Hillslope lateral subsurface flow is dependent on soil properties such as infiltration capacity, heterogeneity of hydraulic conductivity, soil water retention, thickness of unsaturated zone and preferential pathways. Increase in soil stoniness decreases the hydraulic conductivity of soil by reducing the effective cross-sectional area of soil profile through which water flow, making the water flow path more elongated. But, soil stoniness increase can also produce temporal preferential pathways along the rock-soil interface due to shrinking and swelling phenomenon, resulting in higher saturated conductivity. Preferential pathways can produce rapid formation of the subsurface flow that eventually contributes to catchment stormflow (Beven and Germann, 1982). Therefore, the need to study the role of rock fragments on runoff generation and soil erosion is vital to understand the water cycle of hillslopes.

The present thesis is focussed on two main goals. First objective is to create further understanding of rock fragments impact on surface-subsurface hydrological processes at plot and hillslope catchment scale. Second one deals with the development of innovative measuring techniques and mathematical models related to surface hydrological processes. More specifically, the objectives of thesis are:

- to evaluate the influence of different distribution patterns of rock fragment surface cover and soil surface geometry on runoff and soil loss through laboratory experiments;
- to study the role of stony soils in runoff response of a small mountain catchment through numerical simulations;
- To test the capabilities of a new thermal tracer for velocity estimation of shallow overland flows;
- To develop a one-dimensional rainfall induced soil erosion numerical model based on cascade plane theory.

The presented doctoral study, from 2015 to 2021, was done at the Universidade de Coimbra. For first three years, the author of thesis did the experimental work in Laboratory of Hydraulics, Water resources and Environment, Universidade de Coimbra, using different instruments such as, soil flume, rainfall simulator, infrared thermographic cameras, optical cameras and soil moisture sensors. The author also spent two months, under Erasmus mobility program, in Institute of Hydrology of the Slovak Academy of Sciences, Bratislava, to conduct part of thesis research work related to subsurface flow modelling in stony soils and measured hydrological data of small mountainous hillslope. In last three years, author finished thesis writing and published most of the doctoral research work in international journals.

1.2. Thesis structure

The thesis is structured in eight chapters. Their content is briefly summarized in the following paragraphs.

- **Chapter 1. Introduction.** This chapter gives the motivation of this research study, defines the objectives, describes the structure of this documents and presents the research publications involved in the achievement of the present thesis.
- **Chapter 2. Literature review.** This chapter presents the overview of the contribution of lateral subsurface flow in the overland runoff generation on hillslopes. It briefly describes the soil erosion processes and modelling, and the rock fragments role on surface-subsurface hydrological processes. Finally, it illustrates some techniques regarding rainfall, soil characteristics and flow velocity measurements used in surface hydrology.
- **Chapter 3. Importance of the hydraulics of converging and diverging flows on soil erosion override effects of rock fragment cover patterns: Experimental assessment.** This chapter compares the influence of soil surface geometry and different distribution of surface rock fragment cover on runoff and soil loss in controlled laboratory conditions. Three different patterns of constant surface rock fragment cover were tested for single rainfall intensity event on converging and diverging plane soil surfaces at constant hillslope gradient. Application of organic mulch on these soil surface geometries was also tested for soil and water conservation.
- **Chapter 4. The role of stony soils in hillslope and catchment runoff formation.** This chapter presents the comparison of the subsurface runoff response from stony

soils with observed surface runoff response at mountainous catchment's outlet. Soil hydraulic parameters applied in Hydrus-2D single porosity model for soil water response simulations were obtained by the Representative Elementary Volume approach and by the inverse modelling with Hydrus-1D model. Suitability of these approaches for soil hydraulic parameters determination for stony soils was also analysed. Field measurements that were used for this study are shown in Fig. 1.1.

Fig. 1.1. Field measurements done for stony soil characteristics of the studied mountainous catchment.

- **Chapter 5. Laboratory testing of a new thermal tracer for infrared-based PTV technique for shallow overland flows**. This chapter presents the testing of a new thermal particle tracer (cold oil droplets) capabilities to measure the velocity of shallow overland flows (<2 mm depth) using the infrared-based particle tracking velocimetry (PTV) technique. Velocity measurements were taken under controlled laboratory conditions by infrared-based based PTV, conventional PTV (polystyrene beads as tracer and optical video camera), dye tracing optical video camera and volumetric discharge techniques. Comparison of these techniques' results evaluated the performance of the new thermal particle tracer. Movement of oil droplets over a shallow overland flow in the presence of hurdles captured by the infrared-based PTV technique is shown in Fig. 1.2.

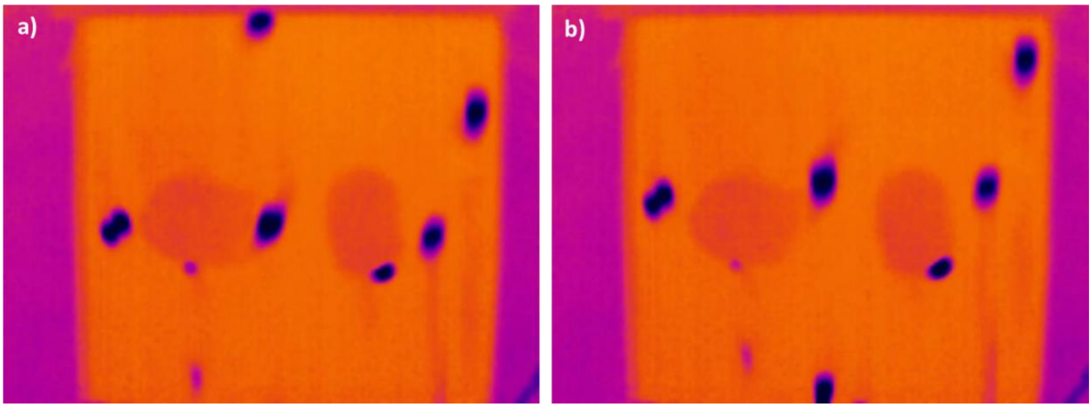

Fig. 1.2. Movement of oil droplets in two consecutive thermographic images (a) and (b) in the presence of rock fragments resting on soil crust surface.

- **Chapter 6. Laboratory testing of a one-dimensional cascade model for runoff and soil erosion on converging and diverging plane surfaces.** This chapter describes the conceptualization and validation of a one-dimensional numerical overland flow model that uses the cascade plane theory for the estimation of rainfall induced runoff and soil erosion. The model has three components i.e. 1) soil infiltration component solves Horton's equation, 2) kinematic overland flow component for a cascade of planes and 3) soil erosion component solves the sediment transport continuity equation. Numerical simulations were evaluated with the data from laboratory rainfall simulation experiments on a soil flume.
- **Chapter 7. Conclusions and Final remarks.** This chapter summarizes the overall conclusions and gives suggestions for future research investigations.
- **Chapter 8. References.** This chapter lists the publications consulted during this doctoral study, which are referenced in the previous chapters.

1.3. Publications

Chapters 3 to 5 of this thesis were published in international journals and are presented here as published by the journals, except for some layout changes, such as size, position and numbering of figures and tables. Chapter 6 was submitted to an international journal. References of the articles are presented next:

- **Chapter 3. Mujtaba, B.**, de Lima, J.L.M.P., de Lima, M.I.P., Vargas, M.M., 2019. Importance of the hydraulics of converging and diverging flows on soil erosion override effects of rock fragment cover patterns: experimental assessment. Zeitschrift für Geomorphol.

62 (3), 183–197. https://doi.org/10.1127/zfg/2019/0578

- **Chapter 4.** **Mujtaba, B.**, Hlaváčiková, H., Danko, M., de Lima, J.L.M.P., Holko, L., 2020. The role of stony soils in hillslope and catchment runoff formation. J. Hydrol. Hydromechanics 68 (2), 144–154. https://doi.org/10.2478/johh-2020-0012
- **Chapter 5.** **Mujtaba, B.**, de Lima, J.L.M.P., 2018. Laboratory testing of a new thermal tracer for infrared-based PTV technique for shallow overland flows. Catena 169, 69-79. https://doi.org/ 10.1016/j.catena.2018.05.030
- **Chapter 6.** **Mujtaba, B.**, de Lima, J.L.M.P., de Lima, M.I.P.. Laboratory testing of a one-dimensional cascade model for runoff and soil erosion on converging and diverging plane surfaces. (submitted in 2021 to an international Journal with Impact Factor).

The research conducted in this thesis also contributed to presentations (oral and poster) in several national and international scientific meetings, which are listed in the author's curriculum vitae. The author of this thesis was also involved in several other studies in the field of Hydraulics, Water Resources and Environment, during his doctoral studies, that resulted in publications but were not included in this thesis. One way or another, these studies also contributed to the knowledge that was needed for the success in completing the thesis. These publications are:

- de Lima, J.L.M.P., Santos, L., **Mujtaba, B.**, de Lima, M.I.P., 2019. Laboratory assessment of the influence of rice straw mulch size on soil loss. Adv. Geosci. 48, 11-18. https://doi.org/10.5194/adgeo-48-11-2019

- Lopes de Almeida, J.P.P.G., **Mujtaba, B.**, Oliveira Fernandes, A.M., 2018. Preliminary laboratorial determination of the REEFS novel wave energy converter power matrix. Renew. Energy 122, 654-664. https://doi.org/10.1016/j.renene.2018.01.030

- de Lima, C.A., de Lima, J.L.M.P., Montenegro, A.A.A., **Mujtaba, B.**, Abrantes, J.R.C.B., 2018. Comparative evaluation of factors influencing seed displacement over the soil of nonconventional perennial crops: Moringa (*Moringa oleifera* Lam.) and Neem (*Azadirachta indica* A. Juss.). Soil Sci. 182 (8), 267-277. https://doi.org/10.1097/ss.0000000000000219

- Silveira, A., de Lima, J.L.M.P., Abrantes, J.R.C.B., **Mujtaba, B.**, 2017. Washout of fine sand particles from a ceramic tile roof: laboratory experiments under simulated rainfall. Water Air Soil Pollut., 228-352. https://doi.org/10.1007/s11270-017-3529-8

2. Literature review

This chapters briefly reviews some research studies on surface-subsurface hydrological processes that are relevant to later chapters. The first part of this chapter gives a short overview of the lateral subsurface runoff role in surface runoff generation at hillslopes. The second part describes the rainfall induced soil erosion processes and their controlling factors. The third part summarizes soil erosion modelling. The fourth part details the impact of rock fragments on surface-subsurface hydrological processes. The fifth part gives a state of the art about some measurement techniques used in surface hydrology to assess the characteristics of rainfall, soil morphology, soil sampling of stony soils, soil moisture and shallow flow hydraulics.

2.1. Lateral subsurface flow contribution in surface runoff generation at hillslopes

Lateral subsurface flow (Fig. 2.1), also known as interflow, soil water flow, subsurface runoff or subsurface storm flow, represents water movement laterally down a hillslope through the unsaturated soil zone until it reaches the stream channel (e.g. Sabzevari and Noroozpour, 2014; Hu and Li, 2019). This happens due to the entrapment of a portion of infiltrated water at the top soil layer, as a result of permeability contrast with a lower soil layer, or at soil-bedrock interaction, which in turn creates transient subsurface saturation, resulting in downslope water movement. In many upland environments, lateral subsurface flow is the dominant runoff producing mechanism that determines the hydrological response of catchments to rainstorm events. Lateral subsurface flow mainly occurs in humid catchments, where terrain slope is steep, surface soil has high porosity and soil-bedrock interface is near the surface (e.g. Turton et al., 1992; Holko et al., 2011; Jung et al., 2020). In arid regions and lowland areas where slope is gentle, subsurface flow generation is rare and can only be activated under high rainfall intensity and high antecedent soil moisture condition (Wilcox et al., 1997).

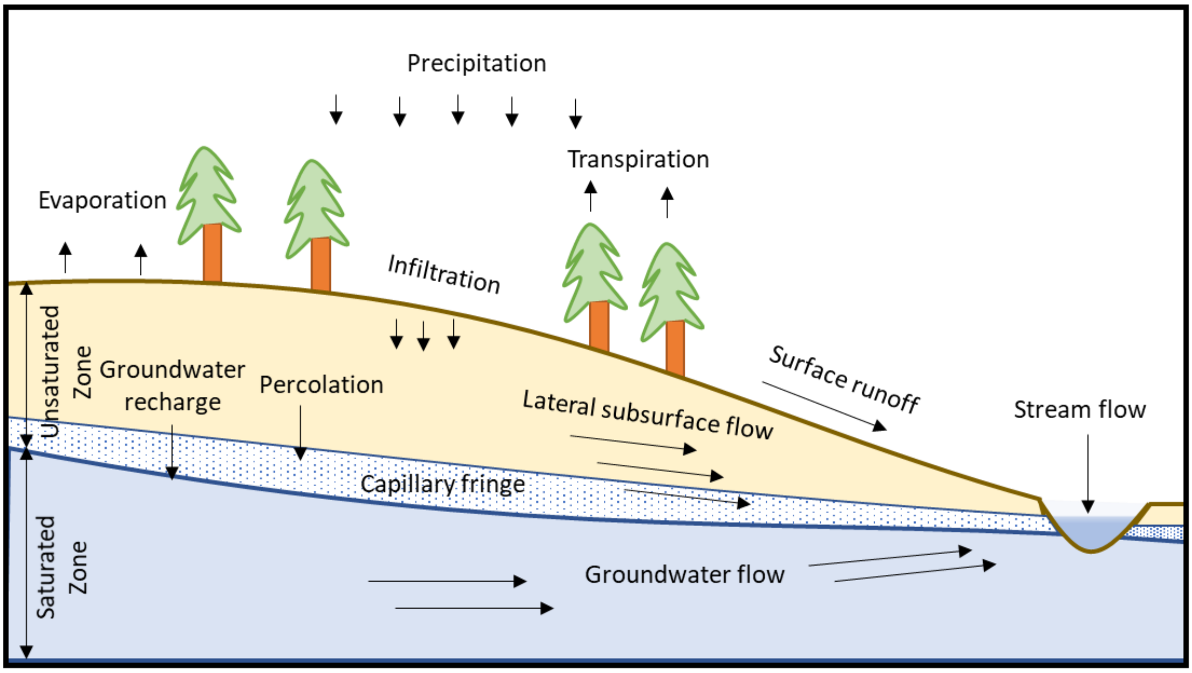

Fig. 2.1. Schematic representation of lateral subsurface flow at hillslope.

The lateral subsurface flow drains slower than surface runoff but faster than groundwater flow. The main responsibility of lateral subsurface flow is quick response to storm flow during rainstorm event. It can drain water from the soil unexpectedly fast, which contributes to storm flow. This quick soil drainage delays or prevent saturation overland flow to occur (e.g. Weiler et al., 2006; Tromp-Van Meerveld and McDonnell, 2006a). Rapid formation of lateral subsurface flow at hillslope that contribute to stream flow can be explained by preferential flow in the soil (Beven and Germann, 1982), instability-driven flow (Tesař et al., 2001) or fill and spill mechanism (Tromp-Van Meerveld and McDonnell, 2006b). Mujtaba et al. (2020, Chapter 4 of this Thesis) explored the idea that rapid subsurface runoff response can occur in stony soils due to the soil water retention capacity reduction by soil stoniness, rather than the more often invoked preferential flow explanation. This study stresses the need for more reliable field and laboratory data to characterize soil stoniness and its variability in order to further investigate this central idea.

2.2. Rainfall-induced soil erosion

Rainfall-induced soil erosion is natural occurring phenomena in the world. According to Foster et al. (1982), soil erosion is the process of detachment, transportation and deposition of soil particles by rainfall and surface runoff. Soil erosion is responsible for degradation of agricultural land by removing the fertile nutrient rich top surface of soil bed (Martínez-Mena et al., 2020). Soil erosion threatens the ecosystem by damaging the water quality as it transports eroded soil, nutrients and chemical pollutants into freshwater (e.g. Scherer et al., 2012; Issaka and Ashraf, 2017). Splash, sheet, rill and gully are the types of soil erosion that occur in different stages of the erosion process depending mainly on surface characteristics, rainfall intensity and slope (Fig. 2.2).

Generally, splash erosion is the first process of rainfall-induced soil erosion. Splash erosion is the detachment of soil particle by raindrop splash. Detachment of soil particles occur when impact forces of raindrops destroy the interlocking matrix of soil surface which are later transported by overland flow (e.g. Jomaa et al., 2012a; Beguería et al., 2015). Rainfall intensity, kinetic energy of raindrop, angle of raindrop impact and soil characteristics are the factors that influence splash erosion (e.g. Angulo-Martínez et al., 2012; Ma et al., 2014; Xiao et al., 2017). Due to the continuing pounding of raindrops, the soil aggregates are broken down in smaller particles which in turn get deposited into soil pores creating a thin impermeable layer, called soil surface sealing or crust (e.g. Lu et al., 2017; Ran et al., 2018). The surface sealing helps to decrease detachability of soil particles by increasing cohesion of soil particles and reduce infiltration (e.g. Sela et al., 2012; Han et al., 2016).

After detaching by the raindrop splash, soil particles are transported by rainfall generated overland shallow flow. With increase in flow depth, splash erosion rates decrease. Erosive forces of shallow flow also start to detach soil particles from the soil surface causing sheet erosion. The combination of splash and sheet erosion is known as interrill erosion, which is a dominant erosion process on the soil surface of the hillslope in terms of surface area but contributes a small portion in total sediments mobilized (e.g. Wu et al., 2018; Wang et al., 2020; Zhang et al., 2020). When rainfall generated overland flow concentrates due to topographic landforms, few tens of millimetres wide rills are formed. Erosion in these macrochannels, termed as rill erosion, is responsible for majority of sediments removal from the hillslope due to strong erosive forces associated with concentrated surface runoff (e.g. Zhang et al., 2008; Kenny et al., 2018). Rill erosion plays a dominant role in interrill-rill erosion process when the annual soil loss rate exceeds 15 t ha^{-1} yr^{-1}, which is a general guideline (Foster, 2004). If erosive forces increase more, small rills may converge into each other to form a large channel called gully (Poesen et al., 1990), starting the gully erosion.

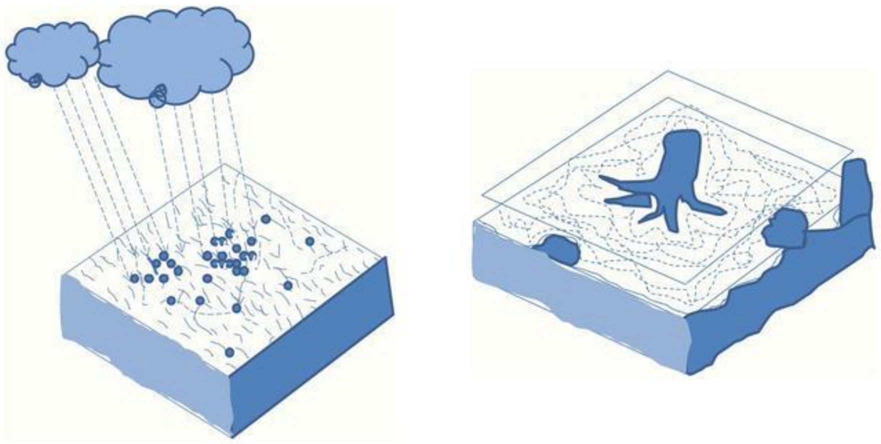

1. Splash Erosion

2. Sheet Erosion

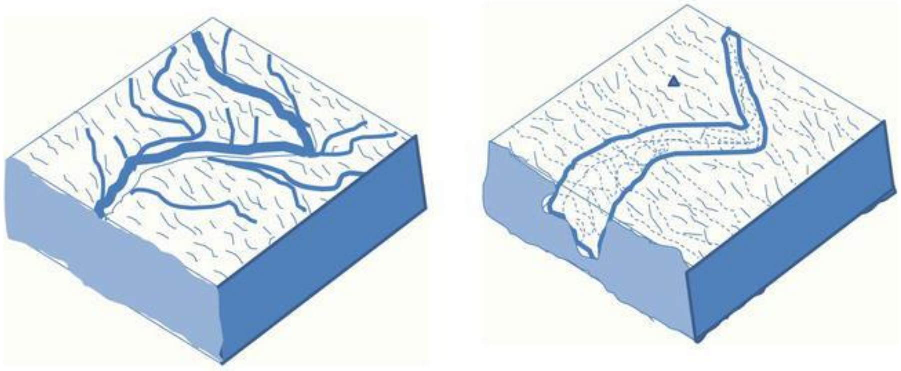

3. Rill Erosion

4. Gully Erosion

Fig. 2.2. Basic types of rainfall-induced soil erosion (Kumawat et al., 2020).

Rainfall, soil characteristics, hillslope topography and organic mulches are some of the factors affecting the soil erosion process. Details of these factors are given below.

2.2.1. Rainfall characteristics

The rainfall intensity and duration are the most important rainfall characteristics that affect soil erosion processes. Increase in rainfall intensity for a given duration increases the soil erosion(e.g. Salem and Meselhy, 2021; Zhang et al., 2020). Moreover, extreme rainfall events of shorter duration can generate higher soil loss than lower intensity events of longer duration (Ran et al., 2012). Furthermore, raindrops kinetic energy is an important controlling factor in splash erosion. Kinetic energy of rainfall, depending on size, amount and velocity of rain drops, has to exceed a threshold value to detach soil particles (Kinnell, 2005). Determination of rainfall kinetic energy and intensity relationship is vital to estimate rainfall erosivity i.e. capability of rainfall to induce soil erosion (Nearing et al., 2017).

Different rainfall spatial and temporal patterns have different impact on soil erosion processes. For example, Römkens et al. (2002) using a laboratory setup showed that eroded soil mass is higher when the sequence of rainstorms of decreasing intensity were applied on air-dried soil surface compared to the similar rainstorms sequence of increasing intensity. de Lima et al. (2003) observed that downstream moving storms produced higher soil loss than upstream moving storms. de Lima et al. (2012)`conducted soil experiments in laboratory conditions applying rainfall temporal patterns consisting of short duration heavy burst occurring at different times of constant base rainfall event; this study concluded that rainfall events in which burst came in later stage (delayed pattern) accumulated the highest soil loss compared to advanced and centred rainfall patterns.

2.2.2. Soil surface morphology

Soil surface morphology, commonly known as microrelief, is elevation variation of soil surface amounting no more than few centimetres, quantitatively described by soil roughness ratio (e.g. Bauer et al., 2015; Bullard et al., 2018). Rainfall induced erosion and deposition processes are deriving controlling factors of the soil roughness. Bullard et al. (2018) using laboratory setup observed that soil surface roughness increased for lower rainfall amount (2 mm) and decreased for higher rainfall amount (5mm) due to ponding occurrence. They also found that changes (increase/decrease) in surface roughness were caused by direct raindrop impact, courtesy of low rainfall amount and fine soil composition. On stony soil plots, Li et al. (2020) found soil roughness increased on steeper slopes and was also affected by the rainfall induced erosional features and increase in surficial exposed rock fragments.

Soil roughness, to some extent, affect soil erosion by influencing the infiltration, overland flow, evaporation and surface storage capacity of both water and eroded mass. Gómez and Nearing (2005) using laboratory setup found that rainfall induced soil erosion was higher on rough surface than smooth one at mild slope (5%) due to flow concentration around rougher topographic elements. At steep slope (20%), noteworthy runoff and soil loss differences between rough and smooth surfaces were not found. Vermang et al. (2015) observed on mild slope (5%) that soil surface roughness is important for rainfall induced runoff generation but not for sediment loss. Zhao et al. (2016) observed that soil surface with mounds increased soil loss compared to smooth surface. However, the surface with depressions decreased erosion rates at hillslope scale due to higher surface storage capacity. Increase in rainfall intensity and duration caused the depression effect to minimize, resulting in higher soil loss than smooth surface.

2.2.3. Soil water repellency and crusting

Water repellency is the soil property that restricts water infiltration by coating the dry soil particles with hydrophobic compounds. Organic hydrophobic matter in soils are supplied from wide range of vegetation such as mosses, grasses, shrubs and trees (e.g. Mao et al., 2016; Barthlott et al., 2017; Jia et al., 2020; Papierowska et al., 2020). Presence of factors such asfires, soil temperature, soil water content, soil structure and chemicals, can also make soil water repellent (e.g. Woche et al., 2005; Leelamanie and Nishiwaki, 2019; Weninger et al., 2019; Głąb et al., 2020). Water repellency enhance surface runoff by reducing soil wettability and making soil susceptible to rainfall induced erosion, reported by various laboratory and field studies (e.g. Cawson et al., 2016; Robichaud et al., 2016; Lowe et al., 2021). Overland flow generation and sediment transport mechanisms on hydrophobic soils are different than on wettable soils. Splash erosion on hydrophobic soils is higher than on wettable soils (Ahn et al., 2013). Small water pathways known as rivulets are formed on the surface of hydrophobic soils that areresponsible for runoff and eroded sediments transportation. Dry soil left around these stable narrow water pathways continuously supply soil particles dispersed by rain drop impact. Whereas, on wettable soils, surface is somehow protected from splash erosion by the rainfall induced overland flow sheet.

Soil crust or seal is the surface layer that has higher shear strength, greater bulk density, finer pores and lower hydraulic conductivity than underlying soil. The soil sealing reduce water infiltration, increase surface runoff and protect the surface from splash erosion (e.g. Sela et al., 2012; Zhou et al., 2013; Ran et al., 2018). Seal formation on wet soils is quicker, resulting in lower sediment yield than on dry soils (e.g. Han et al., 2016; Zambon et al., 2021). Two types of rainfall induced seals are formed on soil surface: 1) structural seal form as a result of the compaction done by the raindrops' impact, and 2) depositional seal is formed by the deposition of translocated eroded fine particles into the surface soil pores spaces (Lu et al., 2017). Wu et al. (2016) observed through artificial rainfall simulation on three distinct soil tillage surfaces that structural sealed surfaces yielded lower runoff and sediments loss than depositional sealed surfaces. However, both sealed surfaces had higher runoff volume and lower soil loss than the unsealed surfaces on every tillage treatment.

2.2.4. Hillslope topography

Hillslope surface geometry is complex. Researchers (e.g. Talebi et al., 2008; Sabzevari et al., 2013; Sabzevari and Talebi, 2019) have categorized hillslope geometry in nine shapes depending on soil surface profile curvature (convex, plane, concave) and slope shape (converging, linear, diverging). These shapes are linear plane, converging plane, diverging plane, converging convex, diverging convex, linear convex, converging concave, diverging concave and linear concave surfaces. Some researchers have studied the soil erosion response on different soil surface geometries. Young and Mutchler (1969) conducted simulated rainfall experiments on 12 field plots to investigate soil loss and runoff response on three different surface curvatures of linear shaped soil slope. They found that linear concave soil slope had accumulated less soil loss compared to linear plane and linear convex slopes. In laboratory conditions, D'Souza and Morgan (1976) measured soil loss from linear plane, linear convex and linear concave soil slopes at 3.5, 7, 10.5, 14 and 18% slopes under simulated rainfall. They found that linear concave slope yielded less soil loss than the other two soil surface geometries. Rieke-Zapp and Nearing (2005) evaluated the soil erosion response by simulated rainfall in controlled laboratory experiments on five curvatures of linear shaped soil slope i.e. linear plane, linear concave, linear convex, nose slope and head slope. Their results indicated that soil loss on head and linear concave slopes was lower than on linear plane, linear convex and nose slopes. de Lima et al. (2018) concluded that convex curvatures of linear shaped soil slopes were the most hazardous in terms of the generation of runoff and sediments, when compared with concave, convex-concave, and concave-convex curvatures of linear shaped soil slopes. Also, Sabzevari and Talebi (2019) observed through laboratory experiments and modelling that slope shapes (linear, converging and diverging) of convex curvature hillslopes were more susceptible to soil erosion than the plane and concave hillslopes. They also found that for a given hillslope curvature, converging soil surface produced higher erosion rates than diverging and linear ones.

2.2.5. Organic mulches

Usage of organic mulches as a soil and water conservation method has been adopted for decades on agricultural lands on hillslopes. In general, organic residues (e.g. mulch) increases infiltration and decreases soil erosion and runoff volume. Zonta et al. (2012) experimentally demonstrated that infiltration rate is lower for soil without crop residue cover as compared to soil with crop residue. Jordán et al. (2010) noted that delay in runoff generation along with soil loss and runoff was decreased by mulching in semiarid region of Spain. Several studies (e.g.

Montenegro et al., 2013; Prats et al., 2017; Abrantes et al., 2018b) have argued that organic mulch protects the soil surface from splash erosion by intercepting the rain drop impact on soil surface; thus, reducing the soil surface crusting and sealing. Moreover, mulch decreases runoff by absorbing the water itself, decreasing runoff velocity and increasing runoff ponding time, which increases infiltration. Due to the soil protection from raindrop impact and flow retardation promoted by mulch cover, soil loss is lower than for bare soil conditions.

Existing studies (e.g. Cerdà, 2001; Pannkuk and Robichaud, 2003; Cook et al., 2006; Adekalu et al., 2007; Mupangwa et al., 2007; Foltz and Wagenbrenner, 2010; Jordán et al., 2010; Gholami et al., 2013; Montenegro et al., 2013; Prats et al., 2015; Hosseini et al., 2017; Abrantes et al., 2018b) in laboratory and field conditions have used different types of organic mulch such as leaf litter, woodchips, bark chips, rice straw, elephant grass, wheat, soybean, maize, barley, eucalypt chopped bark, wood strands and pine needles. Testing of rice straw mulch for soil and water conservation is shown in Fig. 2.3, as an example.

Fig. 2.3. Application of rice straw (organic mulch type) on a converging plane soil surface in controlled laboratory conditions (Photograph taken by the author of this thesis on the 15th June, 2017).

Application rate, cover percentage and spatial distribution of mulch have impact on runoff and soil loss. Laboratory experiments were conducted by Montenegro et al. (2013) to study the effect of two different mulch densities (2 t/ha and 4 t/ha) on soil erosion process under intermittent rainstorms. The study concluded that increase in mulch application rate have increased infiltration, decreased runoff (especially the peak discharge), decreased soil loss and delayed runoff generation. Pan and Shangguan (2006) conducted laboratory experiments with different cover percentages (0%, 35%, 45%, 65% and 90%) of grass at 15^o slope angle under simulated rainfall conditions. They concluded that increase in cover percentage of grass significantly decreased the runoff volume and soil loss. Jin et al. (2009) applied three uniform rainstorms (65, 85 and 105 mm h^{-1}) separately on four different cover percentages (0%, 25%, 50% and 75%) of mulch to examine the effect on runoff and sediment yield. It was seen that lower rainfall intensity (65 mm h^{-1}) and percentage of mulch cover percentage (25%) produced the highest runoff and soil loss.

Furthermore, application of mulch in specific regions of plot in form of strips rather than the whole area has been proven a cost-effective method to counter the soil erosion problem. In field conditions, Bhatt and Khera (2006) studied the runoff and soil loss response in the presence of four different modes of mulch application i.e. mulch over a whole plot, mulch over one third of plot, horizontal mulch strips and vertical mulch strips. In controlled laboratory conditions, Prats et al. (2015) compared different mulch strip schemes effectiveness to reduce runoff and soil loss under simulated rainfall and concentrated flow. Abrantes et al. (2018b) in laboratory conditions used three mulching strip schemes i.e. over whole plot area. 1/3 of plot and 2/3 of plot, for two different mulch cover percentages (50% and 70%). All these above-mentioned studies found that mulch over the whole plot area reduces the highest runoff and soil loss compared to strips application; however, runoff and soil loss rates of strips application are not significantly different from the ones of whole plot mulching.

Apart from soil erosion processes, organic mulch also affects the soil moisture and topsoil temperature. In laboratory conditions under simulated rainfall, Montenegro et al. (2013) found that higher mulch rate (4 t/ha of rice straw) led to higher soil moisture than the lower mulch rate (2 t/ha) and bare soil condition. Also, soil temperature of higher mulch rate was better regulated than lower mulch rate one. In field conditions, Cook et al. (2006) observed that 2-8 t/ha of wheat straw increased the soil moisture and positively regulated the top soil temperature. Under natural rainfall field conditions in northeast Brazil, dos Santos et al. (2010) noted that the usage of 3.2 t/ha bean straw mulch influenced the soil moisture level variations both is dry and rainy seasons. Similarly, Souza et al. (2014) used 9 t/ha bean straw in northeast Brazil and found that the mulching proved to be efficient in reducing soil moisture spatial variability by retaining the soil moisture.

2.3. Soil erosion modelling

Rainfall-induced soil erosion models describe multi-variable phenomena by combining surface hydrology, soil characteristics, raindrop impact and topography. Merritt et al. (2003) classified the soil erosion models in three categories i.e. empirical, conceptual and physically based models. Empirical models have a simple structure and less input data requirement. As limited data are available in many gauged and ungauged catchments, these models are widely used to predict soil erosion on catchment scale. Annual rainfall data, topographic data from digital elevation models along with soil type, land cover and vegetation cover data through remote sensing are utilized by empirical models. Empirical models do not account for the variation of physical characteristics of drainage basin such as variability of slope and heterogeneity of soil. Calibration of parameters for empirical models is done through field experiments. Universal soil loss equation (USLE) model and its revised version RUSLE incorporating rainfall erosivity parameter are widely used on various hillslope surface geometries found in different regions of the world for soil erosion risk assessment (e.g. Sabzevari and Talebi, 2019; Biddoccu et al., 2020; Efthimiou et al., 2020; Mohammed et al., 2020).

Conceptual models lie between empirical and physically based models. This type of models divides the catchment into series of storage units with each storage unit requiring some specific data based on its physical features (Aksoy and Kavvas, 2005). Semi empirical equations are used in which model parameters are obtained through field data and calibration. Common examples of conceptual models are AGNPS (Young et al., 1989) and SWRRB (Arnold and Williams JR, 1991).

Physically based soil erosion models are complex models that require intense data of all measurable parameters that contribute to soil erosion process. A detailed review on various physically based soil erosion models atcatchment scale has been presented by Aksoy and Kavvas (2005). Soil erosion by water is a complex process that mainly entails the processes of surface runoff and infiltration. Therefore, a physically based soil erosion model requires the coupling of three models i.e. infiltration, overland flow and soil erosion. Empirical models based on Horton's equation (e.g. Horton, 1933, 1941; Bauer, 1974; Gabellani et al., 2008) or physical based models relying on the law of conservation of mass and Darcy law for the water movement in porous soils (e.g. Green and Ampt, 1911; Richards, 1931; Philip, 1957; Smith, 1972; Smith and Parlange, 1978) can be used for water infiltration modelling. The overland flow can be modelled by using the kinematic and diffusive wave approximations or the 1D and 2D Saint-Venant shallow water equations (e.g. de Lima and Singh, 2002; Chen et al., 2016; Abrantes et al., 2021).These equations express the laws of conservation of mass and momentum for overland flow. For the soil erosion part, the continuity equation of sediment transport is used to express the detachment-transport-deposition processes of sediments induced by the raindrops impact and overland flow (e.g. Bennett, 1974; Foster et al., 1982; Tromp-Van Meerveld et al., 2008; Brooks et al., 2016; Wu et al., 2020).

2.4. Rock fragments and surface-subsurface hydrological processes

2.4.1. Surface rock fragments cover

Surface rock fragments cover is the proportional area of rock fragments resting on soil surface in terms of percentage (shown in Fig. 2.4). Rock fragments cover as a mulching technique has been widely used as a soil and water conservation measure in erosion prone agricultural lands (e.g. Liu and She, 2017; Rodrigo-Comino et al., 2017; Xia et al., 2018).

However, surface rock fragments cover usage as mulch has shown both positive and negative effects on some key soil hydrological processes i.e. rainfall induced runoff and soil erosion. For example, laboratory experiments (e.g. Poesen et al., 1990; Jomaa et al., 2012a, 2012b, 2013) found that the increase of rock fragments surface cover reduces runoff volume and soil erosion and increases water percolation on moderate slope gradients. They observed that increase of rock fragments cover retard/divert Horton’s flow velocity and reduce physical degradation of eroded soil surfaces. On the contrary, Laboratory experiments of Jean et al. (2000) showed that increase in surface rock fragments cover on steep soil slopes increases runoff and decreases infiltration. Poesen and Lavee (1991) studied the runoff and soil erosion response in the presence of rock fragments placed over square polystyrene mulch. They observed the probability of runoff generation and soil erosion increased with increase in rock fragment cover.

Fig. 2.4. Different distribution patterns of 50% surface rock fragments cover on a converging plane soil surface in controlled laboratory conditions (Photographs taken by the author of this thesis on the 10th June, 2017).

Several field studies (e.g. de Figueiredo and Poesen, 1998; Mandal et al., 2005; Mayor et al., 2009) observed that the runoff volume and soil erosion reduces, while infiltration increases with the increase of rock fragments cover. Guo et al. (2010) and Wang et al. (2012) also found the reduction of runoff volume and soil erosion with increase of rock fragments coverage from 0% to 40%. However, other field studies (e.g. Iverson, 1980; Wilcox et al., 1988; Loosvelt, 2007) found a positive relation of surface rock fragment with runoff and soil erosion. Zavala et al. (2010) observed that the runoff volume and soil erosion increased when rock fragments coverage increased above 60%. This positive effect of rock fragments coverage was also observed on fire induced water repellent soil (Gordillo-Rivero et al., 2014), where increase in rock fragments cover increased runoff and soil erosion.

Apart from soil erosion processes, other hydrological processes such as evaporation, soil temperature and soil structure are affected by the presence of rock fragment cover. Several studies (e.g. Roundy et al., 1997; Nachtergaele et al., 1998; Li et al., 2001) observed that surface rock fragments cover allows the water to infiltrate into the soil through their pores but retard evaporation. Li (2002) found surface fragments cover reduces dew deposition. Surface rock fragments cover acts as an insulator for the soil beneath them (Li, 2003). Mehuys et al. (1975) found that at daytime (heating period), temperature of soil under surface rock fragments is lower than the adjacent unprotected soil surface. At night time (cooling period) higher soil temperature beneath surface rock fragment was found compared to adjacent soil.

2.4.2. Rock fragments content

Rock fragment content or stoniness, referred as amount of rock fragments in soil profile, is defined by percentage, either by mass or volume (Torri et al., 1994). Presence of rock fragment content has a great impact on soil structure and soil water characteristics which, in turn, makes the water flow and solute transport process to understand in stony soils more complex than in homogenous non-stony soils (e.g. Ma et al., 2010; Hlaváčiková et al., 2014, 2019). Soil water storage reduces with increase in stoniness due to reduction in the available soil pore volume (Hlaváčiková et al., 2014, 2016, 2018). Novák et al. (2011) found through numerical simulations that increase in rock fragment content in soil decreases the saturated hydraulic conductivity. Increase in stoniness reduces the effective cross-sectional area of soil profile through which water flow, making the water flow path more elongated, which can result into lower hydraulic conductivities (Ma et al., 2010). Consequently, the infiltration rate also decreases. On the contrary, other studies (e.g. Shi et al., 2008; Beibei et al., 2009; Verbist et al., 2013) noted that shrink and swell occurring due to temperature fluctuation in stony soils produces temporal preferential pathways along the rock-soil interface, leading to higher hydraulic conductivities. Zhongjie et al. (2012) noted that increase in rock fragment content creates more macropores and increases the average size of macropores in soil profile, leading to higher infiltration rate. Furthermore, Shi et al. (2008) found that soil evaporation rate decreases with increase in stoniness of soil They argued that increase in stoniness increases the macropores and hydraulic conductivity of soil whereas, decreases the soil water retention capability and capillary porosity. As a result, soil water drainage increases and soil evaporation rate decreases.

Soil erosion process is also affected by the stoniness in soil. Han et al. (2019) through laboratory experiments studied the erosion response of clay loam soil mixed with different rock fragment volumetric contents (0, 5, 10, 20, 30 and 40%) on a 15° slope angle. They found that soil erosion rate decreased with increase in rock fragments content. Lv et al. (2019) found that increase in rock fragment content up to 30% deceased soil erosion rate in clay loam soil heaps. However, positive relation was found between erosion rate and rock fragment content increase in sandy loam soil heaps. They concluded that increase in rock fragments content in different soils affect the soil erosion process differently.

2.4.3. Rock fragments position at topsoil

The position of rock fragments has an ambivalent effect on the soil hydrological processes. There are three positions of rock fragments in topsoil layer: 1) rock fragments resting on top of soil surface; 2) rock fragments partially embedded in topsoil; and 3) rock fragments fully embedded in topsoil layer.

Poesen et al. (1990) conducted laboratory experiments for four rock fragment cover percentages with two rock fragment positions, i.e. top of soil surface and partially embedded in topsoil. They noted delay in runoff generation, decreased runoff and increased infiltration when rock fragments rested on top of soil surface, whereas, runoff generated quickly, runoff volume increased, and infiltration decreased when rock fragments partially embedded inside topsoil. They argued that splash erosion caused by rain drop impact on unprotected soil surface creates a surface sealing. This phenomenon decreases water infiltration. Presence of rock fragments on top of soil surface protects the soil surface below them from surface sealing, resulting in increase of infiltration through the protected soil surface. In case of partially embedded rock fragments, area below them becomes impermeable, resulting in higher runoff volume. Rock fragments completely embedded in topsoil produces higher runoff volume and lower water percolation than those placed on top of soil surface (e.g. Valentin, 1994; de Figueiredo and Poesen, 1998). This happens because completely embedded rock fragments are unable to protect soil surface from surface sealing. Also, soil moisture rapidly increases in topsoil region above the embedded rock fragments and, therefore, soil cohesion decreases making the topsoil more prone to erosion (Smets et al., 2011).

2.4.4. Rock fragments size and shape

Several studies reported that soil hydrological processes are sensitive to the rock fragments size and shape. For example, Chen et al. (2005) studied the evaporation rates of soil covered with different sizes of surface rock fragments. They found that soil covered with 2-5 mm rock fragments size has significantly lower evaporation rates than those soils covered with the rock fragments size of 5–20 mm and 20–60 mm. de Figueiredo and Poesen (1998) observed in their laboratory experiments that smaller surface rock fragments increased infiltration and reduced runoff volume and soil erosion compared to larger ones. At plot scale, Guo et al. (2010) also found that smaller surface rock fragments play an important role in countering the soil erosion problem than large ones. In storm event, water flow generated on the surface of small rock fragments is smaller than the larger ones that discharges onto the surrounding soil surface of each rock fragment. This flow will generate Hortonian overland flow, only if, it exceeds soil infiltration capacity which will happen more often for the larger rock fragments than smaller ones (e.g. Poesen and Lavee, 1991; Katra et al., 2008). Furthermore, tortuosity and discontinuity of surface water flow becomes more visible with increase in rock fragment cover (Bunte and Poesen, 1993). Size of rock fragments also affects the hydraulic conductivity of soil when they are embedded in the soil matrix. Numerical simulated study of Novák et al. (2011) showed that effective hydraulic conductivity of soil profile for a given rock fragments content is smaller when containing single large rock fragments compared to multiple smaller rock fragments.

Studies by de Figueiredo and Poesen (1998) and Jean et al. (2000) showed that the shape of surface rock fragments does not impose significant impact on runoff and soil erosion. However, rock fragments embedded in soil profile affect the hydraulic conductivity of soil, thus affecting the soil water movement. Hlaváčiková et al. (2016) conducted numerical experiments on soil profiles containing different shapes of rock fragments i.e. a sphere, an ellipsoid with two different positions, and a triangle. Simulations were done for four different (0.07, 0.16, 0.24, 0.31 cm^3 $cm\text{-}^3$) rock fragment content in soil profile. Their results showed that relative effective saturated hydraulic conductivity were different for different shapes of rock fragments for every rock fragment content simulation.

2.5. Measurement techniques for surface hydrological processes

2.5.1. Rain drop measurement techniques

Raindrops distribution, size, velocity, kinetic energy and angle of impact have a significant importance on surface hydrological processes. Kathiravelu et al. (2016) have categorized raindrop measuring techniques into manual and automated measuring techniques. Manual measuring techniques are simple, time consuming and their accuracy is limited. Manual measuring techniques are: 1) Flour pellet method develop by Bentley (1904) uses flour samples to measure raindrop size distribution. Large number of samples is required due to variability in results and overlapping of raindrops. Sampling is done for 1-2 seconds. 2) Stain method developed by Lowe (2007) uses absorbent paper covered with water soluble dye. The raindrops make the impact on chemical paper and leave a mark which can be counted to measure size distribution of raindrops. However, its accuracy is compromised when applied for long duration as raindrops start to overlap with each other. 3) Oil immersion method by Fuchs and Petrjanoff (1937) uses container low viscous oil to capture raindrops. Raindrops makes a spherical shape whose size can be measured by taking photograph or microscope.

Automated measuring techniques utilize electrical, optical imaging and acoustic techniques to measure size distribution and velocity of raindrops for longer duration of time. These techniques can give terminal velocity data which are vital for estimation of kinetic energy of raindrops. These techniques are: 1) Acoustic disdrometer (e.g. Winder and Paulson, 2012, 2013) utilizes piezoelectric sensor to emit and receive an electric signal when raindrop makes an impact on a plate, 2) Displacement disdrometer (Bass, 1971) uses magnetic induction to convert the force created by raindrop impact into electric signal to measure size, velocity and kinetic energy of raindrop, 3) Optical disdrometer (e.g. Beguería et al., 2015; Angulo-Martínez et al., 2016) is a non-intrusive technique. Optical imaging and optical scattering are its two types. Optical imaging uses two high speed cameras which take images of raindrops passing between them. These images are translated to measure size, velocity and kinetic energy of raindrops. Optical scattering uses horizontal light sheets (usually a laser beam) which gets scattered by rain drops interception. This interception causes an electrical signal by receiver which is translated to measure shape, velocity and kinetic energy of raindrop.

2.5.2. Soil Surface measurement techniques

Soil surface morphology/roughness measurement techniques can be categorized into contact and non-contact measurement techniques. The contact measurement techniques are pin meters (e.g. Gilley and Kottwitz, 1996; Stenberg et al., 2016), chain method (e.g. Saleh, 1993; Wu et al., 2020) and automatic relief meters (Hansen et al., 1999). These techniques are low cost but time consuming, prone to human errors and can deform the soil surface. Non-contact methods are more accurate and less time consuming. These methods can make digital elevation models with good resolution. Such methods are the laser techniques (e.g. Stenberg et al., 2016; Abban et al., 2017; Li et al., 2020b), photogrammetry methods (e.g. Bauer et al., 2015; Gilliot et al., 2017) and shadow analysis (e.g. García Moreno et al., 2008; Denis et al., 2014). de Lima and Abrantes (2014a) introduced an innovative technique to measure soil surface roughness at laboratory scale using infrared thermography and found satisfactory results when compared with manual profile meter.

2.5.3. Discharge, Stage and velocity measurement techniques of natural stream

Discharge estimation of a natural stream is commonly done through velocity area method (Le Coz et al., 2012), which requires the measurements of flow velocity, stage at stream's vertical cross sections and stream width. Stage i.e. water depth of stream above the established datum at gauging site, can be measured by reading the height gauge through naked eye or by using various automatic gauges such as float-type, pressure-type and ultrasonic-type (Herschy, 2008). Flow velocity at various water depths of a stream is commonly measured through mechanical (rotor-type) or electromagnetic current meters. Mechanical current meter (Saretta et al., 2016) uses the vertical or horizontal axis rotation of bucket wheel or impeller whereas, electromagnetic one (MacVicar et al., 2007) uses electromagnetic induction for flow velocity measurements. Dilution gauging (Comina et al., 2014) is another streamflow velocity measurement method that involves the induction of chemical or radio isotope tracers and their subsequent detection at known distance downstream. However, if mixing of tracer in stream water profile is not homogeneous, results can have errors. Acoustic Doppler Velocimetric method (Dobriyal et al., 2017) for streamflow velocity measurement using sound waves have shown reliability but is expensive compared to other above-mentioned methods. Large Scale Particle Image Velocimetry (LSPIV) and Particle Tracking Velocimetry (PTV) using optical cameras and particle tracers are other techniques which are used in recent years to measure surface velocities of natural streams (e.g. Jodeau et al., 2008; Tauro et al., 2017). Although, these techniques proved to be dependable but in-depth knowledge of image processing and good lightingconditions are essential requirements. Using infrared camera and particle thermal tracer (ice dices) for PTV technique solved the lighting condition problem for natural stream surface velocity measurement (Tauro and Grimaldi, 2017).

2.5.4. Shallow flow velocity measurement techniques

According to Flury and Wai (2003), density closer to water, detectability and low toxicity are the characteristics of suitable tracer for shallow overland flow velocity measurement. Most used methods to determine velocity of shallow overland flow is dye and salt tracing for the laboratory and field experiments (e.g. Abrahams et al., 1986; Tatard et al., 2008; Abrantes et al., 2018a; Huang et al., 2018; Yang et al., 2020). Normally, leading edge or sometime the centroid of dye mass is traced from its injection to sampling point, either by naked eye or optical camera. Electric conductivity meter is used for tracking the leading edge and centroid of salt tracers. Both dye and salt tracers have non conservative nature and are affected by the advection and diffusion processes. Correction factor dependent on flow characteristics and bathymetry is required for reliable estimation of mean flow velocity. In recent years, thermal tracers (e.g. hot water) detected by infrared camera are used for shallow flow velocity measurements. Thermal tracer in thermal images is clearer than the dye tracer is in the optical images (e.g. de Lima and Abrantes, 2014a; Abrantes et al., 2019). Particle Tracking Velocimetry (PTV) using optical or infrared cameras and particle tracers are other techniques which are used in recent years. For very shallow flow (< 2 mm) velocity measurements, Mujtaba and de Lima (2018, Chapter 5 of this Thesis) used cold oil droplets as particle thermal tracer for infrared based PTV technique and found to be reliable when compared with conventional PTV technique (using optical camera and polystyrene beads as tracer) and dye tracing technique, shown in Fig 2.5.

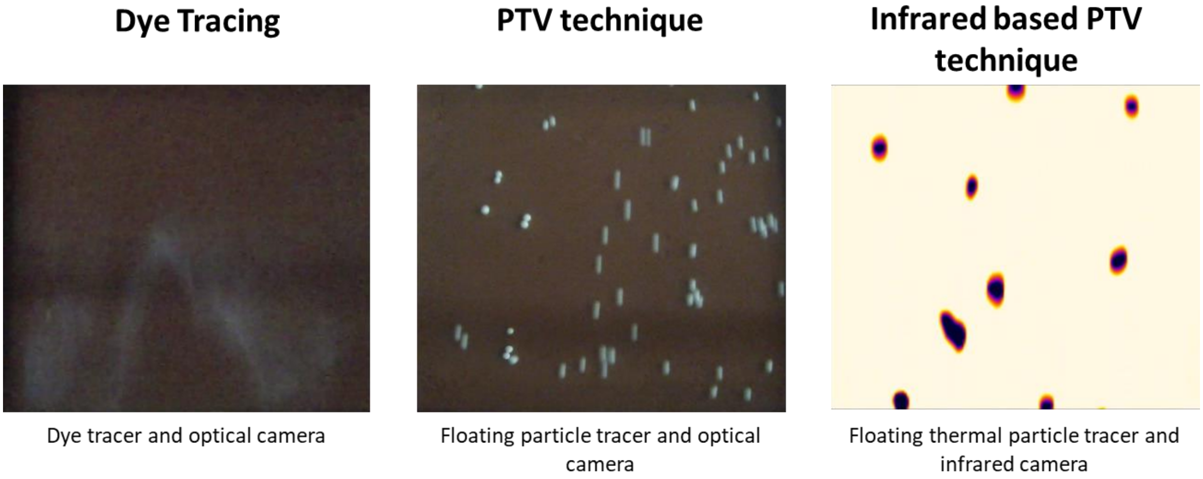

Fig. 2.5. Overview of different techniques used for shallow flow velocity measurements (Photographs taken by the author of this thesis on the 10th December, 2016).

2.5.5. Soil moisture measurement techniques

Soil moisture measuring techniques can be categorized into direct and indirect methods. In case of direct method, wet soil sample is weighed and put in oven to dry and weighed again. Indirect methods include Time Domain Reflectometry (TDR) and Ground Penetrating Radar (GPR). TDR measures soil moisture content by measuring the electric pulse travelling time between two probes, whereas, GPR uses electromagnetic signals for soil moisture estimation. A review of Dobriyal et al. (2012a) concluded that the direct method is inexpensive and accurate but has limited spatial coverage and data retrieval is slow. On the other hand, TDR and GPR methods give accurate and instantaneous data for large spatial cover but are expensive. Installation of

TDR probes into stony soils in the field is difficult and pose a serious hindrance to measure soil moisture (e.g. Cousin et al., 2003; Ma et al., 2010).

2.5.6. Soil stoniness measurement techniques

In stony soils, soil sampling by taking a large representative elementary volume to estimate rock fragments content at different soil layers is common, shown in Fig. 2.6 (e.g. Hlaváčiková et al., 2018; Koestel et al., 2020). Buchter et al. (1994) recommended that the dry mass of a stony soil sample should be at least 100 times the mass of the largest particle. Other techniques such as remote sensing, brightness index and geoelectrical methods are also used to estimate stoniness of soil profile (Tetegan et al., 2012).

Fig. 2.6. Large representative elementary volumes at field sites taken for rock fragments content measurement in stony soils (Photographs taken by the Institute of Hydrology, Slovakia research team).

3. Importance of the hydraulics of converging and diverging flows on soil erosion override effects of rock fragment cover patterns: experimental assessment[1]

3.1. Abstract

Soil erosion in the presence of surface rock fragments and organic mulches has been mostly studied for 1-dimensional surface flows. This study evaluates the influence of different distribution patterns of rock fragment surface cover on runoff and soil loss from converging and diverging plane surfaces. The laboratory apparatus was comprised of a rainfall simulator and a soil flume, which geometry was based on a circular sector, of 2.02 m length and limited by 0.10 m and 2.10 m arc lengths. The soil flume had runoff collection outlets at both ends in order to perform experiments on both converging and diverging plane surfaces. Rainfall events with a mean intensity of 87 mm hr^{-1} and duration of 10 min were simulated at a 20% slope gradient for six scenarios on both soil surfaces' geometries. These scenarios were (i) control (bare soil), (ii) three distribution patterns (i.e. evenly diamond distributed, line rows and radial rows) of 40% rock fragment surface cover, (iii) organic mulch over bare soil and (iv) organic mulch over rock fragment surface cover. Results indicate that all tested rock fragment surface cover patterns increased runoff volumes and soil loss with respect to control scenario while mulch cover scenarios decreased runoff and soil loss. Diamond pattern rock fragment cover scenario caused the largest increase and the radial rows pattern the least increase compared to the control scenario, on both converging and diverging surfaces. For all six scenarios, soil loss on a converging surface was ~10-30 times higher than on the diverging surface. Our study suggests that soil surface geometry had more influence on soil erosion than different distribution patterns of specific percentage of rock fragment surface cover, in part due to flume's border effect.

---

[1] **Mujtaba, B.**, de Lima, J.L.M.P., de Lima, M.I.P., Vargas, M.M., 2019. Importance of the hydraulics of converging and diverging flows on soil erosion override effects of rock fragment cover patterns: experimental assessment. Zeitschrift für Geomorphol. 62 (3), 183–197. https://doi.org/10.1127/zfg/2019/0578

3.2. Introduction

Understanding soil erosion processes in the presence of different soil surface covers (e.g. vegetation, rock fragments, organic residues, etc.) is important for planning and implementing soil conservation strategies. Extensive laboratory and field studies have been done in the past to study the influence of rock fragments on runoff generation and soil erosion (e.g. Box, 1981; Poesen et al., 1990; Poesen and Lavee, 1991; de Figueiredo and Poesen, 1998; Loosvelt, 2007; Zavala et al., 2010; Rodrigo-Comino et al., 2017). It was observed that the effect of surface rock fragments (i.e. rock fragments resting on soil surface) on soil erosion is complex and inconsistent, i.e. rock fragments could both increase or decrease runoff and soil loss. Numerous field studies found that surface rock fragments decrease surface runoff volume, reduce soil erosion and enhance water percolation (e.g. de Figueiredo and Poesen, 1998; Mandal et al., 2005; Mayor et al., 2009). Other field studies (e.g. Iverson, 1980; Wilcox et al., 1988; Loosvelt, 2007; Zavala et al., 2010) found a positive relation of surface rock fragment with runoff and soil erosion. Even in laboratory conditions, the effects of surface rock fragments influence on runoff and soil loss are multifaceted, as summarized in Table 3.1. It has also been observed that the surface rock fragment distribution-patterns applied in laboratory simulations differ among studies.

Jean et al. (2000) compared runoff volumes of two rock fragments distribution patterns (regular and interlaced) for a similar percentage of surface cover. They found that the runoff volume was affected by rock fragments cover and distribution pattern over the soil surface and slope. Abu-Zreig et al. (2011) observed that farmers in highland of northern Jordan used contour rock fragment rows (i.e. rock fragment placed in rows at regular intervals) to protect their farms from soil erosion. Those results suggest that the distribution pattern of rock fragments has a role in soil conservation.

Hillslopes are generally found in rocky catchments with shallow surface soil layers. Landslides are quite common in these hillslopes, resulting in release of debris mass. Weak soil/rock layers are present at various soil depths, along which rock slope failure can occur (e.g. Wang et al., 2010; Xu et al., 2010; Crusoe et al., 2016). Moreover, the risk of plane hillslope failures can be larger where slope cutting is conducted due to civil engineering works (e.g. Shukla et al., 2009; Tang et al., 2016). The surface resulting from slope failure has abundance of rock fragments of various sizes distributed on the soil profile. Plane failure of rock slope is a simple mode of failure (Raghuvansi, 2019).

Table 3.1. Selection of studies in the literature on the influence of surface rock fragments (resting on top of the soil surface) on runoff and soil loss under simulated rainfall in laboratory condition. Control is bare, rock free soil.

Reference	Rainfall duration	Rainfall intensity (mm hr^{-1})	Slope (%)	Initial moisture condition	Rock fragments characteristics			Flume characteristics	Runoff	Soil loss
					Cover (%)	Size (mm)	Distribution pattern			
Poesen et al. (1990)	90 min	36.4	5.7	Top soil layer (30 mm) air dried	20; 34; 49; 65; 83	33×70×100	Irregular	Rectangular 0.95×0.6 m^2	Decreased	-
Poesen and Lavee (1991)	60 min	71.3	4.5	Air dried	30; 49; 70; 88	Rock fragment over square polystyrene mulch with side of 30; 59; 117; 223	Running bond	Rectangular 1.8×1.27 m^2	Probability of runoff generation increased with increase in mulch size	Increased for 223 mm mulch for 30, 49 and 70% cover and 117 mm mulch for 30% cover
Jean et al. (2000)	120 sec	109.2	5; 10; 20	20%	0; 10; 20; 30	9.5-20	Regular and Interlaced	Rectangular $1.2\times0.8\times0.2$ m^2	Decreased Increased	- -
Jomaa et al. (2012a)	2-3 hrs	28; 74	2.2	6.52-26.36%	20; 40	50-70	Triangular	Rectangular 6×1 m^2	Decreased	Decreased
Jomaa et al. (2012b)	2 hrs	14.56- 68.7	2.2	6.81-8.84%	20; 40	50-70	Triangular	Rectangular 6×1 m^2	Decreased	Decreased
Jomaa et al. (2013)	2 hrs	28; 74	2.2	7.7-26.4%	40	50-70	Triangular	Rectangular 6×1m^2	Decreased	Decreased

This kind of failure leads to sliding action along the failure surface. Researchers (e.g. Goodman and Shi, 1985; Sharma et al., 1995; Raghuvansi, 2019) have categorized the lateral release surfaces of plane rock slope failure (Goodman and Shi, 1985). The resulting surfaces are converging plane, plane and diverging plane with border walls which becomes part of hillslope overall geometry. Many researchers (e.g. Young and Mutchler, 1969; D' Souza and Morgan, 1976; Rieke-Zapp and Nearing, 2005; de Lima et al., 2017) have studied the soil erosion response on different profile curvatures (convex, plane and concave) of linear shaped soil surface (i.e. rectangular shape). All of these researchers observed that a convex curvature of a linear-shaped soil surface was the most hazardous in terms of the generation of runoff and sediments. Rectangular plane shape surfaces have been adopted by many researchers as the standard geometry (see Table 3.1) in laboratory experiments to study the response of soil loss and runoff in the presence of rock fragments. To our knowledge, no study has been done at a laboratory scale to study the effect of soil erosion under simulated rainfall on converging and diverging shaped plane soil surface geometries with and without surface rock fragments.

Mulching as a soil erosion mitigation method has been adopted for decades on hillslopes. Many researchers (e.g. Swanson et al., 1965; León et al., 2013; Montenegro et al., 2013; Prats et al., 2017; Abrantes et al., 2018b) in laboratory and field conditions have used different types of organic mulch such as leaf litter, woodchips, bark chips and rice straw and found that mulching is a remarkable method to control soil erosion. However, these studies were also done on a rectangular plane-shaped soil surface without rock fragment cover. No study has been done to explore the capability of organic mulch to reduce soil erosion on converging and diverging shaped plane soil surface with and without rock fragment cover.

The aims of this study are to evaluate the variations in runoff and soil loss by converging and diverging flows, by the influence of (i) different spatial distribution patterns of a single percentage of rock fragment surface cover, (ii) organic mulch cover over bare soil, and (iii) organic mulch cover over rock fragment surface cover. Control run was rock free bare soil. Experiments were conducted under controlled laboratory conditions, using simulated rainfall and two different soil surface geometries (e.g. converging and diverging plane surfaces).

3.3. Setup and materials

3.3.1. Laboratory setup

A rainfall simulator and 2.24 m^2 soil flume were used for this experimental work, as shown in

Fig. 3.1a. The flume's geometry was based on a circular sector, of 2.02 m length and limited by 0.10 m and 2.10 m arc lengths; flume's depth was 0.12 m. The flume was made of zinc-coated iron metal sheets; a geotextile rug was placed over the iron mesh at the bottom of the soil flume for free drainage. The flume had runoff collection outlets at both ends. By tilting the flume in opposite directions, the setup allowed to perform experiments on both converging and diverging plane surfaces (Fig. 3.1b), whereby the convergence and divergence of the surface flow is due to lateral border confinement. Experiments were conducted at 20% slope gradient, typical of a mountain environment.

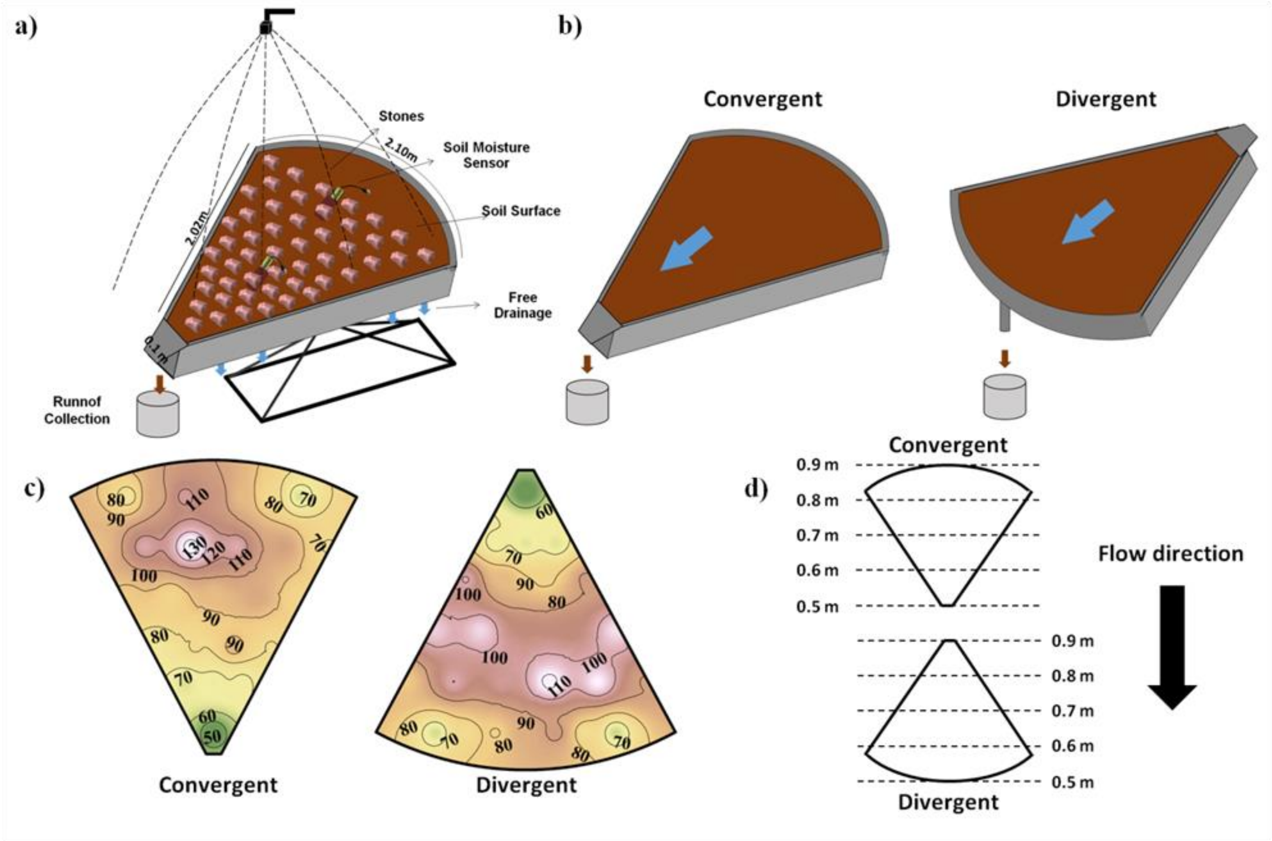

Fig.3.1. Experimental work: a) Sketch of laboratory setup; b) converging and diverging plane surfaces (same soil flume). c) Spatial distribution of rainfall intensity (isohyets in mm hr^{-1}). d) Dashed lines refer to contour lines and solid lines refer to border wall of flume's geometry.

3.3.2. Soil

A sandy loam soil collected from the banks of the Mondego River in Coimbra (Portugal) was used for the experiments. This material had a 1100 kg m^{-3} bulk density and was composed of 7% clay, 9% silt, 73% sand and 11% gravel. The pre-sieved sediment was passed through a 5 mm mesh to remove roots and rock fragments > 5 mm. The sediment was then spread manually in the soil flume in layers and compacted gently with a steel plate. A sharp-edged wooden blade was used to level the soil surface by removing the excess soil. The resulting sediment surface was flat without any micro-topographic protuberances and the entire deposit was 0.1 m deep. Two soil-moisture sensors were installed at the distance of 0.3 m and 1.3 m from the upstream end of the soil flume (converging surface) and reached down to depth of 0.07 m. Soil moisture sensor measured water content at 0.03 m depth of sediment fill. These soil moisture sensors ensured that each experimental run was performed at approximately similar initial soil moisture condition.

3.3.3. Rainfall

The rainfall simulator was equipped with a downward-oriented 3.58 mm orifice diameter HH-22 Full Jet nozzle (e.g. de Lima et al., 2013; Isidoro et al., 2013; Carvalho et al., 2014). The sprinkler was fixed on a connecting rod in a stand placed 2.20 m above the flume surface and produced a full cone spray. Raindrop mean diameter and mean fall velocity, calculated by Carvalho et al. (2014), were 0.74 mm and 1.92 m s^{-1}, respectively, at constant nozzle operational pressure of 50 kPa for the same nozzle of same rainfall simulator used in this study. To maintain constant nozzle pressure at 50 kPa, a hydraulic system was used that pumped water from a constant-head reservoir with a submerged pump. Under these conditions, the experiments were conducted at a mean simulated rainfall intensity of 87 mm hr^{-1} applied during 10 min. This rainfall intensity was found to be comparable with the 20-years return period 10 min event at the city of Coimbra, in Portugal (e.g. Brandão et al., 2001). The rainfall (uneven) spatial distribution on the flume (Fig. 3.1c) is a direct consequence of the rainfall simulator used (i.e. one full-cone nozzle spray, positioned in the middle). Rainfall variability is common in nature. Controlled laboratory conditions guaranteed that the rainfall distribution pattern was the same for all laboratory runs, for comparison purposes.

3.3.4. Rock fragments

In our study, sedimentary rock fragments collected from the banks of the Mondego River, near Coimbra (Portugal), were used for the laboratory simulations. Three different spatial distribution patterns of rock fragments were used on both converging and diverging plane surfaces (Fig. 3.2): evenly diamond-patterned distributed (d), placing rock fragments at regular intervals to form line rows (l) and radial rows (r). A total of 76 irregular-shaped rock fragments with mean size of 80×150×15 mm^3 were used to achieve a 40% rock fragment surface cover for each of the three rock fragments' spatial distribution patterns.

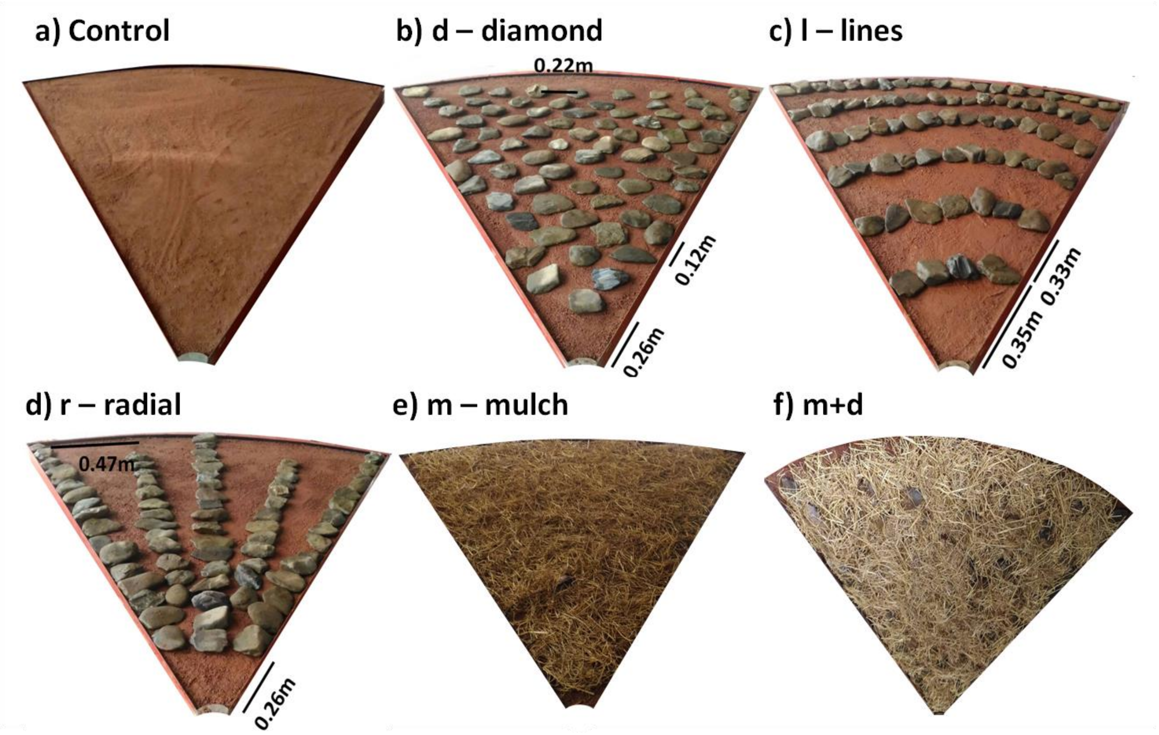

Fig. 3.2. Soil surface scenarios for laboratory experiments: a) Control (bare soil; rock fragment free soil surface), b) d- diamond pattern (evenly distributed) of 40% rock fragment cover, c) l–line rows pattern (i.e. rock fragment rows on regular interval) of 40% rock fragment cover, d) r–radial rows pattern of 40% rock fragment cover, e) m–organic mulch cover of soil without rock fragments and f) m+d–organic mulch over diamond pattern of 40% rock fragment cover.

In our study, the rock fragments' mean size is comparable to those used in other studies (e.g. Poesen and Lavee, 1991; Abu-Zreig et al., 2011). The rock fragments were placed on top of the prepared flume's flat soil surface. Each rock fragment was numbered. For each experimental run of a given scenario, every specific rock fragment was placed at the same position. This ensured the same initial conditions for each experimental run.

3.3.5. Organic mulch cover

Rice straw was used as organic mulch. Air dried mulch was sieved with a 15 mm mesh to use only rice straws above 15 mm of size (up to 300 mm). Rice straw mulch was applied uniformly at 2.5 ton ha^{-1}rate for two scenarios (Figs. 3.2e,f), i.e. over bare soil and over the diamond pattern rock fragment cover. For each experimental run that used mulch, the mulch was always air-dried and applied just before the rain started.

3.4. Experimental and statistical analysis procedure

A total of six scenarios, i.e. control (bare soil), three patterns of rock fragment surface cover (diamond, line rows and radial rows), mulch over bare soil and mulch over rock fragment cover were tested on both converging and diverging plane surfaces, as shown in Fig. 3.2. In order to even-out inter-experimental variability, runs for each scenario were repeated three times, amounting to a total of 36 experimental runs (18 on each surface geometry). Before the first experimental run, the soil was saturated gently with a hose connected to tap water until ponding started to occur. After that, soil was left to drain and air dry until soil moisture decreased to 13-17%, measured using two soil moisture sensors. This soil moisture range is comparable to field capacity of sandy loam soils (e.g. Salter and Haworth, 1961). For subsequent runs, the soil surface layer (roughly 3-4 mm) was removed and replaced by air-dried soil. This was done to ensure a similar content of silt, clay and sand on the top soil surface layer for all runs. The air-dried soil surface layer was again compacted and levelled. After that, the soil saturation procedure was repeated to obtain approximately similar initial moisture conditions.

A total of seven runoff samples were taken for each run, measured at the lower end of the flume for 10 s at intervals of 2 min from the initiation of runoff. These runoff samples were dried at 80ºC to determine soil loss. Grain size analysis was performed on washed sediments through conventional sieving. After completion of each run, mulch or rock fragments placed along the border wall of the soil flume were carefully removed to measure the widths and depths of notable rills that formed along the border wall. The volume of these rills indicated the sediment weight eroded by the influence of the flume's border. Nearing et al. (1997) suggested that, in laboratory conditions, soil erosion could be described by stream power on planar surfaces of constant width; they found that higher stream power results in higher soil loss. Unit stream power ω (W m^{-2}) can be calculated by (e.g. Nearing et al., 1997; Bizzi and Lerner, 2015):

$$\omega = \rho g S q \qquad 3.1)$$

where ρ is water density (kg m^{-3}), g is gravitational acceleration(m s^{-2}), S is slope gradient and q is unit discharge ($m^3 s^{-1} m^{-1}$) at downstream end of soil flume (also in this study).

We used the steam-power approach on the converging and diverging plane surfaces, and calculated stream power at the downstream end of those surfaces. The widths at the downstream sections of the converging and diverging flume ends were 0.10 m and 2.10 m, respectively.

The percentage of deviation of runoff initiation time, total runoff volume and total soil loss from the control scenario for all other scenarios were estimated by:

$$Dev(\%) = \frac{S_s - S_c}{S_c} \times 100 \qquad 3.2)$$

where $Dev(\%)$ is percentage of deviation from control scenario, S_c is parameter value of the control scenario and S_s is parameter value of other given scenarios.

A pair-wise comparison was performed using a one-way analysis of variance (one-way ANOVA) along with post hoc Tukey-Kramer honestly significant difference (HSD) test to determine if peak runoff, total runoff volume, peak soil loss and total soil loss differed significantly between the various surface cover scenarios and the control (bare soil) scenario for a given soil surface geometry (converging or diverging). The statistically significant difference between rock fragment cover patterns and between mulch cover scenarios for a given soil surface geometry (converging or diverging), for total runoff and total soil loss, was also examined. Finally, the statistical test determined if total runoff volume and total soil loss of all six scenarios on converging surface were significantly different from their corresponding values on diverging surface. All statistical analyses were tested at a significance level of 0.05.

3.5. Results

3.5.1. Hydrological response

Runoff hydrographs of all surface cover scenarios on converging and diverging plane surfaces are presented, in Fig. 3.3. Overall, the rising limb of all scenarios' hydrographs for converging surface were steeper than their corresponding ones for diverging surface. An approximate steady state condition (i.e. constant discharge) established around 3 minutes after the start of surface runoff for all scenarios. Once at that state, average runoff responses of all scenarios for the converging surface were similar to those for the diverging surface except for the evenly-distributed diamond rock pattern and the mulch cover on bare soil scenario, which were 1.12 and 1.08 times higher, respectively, on converging surface (see Fig. 3.3).

Details regarding runoff initiation time, total runoff volume and runoff peak of all scenarios are reported in Table 3.2. On both converging and diverging surfaces, runoff initiation time increased for all rock fragment cover pattern and mulch cover scenarios compared to the control scenario. Compared to converging surfaces, average runoff initiation time on diverging soil surfaces was approximately half for the three rock fragment scenarios.

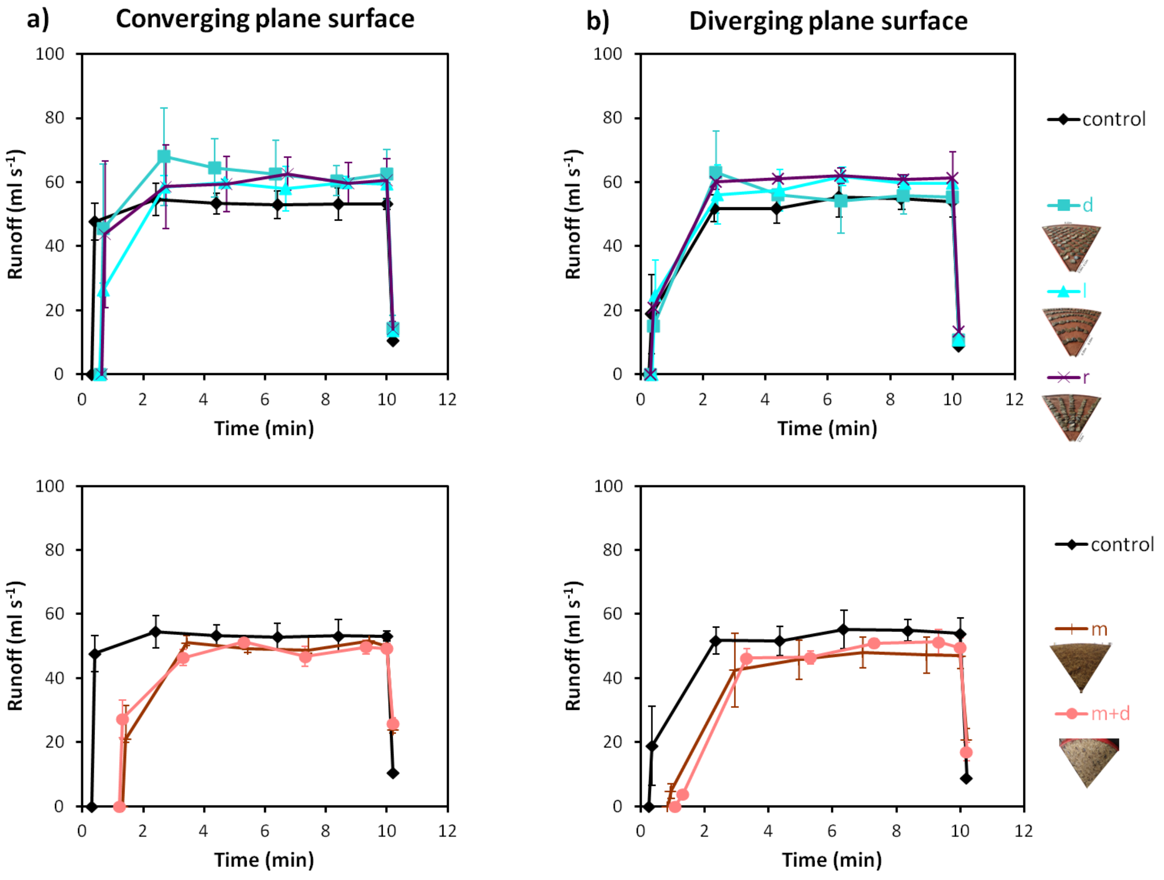

Fig. 3.3. Runoff (average and standard deviation bars of three repetitions) on a) converging and b) diverging plane surfaces, observed for (top) control (bare soil) and three rock fragment cover patterns (d,l and r) and (bottom) mulch cover (m and m+d) scenarios.

Table 3.2. Average ± standard deviation (three repetitions) of runoff initiation time, runoff peak and runoff volume for six scenarios observed on converging and diverging plane surfaces. Coefficient of variation (C.V.) of runoff volume for all scenarios is also presented. Bold is used to denote runoff volume of a scenario on converging surface that is significantly different ($p < 0.05$) from its corresponding value on diverging surface. [a] denotes the runoff peak and runoff volume of scenarios that are significantly different ($p < 0.05$) from corresponding values of the control (bare soil) scenario for a given surface geometry (converging or diverging).

		Converging plane surface				Diverging plane surface			
Scenarios	Treatments	Runoff initiation time (min)	Runoff peak (mL s^{-1})	Total runoff volume (L)	C.V. (%)	Runoff initiation time (min)	Runoff peak (mL s^{-1})	Total runoff volume (L)	C.V. (%)
1	Control	0.31±0.1	54.5±5.1	30.9±1.8	5.8	0.26±0.2	55.2±6.1	29.4±2.8	9.6
2	Diamond rock pattern	0.58±0.2	68.0±15.2	35.5±6.8	19.1	0.32±0.1	63.1±12.8	30.5±3.9	12.8
3	Line rows rock pattern	0.57±0.1	60.0±0.7	31.7±1.9	5.9	0.37±0.1	61.8±2.8	31.1±5.1	16.5
4	Radial rows rock pattern	0.64±0.3	62.6±5.1	33.2±5.9	17.7	0.32±0.1	62.0±2.5	33.3±1.0	3.0
5	Mulch	1.33±0.2	51.7±1.6	24.4±0.7[a]	3.1	0.85±0.3	48.0±4.7	22.7±3.7[a]	16.3
6	Mulch over rock cover	1.21±0.2	51.3±0.6	**24.5±0.2**[a]	0.8	1.08±0.2	51.3±3.8	22.9±0.4[a]	1.8

Correlations of runoff volumes of all surface cover scenarios with control scenario are shown in Fig. 3.4a. All rock fragment cover patterns increased runoff volume compared to control scenario by on average 8% for both converging and diverging surfaces. By contrast, mulch cover scenarios (mulch on bare soil and mulch on rock cover) significantly reduced runoff volumes by 21% and 22% on converging and diverging surfaces (Fig. 3.4a). Runoff peak was highest for the diamond rock pattern scenario on both soil surface geometries and lowest for the mulch cover scenarios (see Table 3.2).

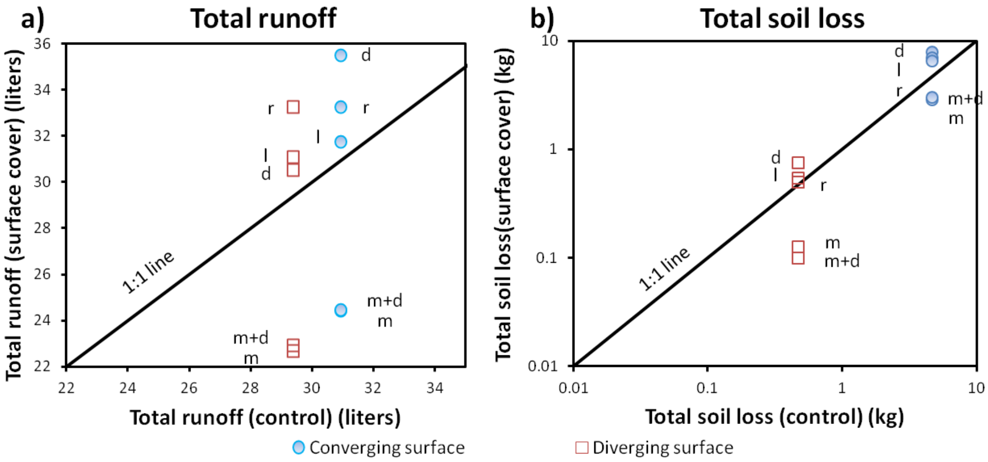

Fig. 3.4. Correlation of results for all rock fragment cover (d, l and r) and mulch cover (m and m+d) scenarios with control (bare soil) scenario for a) total runoff volume and b) total soil loss (note the log-log scale).

3.5.2. Erosion response

Temporal evolutions of average soil loss for all scenarios on converging and diverging plane surfaces are presented in Fig. 3.5. Soil loss fluxes of all scenarios were markedly higher (7 to 67 times) on converging surfaces compared to corresponding values on diverging surfaces. Washed sediments grain size distributions (in percentages) of every scenario except control scenario are shown in Fig. 3.6. On average, all surface cover scenarios on diverging surface transported ~10% more silt and clay than on converging surface. The diamond and lines rock patterns exported similar amounts of coarse sand from both surface geometries, but no coarse sand transport was observed for the other scenarios on diverging surfaces.

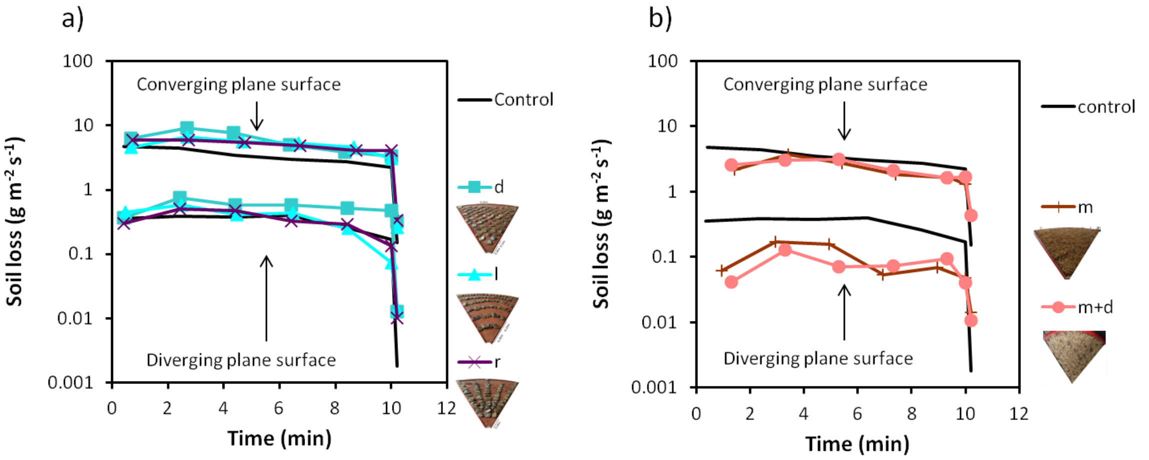

Fig. 3.5. Average soil loss observed for a) control (bare soil) and three rock fragment cover patterns (d, l and r) and b) control and mulch cover (m and m+d) scenarios on converging and diverging plane surfaces. Y-axis is log-log scale.

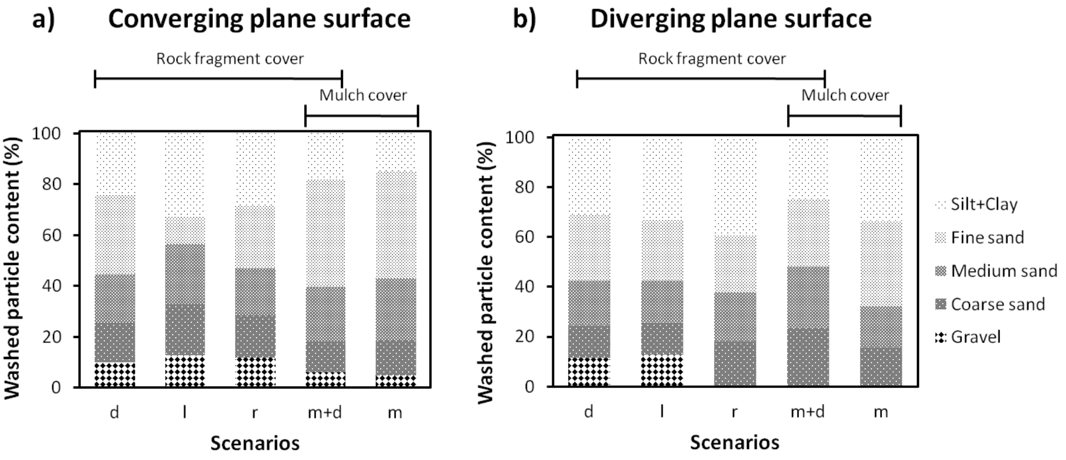

Fig. 3.6. Particle size distribution of transported sediments on a) converging and b) diverging plane surfaces, for three rock fragment cover patterns (d,l and r) and mulch cover (m and m+d) scenarios.

On average, all rock fragment cover patterns increased soil loss compared to the control scenario, about 55% on converging surfaces and 28% on diverging surfaces (see Table 3.3). By contrast, mulch cover scenarios significantly reduced total soil loss in relation to control scenario, on average by 36% on converging surface and by 76% on diverging surface. Soil loss was generally ~10-30 times higher on converging surfaces than on diverging surfaces.

Table 3.3. Average ± standard deviation (three repetitions) of soil loss peak and total soil loss observed for six scenarios on converging and diverging plane surfaces. Coefficient of variation (C.V.) of total soil loss for all scenarios is also presented. Bold is used to denote soil loss of a scenario on converging surface that is significantly different ($p < 0.05$) from its corresponding value on diverging surface. [a] denotes the soil loss peak and soil loss of scenarios that are significantly different ($p < 0.05$) from corresponding values of the control (bare soil) scenario for a given surface geometry (converging or diverging).

		Converging plane surface			Diverging plane surface			
Scenarios	Treatments	Soil loss peak (g m^{-2} s^{-1})	Total soil loss (kg)	C.V. (%)	Soil loss peak (g m^{-2} s^{-1})	Total soil loss (kg)	C.V. (%)	$\frac{TSL_c}{TSL_D}$
1	Control	4.8±0.4	**4.6±0.7**	14.7	0.4±0.2	0.5±0.2	38.7	9.8
2	Diamond rock pattern	9.0±2.4	**8.0±1.4**[a]	16.9	0.7±0.1[a]	0.8±0.4	47.9	10.6
3	Line rows rock pattern	6.7±3.0	**7.0±0.9**	12.2	0.6±0.0	0.6±0.0	3.8	12.8
4	Radial rows rock pattern	5.9±2.6	**6.6±1.6**	23.6	0.5±0.1	0.5±0.1	16.9	13.2
5	Mulch	3.7±1.1	**2.9±0.9**[a]	31.2	0.2±0.1	0.1±0.1[a]	89.0	22.5
6	Mulch over rock cover	3.1±0.5	**3.0±0.3**[a]	11.5	0.1±0.0[a]	0.1±0.0[a]	33.4	30.4

TSL_c is total soil loss on converging plane surface and TSL_D on diverging plane surface.

3.6. Discussion

3.6.1. Effect of different patterns of rock fragment cover on runoff and soil loss

In our study, all rock fragment surface cover patterns enhanced runoff and soil erosion with respect to bare soil conditions on both soil surface geometries. However, in laboratory studies, Poesen et al. (1990) and Jomaa et al. (2012b, 2013) used rock fragments of uneven surface and found a negative effect of surface rock fragments on runoff volume and soil loss on moderate slope gradients. They observed that surface sealing occurs on unprotected soil surface by raindrop splash, resulting in infiltration rate reduction. Presence of surface rock fragments protects the soil surface area below the rocks from surface sealing. Water moves through the areas below rock fragments which favors infiltration and reduces runoff. Also, water depth increases around rock fragments due to reduction of flow width which produces further increase in infiltration below rock fragments. Increased infiltration and presence of surface sealing reduced soil erosion. By contrast, Poesen and Lavee (1991) and Jean et al. (2000) observed that surface rock fragments can increase runoff and soil erosion if slope gradient is steep or large rock fragments of flat surface are used.

Sandy loam soil type in our study is prone to surface sealing, as observed by many researchers (e.g. Poesen et al., 1990; Poesen and Lavee, 1991). Due to high initial soil moisture and soil type, surface sealing probably occurred on unprotected soil surface in initial stages of our experiments. Large rock fragments used in our study had flat surface that contacted the soil surface; thus, less space was available for water infiltration between rock fragments and unsealed soil surface. This made it difficult for hortonian overland flow and flow from rock surface to penetrate the soil area below rock fragments. Due to the steep gradient and high rainfall intensity, unit stream power was high. Unit stream power became higher around the rock fragments due to less available flow width. In fact, larger rock fragments acted as pillars for oncoming runoff, causing scour around rock fragments, which resulted in higher soil loss compared to the control scenario on both surface geometries. This feature of scouring around surface rock fragments promoting erosion by overland flow was also observed by Bunte and Poesen (1993). Our study observed that the presence of large, flat rock fragments that contacted the soil surface may result in promoting runoff and soil erosion, especially under conditions of high soil erosion such as high initial moisture content, a surface prone to sealing, and a steep gradient.

Different patterns of rock fragment surface cover produced different responses in runoff and soil loss on a given soil surface geometry (converging or diverging surface), as shown in Fig. 3.7. Runoff volume was highest for diamond rock pattern scenario on converging surface while on diverging one, it was highest for radial rock pattern scenario. For the same rock soil cover, soil loss was highest for diamond rock pattern scenario and lowest for radial rock pattern scenario on both soil surface geometries. The runoff volume and soil loss variation among three different distribution patterns of constant rock cover could be attributed to different spacing between rock fragments. Poesen and Lavee (1991) observed that increasing the size of impervious mulch particles for the same cover percentage increased soil loss and runoff because the distance between mulch particles became larger, which reduced their ability to trap runoff. Bunte and Lavee (1994) also found that above 50% cover, larger rock fragments (cobbles) yielded more sediment losses by overland flow than smaller ones (pebbles).

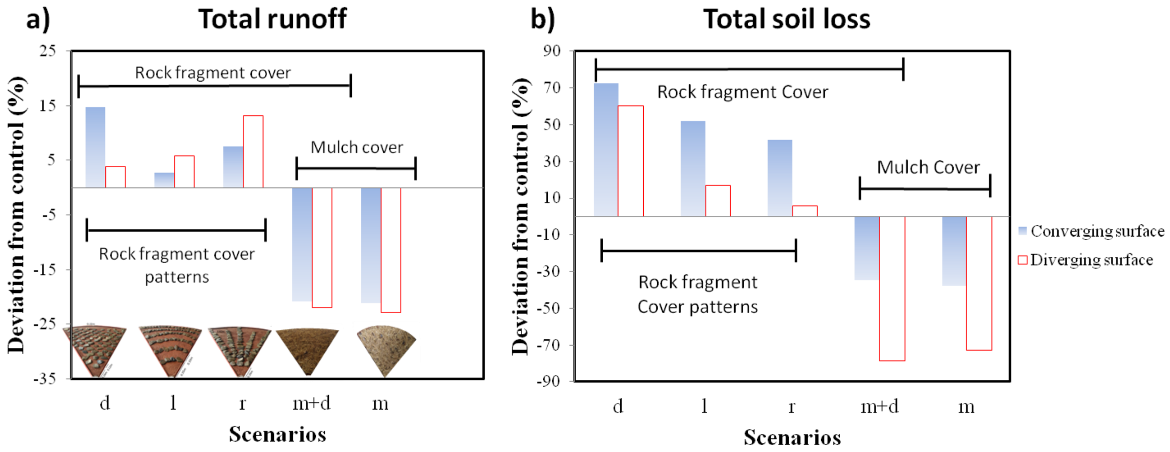

Fig. 3.7. Deviation in a) total runoff volume and b) total soil loss of all rock fragment cover and mulch cover scenarios with respect to control (bare soil) scenario.

In our study, rock fragment cover was constant but the spatial arrangements of the rock fragments, in different patterns, produced different distances between rock fragments in different regions of the flume's soil surface. In radial pattern, rock fragments in contact with each other sides made five alignments that were 0.47 m apart at the diverging end of flume. These alignments converge together along radial lines to form cluster at the converging end of flume. Oncoming runoff was concentrated around rock alignments, causing scour. Water movement on the front side of rock fragments within the rock alignments was minimum. On converging surface, cluster of rock fragments broke the concentrated flow into multi thread flow; thus, it acted as dispersion instrument to reduce the soil loss. While in diverging surface, rock fragments cluster only generated the reticular flow and protected the soil surface from infiltration. In this rock distribution pattern, front side of rock fragments in alignments and cluster was protected from scouring, thus, resulting in least soil loss on both converging and diverging surfaces. In lines rock pattern, rows were 0.33 m apart from each other.

Rock fragments sides were in contact with each other in each row, ensuring small spaces between rock fragments. Rainfall generated runoff was first concentrated to the front side of each rock fragment in a row. Then, the concentrated flow broke into many small threads by the small spaces between rock fragments. This effect was observed in each row on both soil surface geometries. Main scour occurred at the front side of each rock fragment with less detachment around rock fragments due to less available space. As the front side of rock fragments was unprotected from scouring, soil loss was higher in lines rock pattern than on radial rock pattern.

In the diamond rock cover pattern (Fig. 3.2b), rock fragments were laid on the soil surface to obtain an even (diamond-patterned) distribution. Not a single rock fragment was in contact with another one. Longitudinal distance between each rock fragment was approximately 0.12 m. In the cross section direction, the distance between rock fragments was ~0.22 m (this distance between rock fragments was markedly higher than for the line row and radial row patterns). For the diamond pattern, water flow was concentrated in few threads. All three sides of rock fragment (front, left and right) that contacted the oncoming runoff were unprotected from scouring due to more available space. Highest soil loss was observed for diamond cover rock pattern compared to the other two patterns on both converging and diverging surfaces. Thus, for constant percentage of surface rock fragment cover, rock distribution patterns that resulted in having rock fragments sides protected from the direct contact of oncoming runoff yielded less soil loss. However, our study was limited to a single rainfall intensity, slope gradient, initial moisture condition and rock fragment cover percentage. Future studies are required under different initial conditions to better understand the effect of spatial variation of constant rock fragment cover on soil loss and runoff.

3.6.2. Effect of organic mulch cover of soils with and without rock fragments on their surface on runoff and soil loss

Many laboratory studies that were conducted on planar soil surfaces (rectangular plane shape) under laboratory conditions without any surface rock fragment cover (e.g. Montenegro et al., 2013; Prats et al., 2017; Abrantes et al., 2018b) have observed the effectiveness of organic mulch to reduce runoff and soil loss compared to bare soil conditions. Our study found similar results on converging and diverging plane surfaces. We also found small differences in runoff volume and total soil loss between mulch cover scenarios (mulch over bare soil and mulch over soil with rock fragment cover) were observed (see Fig. 3.7). Organic mulch applied to bare soil reduced runoff volume the most compared to control scenario on both converging and diverging surfaces. Both mulch cover scenarios resulted in similar soil loss rates on converging surfaces. While on diverging soil surfaces, the organic mulch over rock fragment cover reduced soil loss by 28% more than the mulch over bare soil scenario. For mulch cover scenarios, runoff initiation time occurred later than for other scenarios, on both soil surface geometries, which indicates longer ponding time. In our study, organic mulch covered the whole soil surface, leaving very small surface areas available for direct raindrop impact. Organic mulch protected both soil surface geometries from splash erosion. Mulching reduced runoff by means of increase in the water storage capacity by the mulch itself, decreasing runoff velocity and increasing runoff ponding time, which increased infiltration. Due to the soil protection from raindrop impact and flow retardation promoted by mulch cover, soil loss was lower than for bare soil conditions. Presence of surface (flat) rock fragments below the organic mulch reduced infiltration into the soil area below rocks; thus slightly higher runoff was observed for this case than for mulch over bare soil, on both soil surface geometries. However, mulch over rock cover reduced more soil loss than mulch over bare soil on diverging surface; but accumulated soil loss was very small with high variability (e.g. as suggested by the coefficient of variation in Table 3.3), for both scenarios. Results suggest that mulching is an effective technique to mitigate soil erosion, otherwise aggravated by the presence of rock fragments over the soil surface.

3.6.3. Effect of soil surface geometry on runoff and soil loss

Overall, runoff volumes of all scenarios on converging surfaces were up to 1.2 times higher than their corresponding values on diverging surfaces. However, soil loss of all scenarios was markedly higher (10 to 30 times) on converging surfaces than that on diverging surfaces (see Table 3.3 and Fig. 3.8).

For converging and diverging planar surfaces, stream power increases along the slope length and, consequently, it is maximum at the outlet. During the experimental runs, unit stream power for all scenarios were around 20 up to 150 times higher on converging surfaces than on diverging surfaces. The higher unit stream power on converging surface generated more soil erosion (Fig. 3.9). For this case, flow depth tends to increase downstream as the available width decreases. Note that the presence of surface rock fragments further decreased the flow width. By contrast, on diverging surface, unit stream power does not increase that much in flow direction as flow width increases. Consequently, soil loss is far less on diverging surface than on converging surface. Furthermore, flow lines might be locally distorted by the presence of rock fragments, which further alters the flow dynamics. Nevertheless, soil surface geometry seams to affect more the hydraulics of overland flow than the patterns of surface rock fragments.

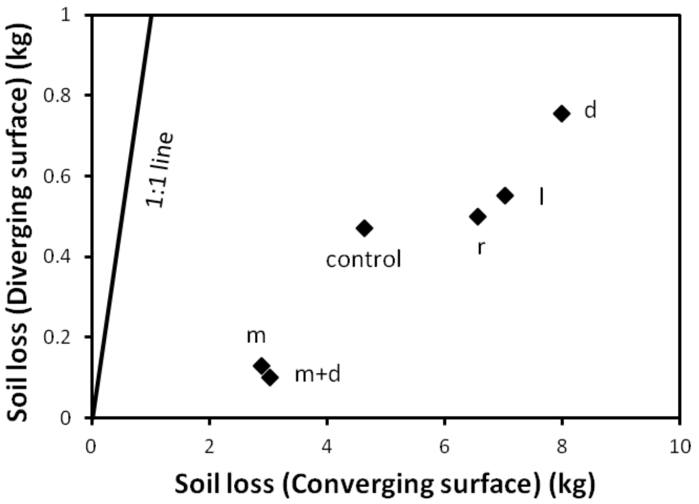

Fig. 3.8. Relation of total soil loss of all surface cover scenarios between converging and diverging plane surfaces. Note the factor of 10 between the vertical and horizontal scales.

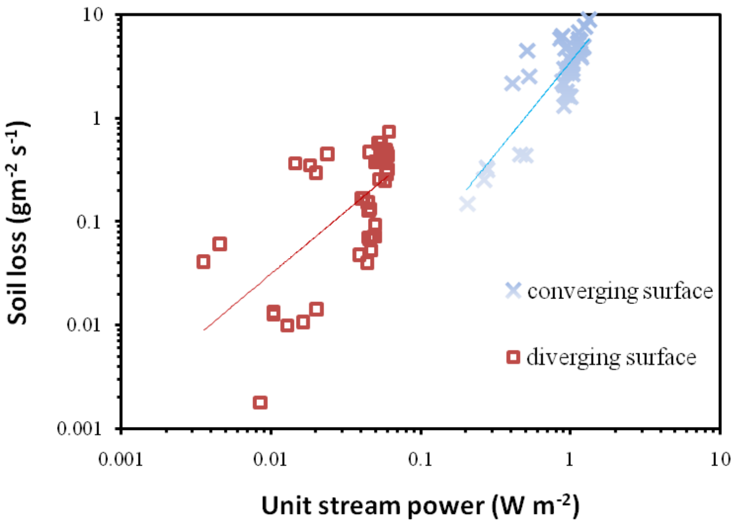

Fig. 3.9. Relation of soil loss measured for all scenarios with unit stream power (at downstream end) for both converging and diverging plane surfaces (log-log scales).

The more intense formation of rills on converging surface, as shown in Fig. 3.10, could be attributed to high stream power, in comparison to diverging surfaces. Also, big rills were formed due to the boundary conditions (flume's wall). However, averaged over all scenarios, soil loss from those rills amounted to only 3 - 15.5% of total soil loss (Fig. 3.11). Those relatively low values suggest that interrill erosion, small rills and local scour around rock fragments were the main contributors to soil erosion on the converging surface rather than the effect of the soil flume border. In case of diverging surface, no big rills were formed along the flume border but there was scour around rock fragments

(Fig. 3.10g,h), again indicating that interrill erosion and small rills around rock fragments were mainly responsible for soil erosion.

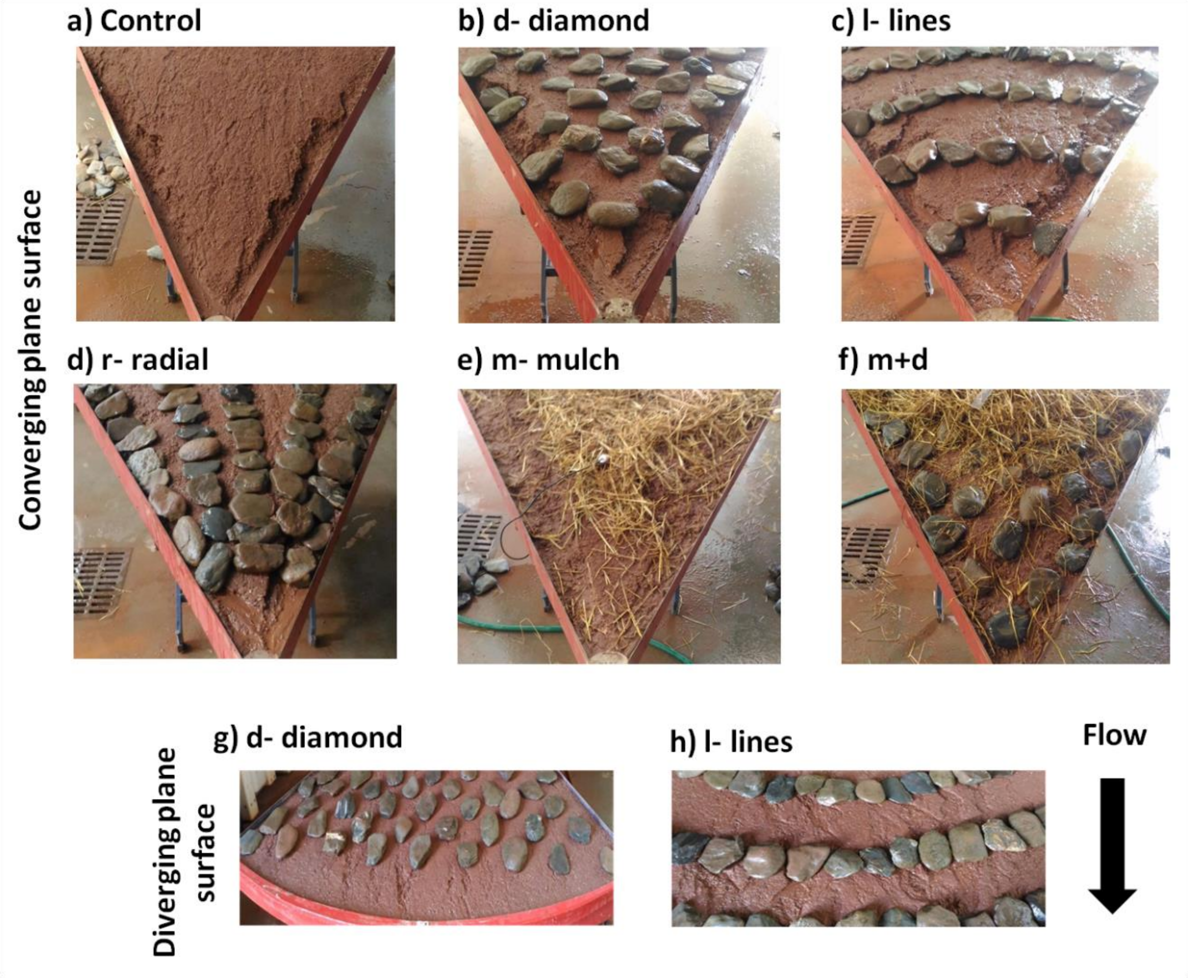

Fig. 3.10. Big rills along the border (flume's wall) and small rills around rock fragments and on the soil surface for scenarios a) control, b) d, c) l, d) r, e) m and f) m+d, on converging plane surface. Small rills around rock fragments and on the soil surface for scenarios g) d and h) l, on diverging plane surface.

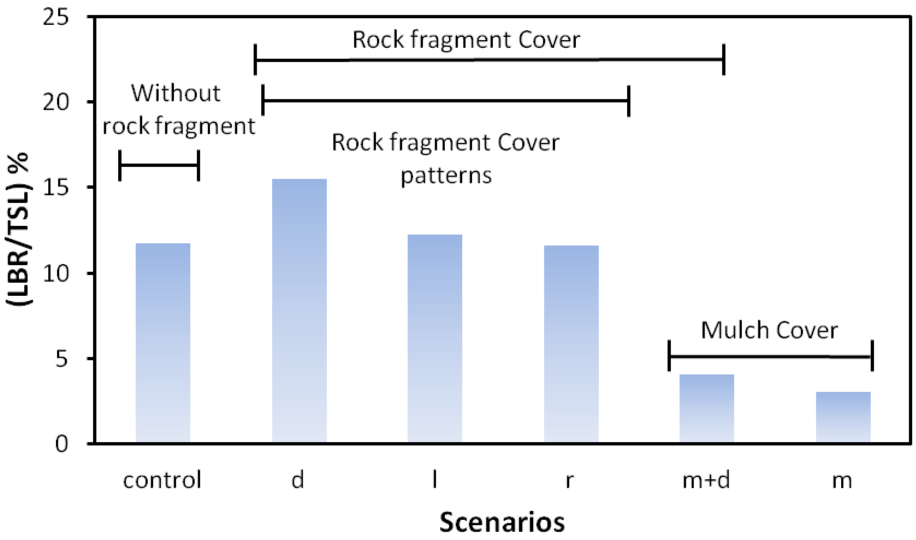

Fig. 3.11. Contribution of soil loss from large border rills (LBR) in total soil loss (TSL) for the soil surface scenarios, on converging plane surface: control (bare soil), three rock fragment cover patterns (d, l and r) and mulch cover (m and m+d).

3.7. Conclusions

In this study, laboratory experiments under simulated rainfall were conducted to study the variations in runoff and soil erosion response to three different distribution patterns of a rock fragment cover and an organic mulch cover (without and combined with rock fragment cover) on two soil surface geometries (converging plane and diverging plane). The rock fragments were resting on the top of the soil surface. The following main conclusions could be drawn:

- For the same rainfall input, runoff volumes for all soil surface conditions' scenarios on converging surfaces were slightly higher (up to 1.2 times) than their corresponding values on diverging surfaces. However, total soil loss for all scenarios on converging surfaces was 10 to 30 times higher than on diverging surfaces.

- Overall, for a given surface geometry, all patterns of rock fragment cover increased runoff and soil loss when compared to the control (bare soil) scenario.

- Among all three patterns of rock fragment cover, diamond pattern rock fragment cover had the highest total soil loss while rock fragments arranged in a radial pattern had the lowest, on both converging and diverging surfaces, for the same percentage cover.

- Mulching reduced runoff and soil loss compared to the control (bare soil) scenario on both surfaces' geometries.

- Unit stream power at the downstream end of the flume, for all scenarios, was around 20 to 150 times higher on converging surfaces than that on diverging surfaces. This explains the significant difference in observed soil loss.
- In the presence of surface rock fragments, which promote runoff and soil erosion, organic mulch can be an effective technique for soil conservation, especially in converging surfaces.

The results suggest that soil surface geometry was a key factor influencing the hydraulics of overland flow, being a much more important factor than the patterns of surface rock fragment cover.

Future studies should evaluate further the runoff and soil loss response of soil surfaces covered with rock fragments and organic mulches; for example, investigation could be done on: (i) different curvatures (convex and concave) of different soil surface shapes (converging, linear and diverging) and for different types of soil in order to fully understand the complex interactions involved; (ii) the effect of the position of rock fragments embedded on the surface soil layers, in these complex geometries; (iii) the flow hydraulics in presence of surface rock fragments and mulch.

4. The role of stony soils in hillslope and catchment runoff formation [2]

4.1. Abstract

The role of stony soils in runoff response of mountain catchments is rarely studied. We have compared simulated response of stony soils with measured catchment runoff for events caused by rains of small and high intensities in the mountain catchment of the Jalovecký Creek, Slovakia. The soil water response was simulated for three sites with stoniness 10-65 % using the Hydrus-2D single porosity model. Soil hydraulic parameters employed in the modelling, i. e. the saturated hydraulic conductivity and parameters of the soil water retention curves, were obtained by two approaches, namely by the Representative Elementary Volume approach (REVa) and by the Inverse Modelling with Hydrus-1D model (IMa). The soil water outflow hydrographs simulated by Hydrus-2D were compared to catchment runoff hydrographs by analysing their skewness and peak times. Measured catchment runoff hydrographs were similar to simulated soil water outflow hydrographs for about a half of rainfall events. Interestingly, most of them were caused by rainfalls with small intensity (below 2.5 mm/10 min). The REV approach to derive soil hydraulic parameters for soil water outflow modelling provided more realistic shapes of soil water outflow hydrographs and peak times than the IMa approach.

4.2. Introduction

Soils play an important role in catchment runoff formation. The response of catchment runoff to precipitation is highly non-linear due to heterogeneity in inputs and catchment characteristics, threshold behaviour depending on catchment wetness and storage state, varying relative contributions of different landscape units, etc. An excellent state of the art review of the processes and controlling factors affecting runoff formation at hillslopes was recently given by Bachmair and Weiler (2011). Preferential flow in the soils (Beven and German, 1982), the instability-driven flow (Tesař et al., 2001) or fill and spill mechanism (Tromp-Van Meerveld and McDonnell, 2006) are commonly used to explain rapid formation of the subsurface flow

---

[2] **Mujtaba, B.,** Hlaváčiková, H., Danko, M., de Lima, J.L.M.P., Holko, L., 2020. The role of stony soils in hillslope and catchment runoff formation. J. Hydrol. Hydromechanics 68 (2), 144–154. https://doi.org/10.2478/johh-2020-0012

that eventually contributes to catchment stormflow. Soil stoniness can have similar effect (Hlaváčiková et al., 2015, 2016) as the retention capacity of stony soils is reduced. This phenomenon is still not well studied, and it is neglected in runoff formation theories.

Many authors (e.g. Li and Sivapalan, 2011; Botter and Rinaldo, 2003) observed that hillslope processes, mainly the lateral subsurface flow tend to make catchment runoff hydrograph positively skewed. Hillslope lateral subsurface flow is dependent on soil properties such as infiltration capacity, heterogeneity of hydraulic conductivity, soil water retention, thickness of unsaturated zone and preferential pathways.

Stony soils are commonly found in hilly and forested regions of the world. Stoniness, defined as the relative volume of rock fragments, is an important soil property. It can strongly influence water infiltration, movement, retention characteristics and runoff formation (e.g. Al-Qinna et al., 2014; Chen et al., 2012; Hlaváčiková et al., 2015). Correct estimation of the soil hydraulic properties (i.e. hydraulic conductivity and van Genuchten soil water retention functions) is essential to evaluate the water flow (hydrological response) in stony soils. Water flow modelling in a stony soil profile is difficult due to the heterogeneity of rock fragments distribution and quantity. It requires determination of the retention characteristics of fine soil fraction, saturated hydraulic conductivity and stoniness in soil layers. For this, a large representative elementary volume (REV) of soil sample is needed to characterize the bulk characteristics of the stony soil profile (e.g. Hlaváčiková et al., 2015, 2018). Buchter et al. (1994) recommended that the dry mass of a stony soil sample should be at least 100 times the mass of the largest particle. However, there is no rule for how large the REV of a stony soil should be for measuring its hydraulic characteristics. After obtaining the stoniness from REV, the soil water retention curves of the fine soil fraction are corrected to adequately represent the hydraulic characteristics of the studied stony soil profile (e.g. Bouwer and Rice, 1984; Ma and Shao, 2008; Coppola et al., 2013).

An alternative approach to REV, the inverse modelling utilizing measured soil moisture data has been used for the estimation of soil hydraulic parameters (e.g. Šimůnek and van Genuchten, 1996; Šimůnek et al., 1998; Wegehenkel et al., 2017). The inverse modelling uses optimization techniques for the estimation of soil hydraulic parameters from transient flow transport data (Šimůnek et al., 2013). The disadvantage of this approach is that derived soil hydraulic parameters can be applied only to the sample volume around the soil moisture sensors that may be very small (200 cm^3) compared to the REV (1 m^3).

In our knowledge, not a single study addressed the impact of soil hydraulic parameters estimated by both inverse modelling and REV on the lateral subsurface flow simulations in stony soils. The objective of our work was to compare the response of the outflow from stony soils in a small mountain catchment to rainfall events with different intensity to catchment runoff response. To fulfil the objective, the work was divided into two parts. First, soil hydraulic parameters needed for the subsurface water flow modelling for three study sites with moderate to high stoniness (10-65%) were derived by the REV (REVa) and inverse modelling (IMa) approaches. Then, comparison of lateral subsurface flow hydrographs (hereafter also soil water outflow) and catchment runoff was done by analysing the skewness and peak time of the hydrographs.

4.3. Study site

The study is carried out in the mountain catchment of the Jalovecký Creek (the Western Tatra Mountains, Slovakia), shown in Fig. 4.1. Catchment area is 22.2 km^2, its mean slope angle is 30° and the altitude ranges from 800 to 2178 m a.s.l. (mean 1500 a.s.l.). The bedrock is dominantly formed by crystalline and metamorphic rocks. Soils are represented by shallow Cambisol, Pozdol, Lithosol, and Leptosol (the soil depth is about0.7–1 m). Soil stoniness is high and varies from 10–65% or more. Forest (mostly spruce), dwarf pine and alpine meadows, including bare rocks on the steepest slopes, cover 44%, 31%, and 25% of catchment area, respectively. Most of the forest is over 100 years old. Mean annual precipitation is about 1500 mm and mean air temperature is 3°C. Additional catchment characteristics can be found e.g. in Holko et al. (2010); the detailed information about the catchment hydrological cycle over the three decades of its monitoring is presented in Holko et al (2020 a,b) .

Simulation of water outflow from the mountain soils was carried out for three sites located at elevations above 1000 m a.s.l. Two of them are in the forest, one is in the open area covered by grass. The main attributes of the sites are:

Site 1: Červenec – open area, 1500 m a.s.l., a flat terrain with slope angle 2.86°, slightly to moderately stony soil classified as a Leptosol with a sandy loam texture is typical for the site. The site is covered by grass and low density vegetation.

Site 2: Červenec – forest, 1450 m a.s.l., a moderately steep terrain with slope angle 14°.

Site 3: Pod Lyscom, 1040 m a.s.l., a steep terrain with slope angle 22°.

Moderate to high soil stoniness is typical for sites 2 and 3. The soil type is classified as Cambisol and has a sandy loam texture. A 130-year old Norway spruce forest (*Piceaabies*) and a low understorey vegetation of *Vacciniummyrtillus*L. grow at the sites.

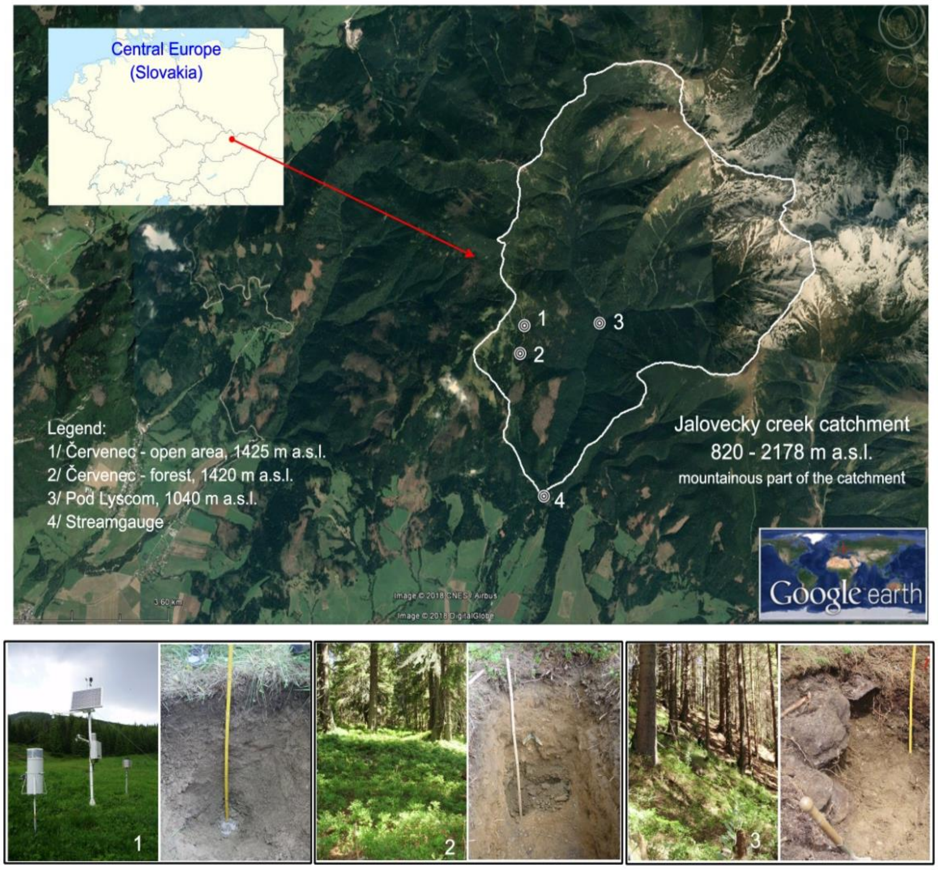

Fig. 4.1. The Jalovecký Creek catchment, location of the sites for which the soil water outflow was simulated (1, 2 and 3), vegetation and soil profiles at the sites; catchment outlet where catchment runoff was measured is indicated by number 4.

4.4. Data

Rainfall, discharge and soil moisture data of the warm seasons (June to September) measured in years 2013-2016 were used in this study. Rainfall and soil moisture data were measured every 10 minutes at all three sites. Hourly discharge data measured at catchment outlet (820 m a.s.l.) were obtained from the 10-min interval pressure transducer water level measurements and the discharge rating curve.

Rainfall data provided the meteorological inputs for the simulation of the soil water outflow. Fifteen rainfall events separated according to rainfall intensity were used (Table 4.1). The small intensity rains had maximum intensity below 2.5 mm/10 min. The large intensity rains had maximum intensity above 3.5 mm/10 min. This division was based on the unpublished results of the analysis of soil moisture response to rainfall on the study sites. Catchment runoff hydrographs during the rainfall events were used for the comparison of soil and catchment responses. The soil moisture measurements helped to obtain the hydraulic parameters of the soils (i.e. the saturated hydraulic conductivity and parameters of the soil water retention curves) used in the lateral subsurface flow simulation (by inverse modelling). Physical characteristics of the soils were measured in the soil pits of 1 m^2 cross section dug to depths 0.70-0.95 m at each site (Hlaváčiková et al., 2015).

Table 4.1. Characteristics of the rainfall events and periods used for the lateral subsurface flow simulations at the three study sites; API is total precipitation over the last 10 days, A-I are events with small rainfall intensity, AI-FI are events with large rainfall intensity.

Rainfall event	Study site	Simulation period	Rainfall amount (mm)	10-min maximum (mm)	API (mm)
A	Červenec - open area	22.9.- 16.10.2013	58.4	1.5	116
	Červenec - forest		72.8	1.4	75
	Pod Lyscom		39.8	1.4	120
B	Červenec - open area	24.6. - 29.6.2014	19.4	1.6	13
	Červenec - forest		12.8	1.0	8
	Pod Lyscom		14.2	1.4	2
C	Červenec - open area	11.7. - 14.7. 2014	24.4	1.0	103
	Červenec - forest	11.7. - 18.7.2014	18.4	0.8	66
	Pod Lyscom	11.7. - 18.7.2014	22.6	1.2	75
D	Červenec - open area	25.9. - 1.10.2014	38.2	1.5	44
	Červenec - forest		23.6	1.0	25
	Pod Lyscom		27.8	1.0	29
E	Červenec - open area	2.9. - 9.9.2013	17.3	1.6	31
	Červenec - forest	2.9. - 11.9.2013	25.4	1.4	14
	Pod Lyscom	2.9. - 11.9.2013	23.2	1.4	14
F	Červenec - open area	23.8. - 9.9.2014	39.2	1.7	50
	Červenec - forest		31.2	2.8	24
	Pod Lyscom		18.2	1.0	20
G	Červenec - open area	8.8. - 14.8.2016	30.4	2.1	14
	Červenec - forest		20.0	1.6	30
	Pod Lyscom		27.2	1.6	40
H	Červenec - open area	5.8. - 10.8.2016	13.1	1.7	62

	Pod Lyscom	5.8. - 10.8.2016	12.6	1.6	56
I	Červenec - open area	20.8. - 4.9.2016	21.2	2.5	25
	Pod Lyscom*	20.8.- 5.9.2016	24.6	5.6	22
AI	Červenec - open area	8.8. - 28.8.2013	28.1	3.8	10
	Červenec - forest	9.8. - 28.8.2013	15.6	3.8	7
	Pod Lyscom	9.8. - 28.8.2013	11.6	3.4	6
BI	Červenec - open area	1.7. - 8.7.2014	51.3	5.7	90
	Červenec - forest		39.6	3.6	55
	Pod Lyscom		36	3.4	62
CI	Červenec - open area	20.7. - 28.7.2014	40.4	6.3	33
	Červenec - forest	20.7. - 31.7.2014	38.8	6.0	22
	Pod Lyscom	20.7. - 31.7.2014	28.0	2.2	27
DI	Červenec - open area	10.8.2014-13.8.2014	50.9	12.0	19
	Červenec - forest		31.4	11.2	17
	Pod Lyscom		35.0	9.4	16
EI	Červenec - open area	3.8.2015-14.8.2015	89.4	12.0	58
	Červenec - forest		71.6	21.2	46
	Pod Lyscom		82.6	19.3	35
FI	Červenec - open area	13.8.2016-21.8.2016	25.3	6.6	43
	Červenec - forest		17.4	4.8	30
	Pod Lyscom		22.2	6.0	40

Pod Lyscom * - event I at the site is classified as large intensity rainfall

4.5. Methodology

4.5.1. Lateral subsurface flow simulation

Lateral subsurface flow hydrographs were simulated by the well-known finite element model HYDRUS 2D (Šimůnek et al., 2008, 2013) as the outflow from the soil through gradient boundary. The 20 m long hillslope segment with 1 m soil profile depth (Fig. 4.2) and different slope angles corresponding to the slope angles at the three study sites (2.86°, 14°, and 22° for sites 1, 2, and 3, respectively) were schematized for the simulations. Soil layers in the model corresponded to the layers found in the soil pits. The following boundary conditions were used in the simulations (Fig. 4.2):

- the upper boundary (surface) was set as atmospheric boundary condition.
- the lower boundary (bottom) and upper vertical boundary (left hand side) were set as no flux conditions. No flux condition at the lower boundary was given because the hydraulic conductivity of the bedrock was much smaller than that of the above soil and water table was not present in the soil profile.

- the lower vertical boundary (right hand side) was set as gradient boundary condition.

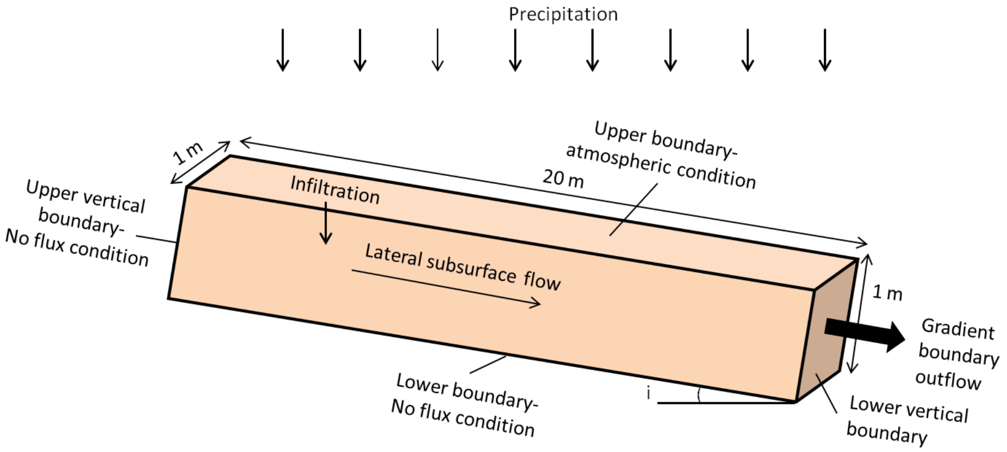

Fig. 4.2. Schematic sketch of the hillslope section used in simulation of the soil water outflow (lateral subsurface outflow). Boundary conditions are also presented. Gradient boundary outflow is the lateral subsurface outflow. *i* denotes the slope angle which is 2.86° for site 1 (Červenec – open area), 14° for site 2 (Červenec – forest) and 22° for site 3 (Pod Lyscom), respectively.

The computation time varied from 40 to 60 minutes for each simulated rainfall event. In total, 86 simulations of the soil water outflow were conducted.

The soil hydraulic parameters required by HYDRUS 2D (i.e. the saturated hydraulic conductivity K_s and parameters of the soil water retention curve θ_s, θ_r, α, n) were obtained by two approaches – the representative elementary volume (REV) and inverse modelling (IM) as described below. The two approaches were used to obtain the hydraulic parameters for the soil depth 0-50 cm. Hydraulic parameters the soil depth 50-100 cm were obtained only from the REV approach.

The REV approach was based on field measurements in soil pits of 1 m^2 cross section dug to depths 0.70-0.95 m at each site (Hlaváčiková et al., 2015). Volumes of stones and boulders were measured directly in the field. Soil stoniness estimated for the soil pits of the REV dimensions is shown in Fig. 4.3. Additionally, the disturbed soil samples with volume of 2-3 litres were collected for each characteristic soil layer for the laboratory evaluation of the fine soil fraction and the volume of the gravel part of the stoniness.

Undisturbed and disturbed samples of fine soil with volume 100 cm^3were collected for each characteristic soil layer at each site to determine the saturated hydraulic conductivity and water retention measurements. The saturated hydraulic conductivity of the fine soil was estimated in the laboratory by the variable hydraulic head method. A small number of field measurements of the saturated hydraulic conductivity was carried out with the single ring infiltrometer as well (Hlaváčiková et al., 2015, 2018). Drying branches of the soil water retention curves (SWRC) of the fine soil were measured by the pressure plate extractor (Dane and Hopmans, 2002) for pressure heads between –50 and –3000 cm. Drying branches of the soil water retention curves of top soil layer (organic horizon) were measured by the sand tank for pressure heads between –2 and –100 cm, smaller pressure heads were measured by the pressure plate extractor. Measured soil water retention curves were fitted by the analytical model of van Genuchten (1980) and their parameters θ_s (the saturated water content) and θ_r (the residual water content) were corrected for the stoniness using the Bouwer and Rice equation (1984). The stoniness-corrected soil water retentions curves and measured saturated hydraulic conductivity (an average of the laboratory and field measurements) obtained for different soil layers at all three study sites provided the soil hydophysical parameters needed in the lateral subsurface flow modelling. Stoniness used in the REV approach for the soil water retention correction was determined from the soil pits stoniness measurements shown in Fig. 4.3.

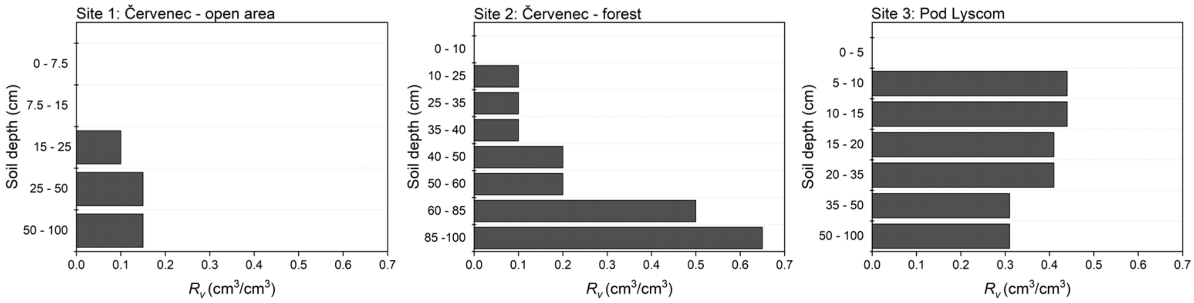

Fig. 4.3. Stoniness R_v (cm^3cm^{-3}) in different soil layers on site 1, 2 and 3 measured in the representative elementary volume (REV) of about 1 m^3; modified from Hlaváčiková et al. (2015).

The IM approach for determination of soil hydraulic parameters was based on the single porosity HYDRUS 1D modelling calibrated against measured soil moisture using the optimization technique available in the Hydrus 1D package. Model parameters were set according to fine soil water retention and the stoniness measurements. Time series of measured soil water contents at three depths (5, 10, 20 cm) at site 1 and two depths (10, 40 cm) at sites 2 and 3 were used in the inverse modelling. Simulated soil profile of all three sites had depth of 50 cm. Soil hydrophysical parameters were determined by the IMa only for the soil depths 0-50 cm because the soil moisture data were not measured at greater depths due to large soil stoniness.

The initial soil conditions for water flow modelling were set for each rainfall event separately according to antecedent soil wetness represented by pressure heads. For this purpose, the soil water potential was estimated from the known soil water retention curves and by taking in account the antecedent precipitation (API). The API was calculated as the sum of 10-day rainfall before the rainfall event. Initial conditions set in the form of pressure heads were chosen because the pressure head can better describe the status of water at the beginning of the simulation. The inverse modelling was done as in Wegehenkel et al. (2017). First, the parameters n and θ_s were calibrated, then K_s and θ_r were obtained, and finally parameter α was calibrated.

4.5.2. Hydrographs comparison

The subsurface lateral flow hydrographs simulated by HYDRUS 2D (with soil hydrophysical parameters from both REVa and IMa) were compared to measured catchment runoff hydrographs. The comparison was based on hydrograph geometry (skewness) and peak times. Skewness as an important characteristic of hydrograph geometry was quantified by the volume before peak (VBP) values (Collischonn et al., 2017). The VBP is the ratio of the flow volume before the peak to total flow volume during an event. Its value ranges between 0 and 1. If VBP is equal to 0.5, the hydrograph is symmetrical. VBP smaller than 0.5 characterizes the positively skewed hydrographs while the negatively skewed hydrograph has the VBP greater than 0.5. Flow volume before the peak was calculated from the discharge data between the rainfall beginning and the hydrograph peak. Total flow volume was calculated from the initiation time of the rainfall until the time when discharge dropped to the value measured before the rainfall. The peak time difference between catchment runoff and lateral subsurface flow hydrographs for every rainfall event at each site was analysed as well. The VBP and peak time difference were used to quantify the geometric similarities of subsurface and catchment runoff hydrographs.

4.6. Results

4.6.1. Influence of stoniness on soil hydraulic parameters estimated by the REV and inverse modelling approaches

Soil hydraulic parameters estimated by REVa and IMa which were thereafter used in the soil water outflow simulation are given in Tables 4.2 and 4.3. Two out of five parameters, namely the saturated hydraulic conductivity (K_s) and the volumetric saturated soil moisture content (θ_s) were found to be the most sensitive in inverse modelling. Figs. 4.4 and 4.5 show the K_s and θ_s values estimated by REVa and IMa at all three sites for different soil depths.

Table 4.2. Soil hydraulic parameters estimated by the REV approach at various soil depths on the three study sites; θ_s is the saturated water content, θ_r is residual water content, α and n are the van Genuchten´s parameters, K_s is the saturated hydraulic conductivity and R_v is the relative volume of rock fragments.

Soil depth	θ_r(cm^3 cm^{-3})	θ_s (cm^{3}cm^{-3})	α (cm^{-1})	n (-)	K_s(cm min^{-1})	R_v(cm^{3}cm^{-3})
Site 1: Červenec - open area						
0 - 7.5 cm	0.1	0.63	0.10	1.27	2.42	0.00
7.5-15 cm	0.05	0.51	0.43	1.13	1.00	0.00
15-25 cm	0.05	0.45	0.43	1.13	0.25	0.10
25 - 50 cm	0.04	0.43	0.41	1.11	0.25	0.15
50 - 100 cm	0.04	0.41	0.40	1.10	0.25	0.15
Site 2: Červenec– forest						
0-10 cm	0.05	0.64	0.48	1.22	18.33	0.00
10 - 25 cm	0.05	0.58	0.05	1.24	3.50	0.10
25 - 35 cm	0.05	0.57	0.07	1.25	1.00	0.10
35 - 40 cm	0.05	0.57	0.07	1.25	0.67	0.10
40 - 50 cm	0.04	0.50	0.07	1.25	0.67	0.20
50 - 60 cm	0.04	0.50	0.07	1.25	0.67	0.20
60-85 cm	0.03	0.31	0.07	1.25	0.33	0.50
85-100 cm	0.02	0.22	0.07	1.25	0.33	0.65
Site 3: Pod Lyscom						
0 - 5 cm	0.05	0.63	0.56	1.21	46.67	0.00
5 - 10 cm	0.03	0.36	0.42	1.24	10.00	0.44
10 - 15 cm	0.03	0.41	0.13	1.27	5.67	0.44
15 - 20 cm	0.03	0.49	0.12	1.22	2.67	0.41
20 - 35 cm	0.03	0.49	0.12	1.22	2.42	0.41
35 - 50 cm	0.03	0.52	0.06	1.25	0.83	0.31
50 - 100 cm	0.03	0.52	0.06	1.25	0.33	0.31

Table 4.3. The Mean values of soil hydraulic parameters estimated by the IM approach; the mean values were calculated from the results of simulations for all 15 rainfall events; θ_s is the saturated water content, θ_r is the residual water content, α and n are the van Genuchten´s parameters, K_s is the saturated hydraulic conductivity and R_v is the relative volume of rock fragments.

Soil depth	θ_r(cm^3 cm^{-3})	θ_s (cm^{3}cm^{-3})	α (cm^{-1})	n (-)	K_s(cm min^{-1})	R_v(cm^{3}cm^{-3})
Site 1: Červenec - open area						
0 - 7.5 cm	0.10	0.59	0.11	1.25	1.61	-
7.5-15 cm	0.11	0.54	0.41	1.12	0.90	-
15-25 cm	0.02	0.42	0.46	1.14	0.42	0.10
25 - 50 cm	0.05	0.47	0.42	1.10	1.00	0.15
*50 - 100 cm	0.04	0.41	0.4	1.1	0.25	0.15
Site 2: Červenec– forest						
0-10 cm	0.12	0.61	0.42	1.26	11.37	-
10 - 25 cm	0.07	0.54	0.05	1.24	1.99	0.10
25 - 35 cm	0.14	0.57	0.06	1.25	2.15	0.10
35 - 40 cm	0.14	0.67	0.06	1.24	2.59	0.10
40 - 50 cm	0.08	0.61	0.07	1.22	1.97	0.20
*50 - 60 cm	0.04	0.50	0.07	1.25	0.67	0.20
*60-85 cm	0.03	0.31	0.07	1.25	0.33	0.50
*85-100 cm	0.02	0.22	0.07	1.25	0.33	0.65
Site 3: Pod Lyscom						
0 - 5 cm	0.12	0.68	0.31	1.23	22.22	-
5 - 10 cm	0.11	0.68	0.41	1.23	11.41	-
10 - 15 cm	0.05	0.61	0.12	1.26	5.33	0.20
15 - 20 cm	0.12	0.54	0.10	1.22	3.76	0.20
20 - 35 cm	0.09	0.83	0.10	1.21	4.01	0.20
35 - 50 cm	0.09	0.70	0.06	1.20	2.21	0.20
*50 - 100 cm	0.03	0.52	0.06	1.25	0.33	0.31

*Parameters for the soil depth of 50-100 cm were the same for the REV and the IM approaches and were derived by the REV approach.

The top soil layers (organic horizons) at all three sites (0-15 cm at Site 1, 0-10 cm at Site 2 and 0-5 cm at Site 3) contained no stones (Fig. 4.4). The highest K_s values were obtained for these layers by both REVa and IMa. The K_s values obtained by both IMa and REVa decreased in the presence of rock fragments at each site for both small and large intensity rainfalls. The largest K_s value difference obtained by inverse modelling for small and large intensity rainfalls was found in the soil depth of 0-7.5 cm at site 1 and 0-10 cm at site 2. Two and four times greater K_s values were obtained for large intensity rainfall at both sites and showed faster water dynamics during large intensity rainfalls. Apart from that, the K_s values obtained by IMa for large rainfalls were 0.7-1.3 times than those for small rainfalls for the remaining corresponding soil layers at all sites.

a) Small intensity rainfalls

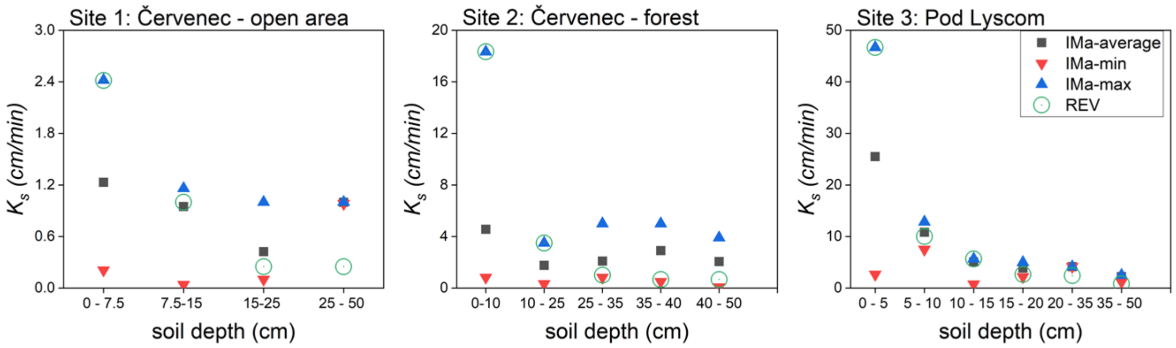

b) Large intensity rainfalls

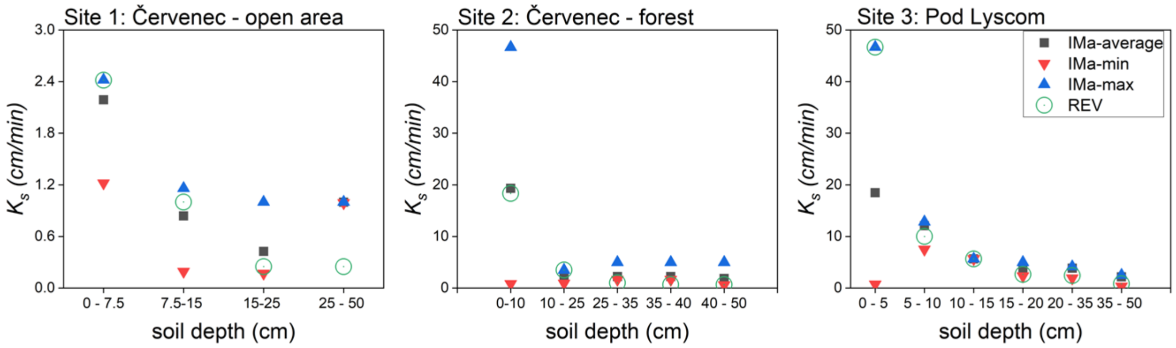

R_v - - 0.10 0.15 **R_v - 0.10 0.10 0.10 0.20** **R_v - - 0.20 0.20 0.20 0.20**

$^*R_v$ - 0.44 0.44 0.41 0.41 0.31

Fig. 4.4. Saturated hydraulic conductivity K_s estimated by the REV and IM approaches at various soil depths with different stoniness R_v; minimum and maximum K_s values estimated by the IMa are also presented; the asterisk denotes different stoniness at site 3 for REVa.

Soil retention capacity decreased with the increase of stoniness for the REVa at all three sites (Fig. 4.5). Compared to the top soil, 32%, 15% and 40% reduction in θ_s was observed, on average, at sites 1, 2 and 3, respectively. For the IMa, the retention capacity on site 1was the highest in the top soil (zero stoniness) for small and large rainfalls. For both small and large rainfalls, the θ_s value was the highest at lower soil layers on site 2 (35-40 cm depth, R_v0.1) and site 3 (20-35 cm depth, R_v 0.2). The greatest differences in the retention capacity of soils profiles between the REV and IM approaches were found on site 3. These differences correspond to different stoniness related to the particular approach.

a) Small intensity rainfalls

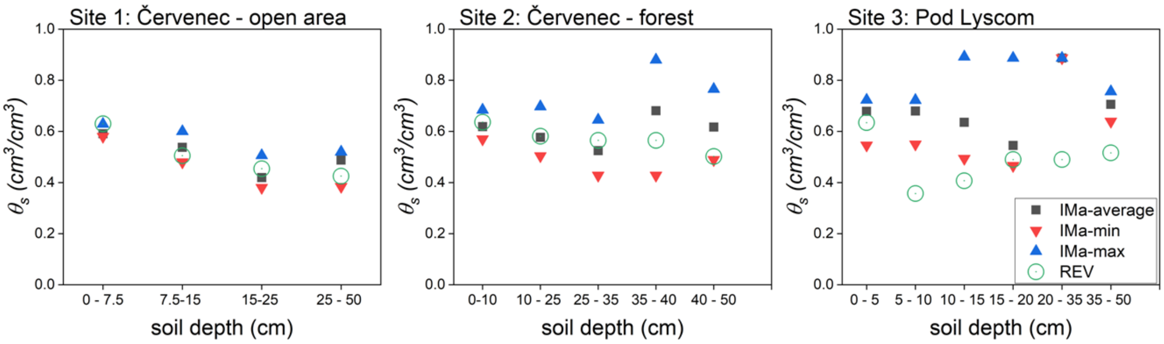

b) Large intensity rainfalls

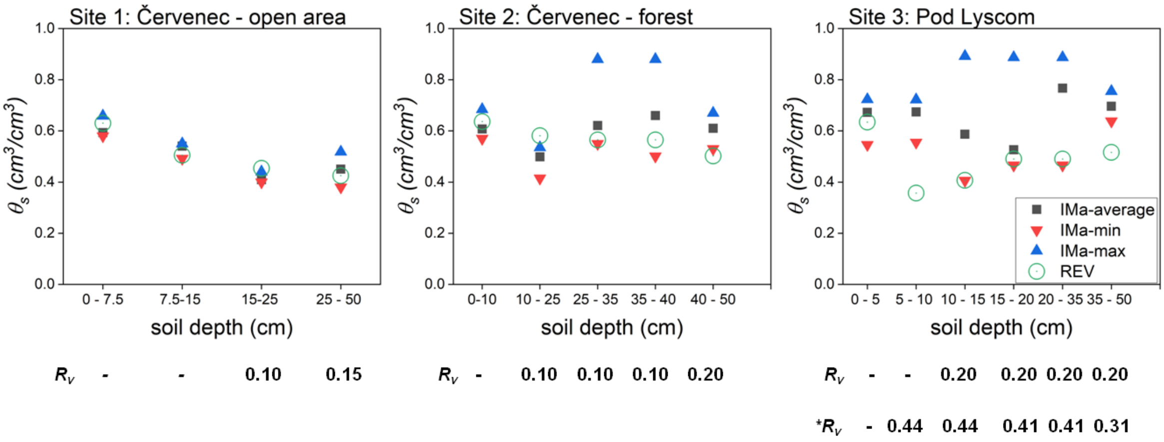

Fig. 4.5. Saturated moisture content θ_s estimated by the REV and IM approaches at various soil depths with different stoniness R_v of site 1, 2 and 3; minimum and maximum θ_s values estimated by the IMa are also presented; the asterisk denotes different stoniness at site 3 for REV.

4.6.2. Comparison of the lateral subsurface flow and catchment runoff hydrographs

Soil moisture of the top soil layer at all three sites significantly increased at the initiation of rainfall and started to decrease slowly when the rain finished (Fig. 4.6).

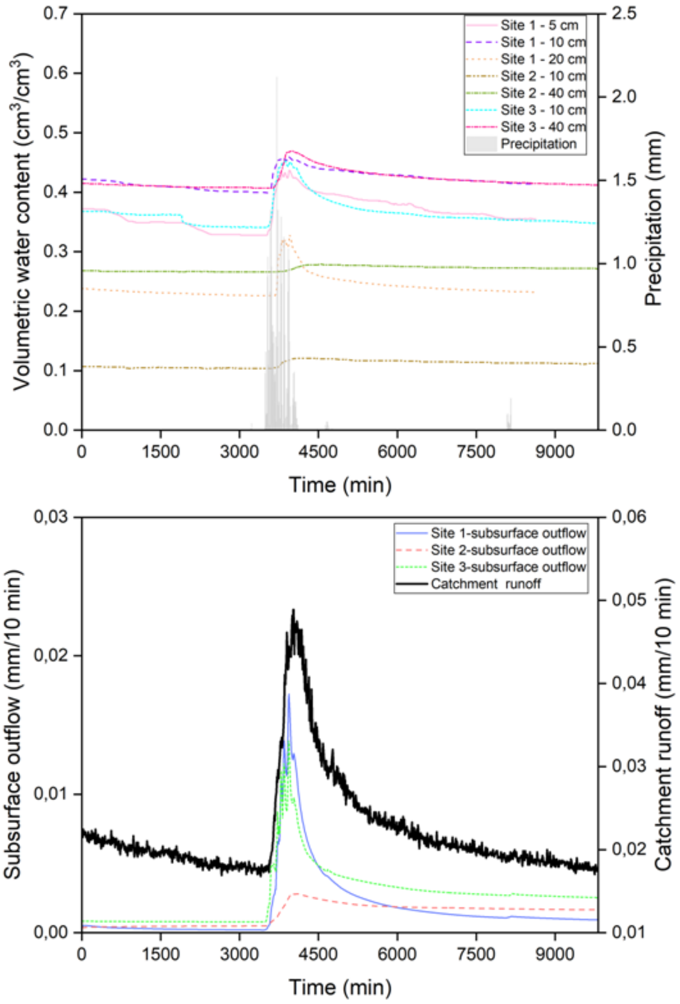

Fig. 4.6. Comparison of simulated lateral subsurface flow based on the REVa (the bottom panel) and catchment runoff for the small intensity rainfall event G; the soil moisture and rainfall measurements are presented in the top panel.

Patterns of the lateral subsurface flow and catchment runoff hydrographs were similar. An example of the lateral subsurface flow and catchment runoff responses for the small and high intensity rainfalls is shown in Fig. 4.7. The most pronounced lateral subsurface flow response was simulated for site 1 which is located in the open area. The response at forested sites 2 and 3 was also dynamic, but only for the soil hydraulic parameters estimated by the REV approach. Hydraulic parameters obtained from IMa typically resulted in smaller dynamics of the simulated lateral subsurface flow response on sites 2 and 3.

a) Small intensity rainfall event D

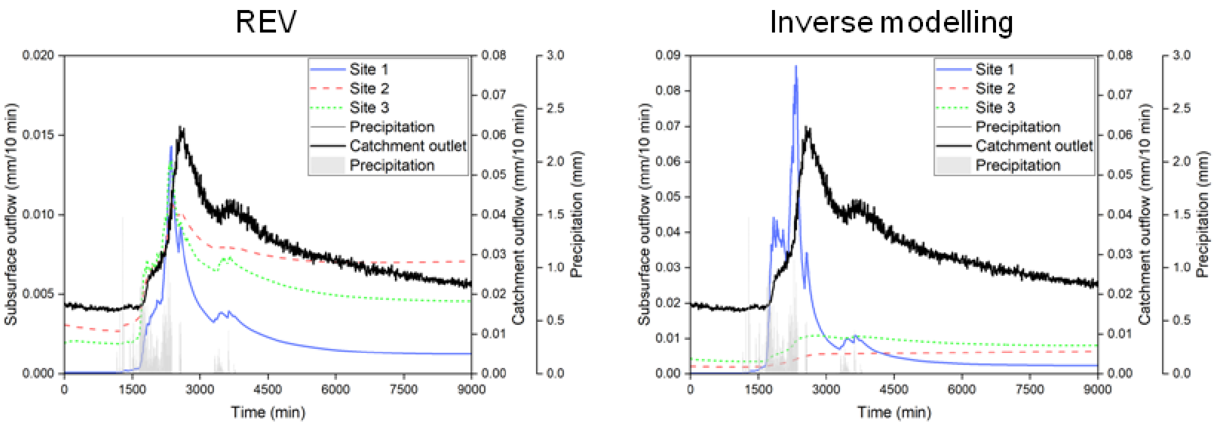

b) Large intensity rainfall event FI

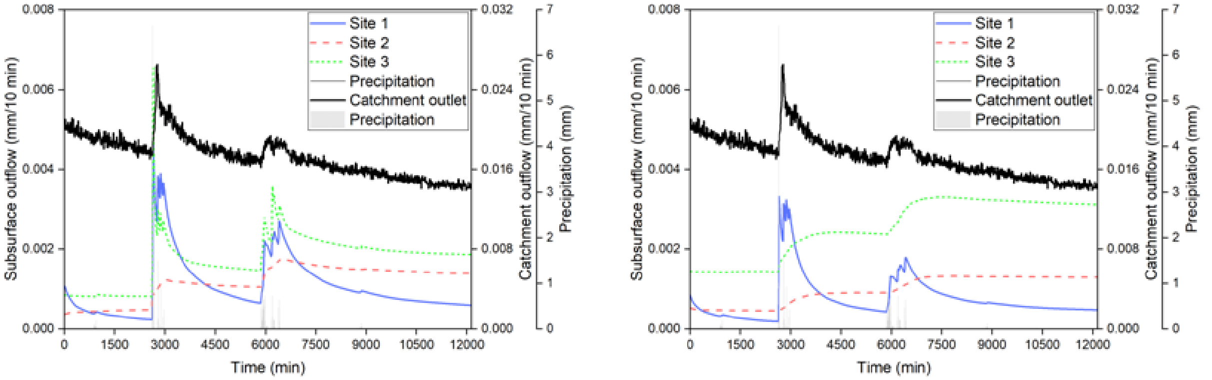

Fig. 4.7. Catchment runoff and simulated lateral subsurface flow hydrographs estimated by the REVa and the IMa for a small and large intensity rainfalls.

The VBP (volume before peak) values are given in Table 4.4. The VBP values for catchment runoff hydrographs varied from 0.11 to 0.40, suggesting positively skewed hydrographs. Among the lateral subsurface flow hydrographs estimated by both REVa and IMa, there were in total 10 hydrographs that were negatively skewed (VBP > 0.5) out of 90 hydrographs.

Table 4.4 shows that similar skewness of lateral subsurface flow hydrographs and catchment runoff hydrographs was obtained for approximately one half of rainfall events (8 out of 15). The similarity was most often obtained for the small intensity rains and site 3 (and parameters obtained from the IMa) which has the shortest distance to the Jalovecký Creek. The connectivity of that particular site with stream network probably does not develop, but the entire hillslope may be connected to the narrow riparian area existing in that part of the catchment.

Table 4.4. Volume before peak (VBP) values for catchment runoff hydrographs and simulated lateral subsurface flow hydrographs; the bold numbers show the negatively skewed hydrographs (VBP > 0.5), the yellow-marked numbers indicate the lateral subsurface flow hydrographs with skewness most similar to that of catchment runoff hydrograph; A-I are events with small intensity rainfalls, AI-FI are the large intensity rainfalls.

Rainfall event	VBP values for lateral subsurface hydrographs						Catchment's outlet runoff hydrographs VBP values
	Inverse modelling approach			REV approach			
	Site 1	Site 2	Site 3	Site 1	Site 2	Site 3	
A	**1.00**	0.35	0.15	0.02	0.34	0.05	0.11
B	0.13	0.26	0.14	0.10	0.23	0.26	0.40
C	0.39	**1.00**	0.15	0.38	0.15	0.10	0.15
D	0.38	**0.99**	0.18	0.18	0.16	0.18	0.21
E	0.08	0.06	0.08	0.06	0.05	0.08	0.16
F	**0.99**	**0.98**	**0.94**	0.04	0.16	0.18	0.11
G	0.22	0.31	0.34	0.21	0.19	0.21	0.38
H	0.17	-	0.23	0.17	-	0.19	0.37
I	0.05	-	0.04	0.08	-	0.04	0.41
AI	0.05	0.03	0.05	0.01	**0.85**	0.04	0.12
BI	0.12	**0.98**	0.25	0.11	**1.00**	0.14	0.24
CI	0.18	**0.99**	0.07	0.12	0.06	0.08	0.11
DI	0.05	0.18	0.18	0.05	0.11	0.12	0.26
EI	0.04	0.02	0.02	0.09	0.01	0.06	0.16
FI	0.10	0.5	0.49	0.09	0.11	0.11	0.25

Site 1 = Červenec - open area; Site 2 = Červenec– forest; Site 3 = PodLyscom.

The negatively skewed hydrographs were excluded from the peak times comparison. Fig. 4.8 shows that more realistic results were obtained for simulations with soil hydraulic parameters estimated by the REVa and the time delay between peaks in the lateral subsurface flow and catchment runoff were mostly about 2-3 hours. Three events with the highest rainfall intensities and comparatively higher wetness before the rain (DI, EI, FI) had shorter time delays (about 1-2 hours).

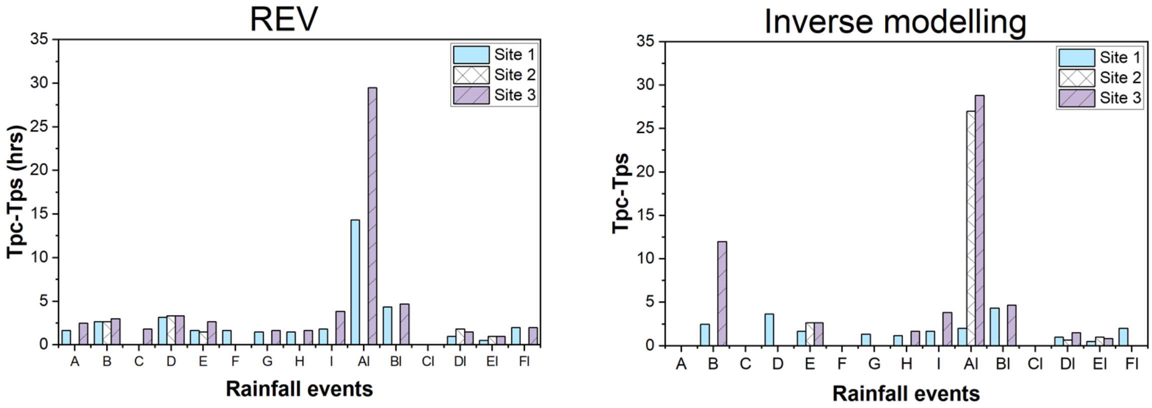

Fig. 4.8. Peak time difference (in hours) between the lateral subsurface flow (Tps) and catchment runoff (Tpc) hydrographs.

4.7. Discussion

Previous studies in the Jalovecký Creek catchment which is representative for the hydrological cycle of the highest part of the Carpathian Mountains, documented the dominant role of the pre-event water, fast runoff response to rainfall and pointed at the importance of the stony soils in catchment runoff generation (e.g. Holko and Lepistő, 1997; Kostka, 2009; Holko et al., 2011, 2018; Hlaváčiková et al., 2015, 2018, 2019). This work indicated that simulation of the lateral subsurface flow in different parts of the catchment and comparison of simulated lateral subsurface flow hydrographs with catchment runoff hydrograph could improve the understanding of the contribution of different parts of the catchment to runoff formation. Comparison of hydrographs shapes based on skewness and peak times was useful to identify the similarity. Additional criteria of hydrograph similarity can be tested when more rainfall events data are available. One of the ultimate aims of such a comparison would be the identification of typical hydrograph shapes related to certain field conditions. An example of the usefulness of such a work was recently given by Brunner et al. (2018) who used flood hydrograph shapes classification to delineate regions of similar flood behaviour in Switzerland.

Simulated soil water outflow depends on many factors, e.g. the initial wetness, soil hydraulic properties, rainfall intensity, hillslope inclination, etc. All these factors determine the shape of the lateral subsurface flow hydrographs. Our simulations showed that K_s value of the soil layers played the key role in influencing the hydrograph geometry at different initial soil conditions and rainfall intensities. An example is presented in Figs. 4.9 and 4.10.

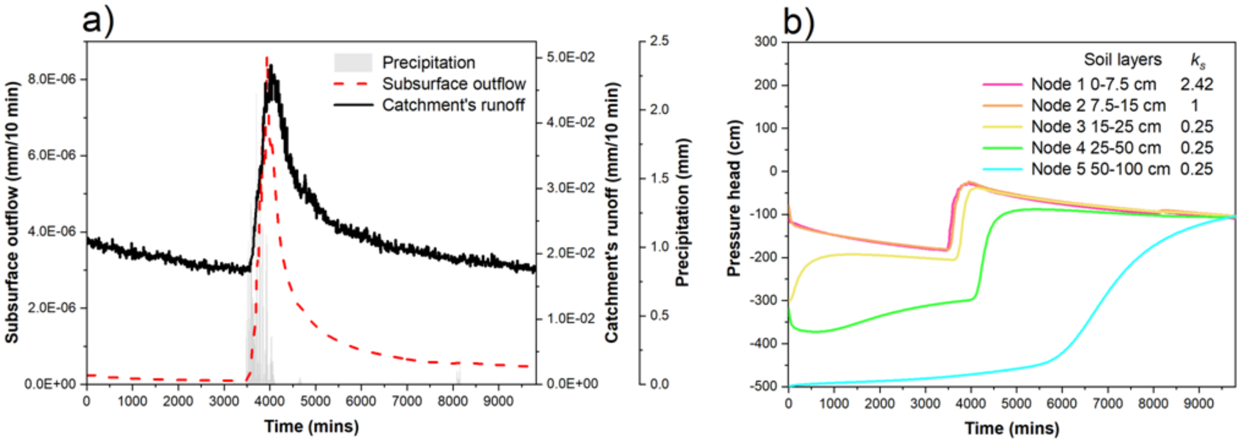

Fig. 4.9. a) Rainfall, catchment runoff and lateral subsurface flow hydrographs with positive skewness caused by the rainfall event G on site 1; b) temporal evolution of pressure head at the gradient boundary observation nodes at different soil depths estimated by the REVa for the same event and site; K_S is the saturated hydraulic conductivity in cm/min.

Fig. 4.9a shows the positively skewed catchment runoff (measured) and lateral subsurface flow (Hydrus 2D simulated) hydrographs that have similar shapes. Temporal evolution of the simulated pressure head at various soil depths is shown in Fig. 4.9b. The top soil on site 1 had high K_S values and its pressure head hydrograph followed the rainfall pulse pattern. The upper soil layers (0-15 cm) were the dominant contributors to simulated soil water outflow and the obtained hydrograph was positively skewed.

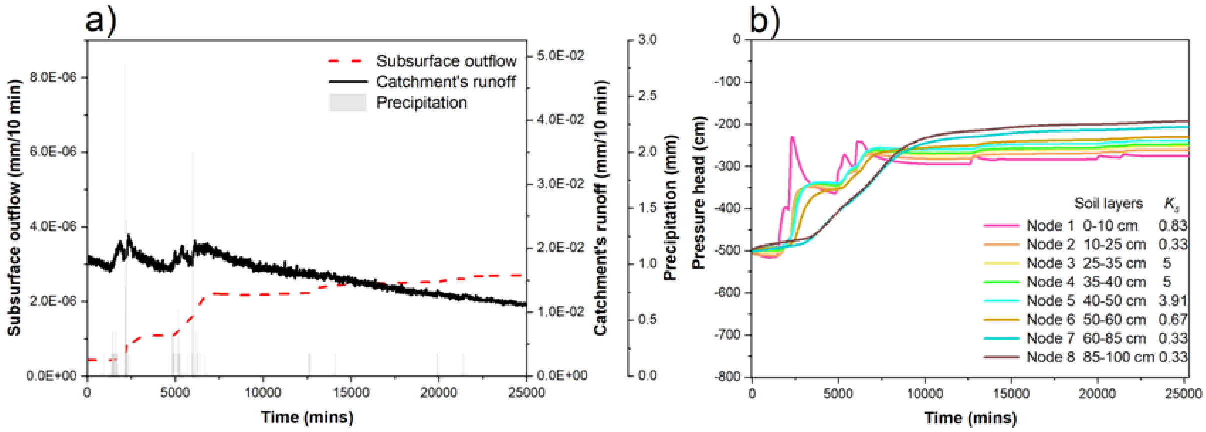

Fig. 4.10. a) Rainfall, catchment runoff hydrograph and soil water outflow hydrograph with negative skewness caused by the rainfall event F on site 2; b) temporal evolution of pressure head with time at the gradient boundary observation nodes at different soil depths estimated by inverse modelling for the same event and site; K_S is saturated hydraulic conductivity in cm/min.

Fig. 4.10a shows the negatively skewed lateral subsurface flow hydrograph. The lower soil layers on the study site (25-100 cm) had eight times greater K_s value than the top soil layers (0 15 cm) (Fig. 4.10b). Consequently, the rainfall fed by the top soil layers to lower soil layers resulted in greater outflow from the lower soil layers compared to the top soil layers. The lowest soil profile zone (depth 50-100 cm) was continuously fed by the upper soil layers that significantly increased its water storage. Since there was no flux condition at the lower soil segment boundary in our numerical simulation (see Fig. 4.2), the lateral outflow occurred only from the 50-100 cm soil depth layer. The outflow was increasing continuously until the end of the simulation. That resulted in the negative skewness of the simulated soil water outflow hydrograph.

Presence of the rock fragments decreases retention capacity of soil by reducing the soil volume. In case of REVa, it was observed that soil layers with the highest stoniness had the lowest retention capacity at each site. However, it was not like that for the IMa (see Fig. 4.5). The IMa optimizes soil hydraulic parameters by simulating moisture content according to observed moisture content. These observed soil moisture data are measured by sensors installed at various soil depths. Soil moisture sensors measure the water content at specific point without taking into account the entire soil profile, i.e. their sampling area is small. The rock fragments affect the hydraulic characteristics of moderately to highly stony soils by reducing the available soil volume for water flow that increases water dynamics (e.g. Hlaváčiková et al., 2015, 2018). The IMa takes the rock fragments into account, but only in a small area of the sampling volume. On the contrary, the REVa represents the bulk characteristics of the soil profile and changes the soil water retention curves in the soil layers according to variation of stoniness in these layers. The REVa also takes into account field and laboratory measurements of hydraulic conductivity of stony soils that make it more suitable than the IMa.

We assumed constant parameters for each layer over the entire 20 m long section of the hillslope. Future studies are needed to evaluate the performance of REVa for the soil layers which do not have constant soil hydraulic parameters.

4.8. Conclusions

Outflow from stony soils can contribute to rapid increase of catchment discharge due to small retention of such soils. Comparison of simulated lateral subsurface flow hydrographs with catchment runoff hydrographs indicated that the shapes of both were similar for about one half of the examined rainfall events.

Soil hydraulic parameters obtained from the Representative Elementary Volume approach provided more realistic simulated soil outflow hydrographs than the parameters obtained from the Inverse Modelling approach. The IMa more often resulted in the negatively skewed hydrographs and peaks that occurred after the catchment runoff peaks.

Modelling of water flow in stony soils is rare and we are not aware of studies analysing subsurface flow and catchment runoff relationships that would consider the stony soils. Future studies could examine the REVa capabilities under different initial soil conditions, soil characteristics, stoniness, rainfall intensities and slope angles.

Limiting factor in a more thorough exploration of the central idea that reduced retention of stony soils can have similar effect on catchment runoff formation as the commonly accepted and more often studied preferential flow, is related to availability of data. While networks of rain gauges supplemented by soil moisture measurements at several depths covering different landscape units of the catchment (e.g. hillslopes, riparian areas) can be established more easily, more effort is needed to obtain good field and laboratory data characterizing soil stoniness and its variability.

5. Laboratory testing of a new thermal tracer for infrared-based PTV technique for shallow overland flows[3]

5.1. Abstract

The accurate measurement of velocities of shallow overland flows normally found in the field of hydrology is essential to understand the kinematics of these flows. In view of this, we have tested the capability of a new thermal particle tracer (cold oil droplets) under controlled laboratory conditions to measure the velocity of shallow overland flows (< 2 mm depth) using the infrared-based particle tracking velocimetry (PTV) technique. Experimental apparatus comprised a soil flume 3.0 m long and 0.3 m wide with a feeder tank attached to the upstream end. Flow velocities acquired through infrared-based PTV were compared with corresponding values given by the volumetric discharge method, dye tracing, and conventional PTV (using polystyrene beads as tracer) for eleven flow conditions that combined different slopes (5, 7, 10 and 15%) and discharges (0.15 to 0.51 L s^{-1} m^{-1}). The Reynolds number (569 to 1938) marked it as quasi-laminar flow. The results showed that acquired flow velocity given by infrared-based PTV and conventional PTV techniques was closer to the mean velocity estimated by the volumetric discharge method than it was to dye tracing estimated velocity. The mean correction factor value (0.78) estimated by the infrared-based PTV technique was higher than the dye tracing estimated correction factor value (0.48). Furthermore, the detection of the leading edge of the dye tracer was difficult and the stagnation of polystyrene beads at lower discharges resulted in an underestimation of mean velocity. This research stresses the potential of using thermal imaging to estimate the velocity of shallow water bodies, because of the tracer's conspicuous visibility and independence from lighting conditions.

5.2. Introduction

Shallow overland flows often occur on hillslopes, irrigation fields, impermeable urban surfaces and natural streams in drought conditions. These flows have a significant impact on the dynamics of soil erosion and pollutant transport. Moreover, accurate velocity measurements are

---

[3] **Mujtaba, B.,** de Lima, J.L.M.P., 2018. Laboratory testing of a new thermal tracer for infrared-based PTV technique for shallow overland flows. Catena 169, 69-79. https://doi.org/ 10.1016/j.catena.2018.05.030

essential if we are to understand the hydraulic dynamics of these water bodies to develop models for the reliable prediction of soil erosion and the simulation of surface runoff and water quality.

Traditionally, dye tracing and salt tracing are the most common methods to estimate very shallow overland flow velocities in both laboratory (e.g. Abrahams and Atkinson, 1993; Lei et al., 2005) and field conditions (e.g. Abrahams et al., 1986; Wirtz et al., 2012). Differently coloured dyes and salts have been used as tracer materials for dye and salt tracing techniques in the past (e.g. Abrahams et al., 1986; Li et al., 1996; Li et al., 2002; Tatard et al., 2008). Dye tracer velocity is estimated by tracking the leading edge of dye tracer, generally regarded as surface velocity of flow (Zhang et al., 2010), whereas an electric conductivity meter is utilized in the salt tracing technique. Mean velocity estimation with these two techniques requires the correct estimation of correction factor α. However, the α value is dependent on many variables such as flow features, sediment load, slope, bathymetry roughness and microrelief, diffusion, etc. (e.g. Luk and Merz, 1992; Li et al., 1996; Dunkerley, 2001; Li and Abrahams, 1997; Zhang et al., 2010), but no reliable relationships have been found between all these parameters to enable the prediction of a reasonable value of α that would make these two techniques reliable for estimating mean overland flow velocities.

In addition, image based techniques using fluorescent particles, mainly large scale particle image velocimetry (LSPIV) and particle tracking velocimetry (PTV) have proven very reliable in the estimation of surface flow velocity in both laboratory (e.g. Weitbrecht et al., 2002; Nikora et al., 2007) and field conditions (e.g. Kantoush et al., 2011; Sidorchuk et al., 2008). In contrast to dye and salt tracing techniques, both these techniques can also explore the 2D-3D flow field characteristics, flow vortex and turbulence in bathymetries of different materials and shape. However, Tauro et al. (2017) found the PTV technique to be better than the LSPIV technique for estimating the surface velocity of natural stream flow. Various sizes of fluorescent particles have been used in the past for surface velocity estimation of shallow overland flows. Tauro et al. (2012) estimated the velocity of overland flow on an experimental hillslope plot by determining the travel time of 75 to 1180 µm fluorescent beads using image analysis techniques. For the PTV technique, Uijttewaal and Jirka (2003) used polypropylene particles (2-3 mm in diameter) for 45 mm flow depth and Nikora et al. (2007) used them for 5.1, 7 and 20 mm flow depths in controlled laboratory conditions. Sidorchuk et al. (2008) used white buoyancy floats (1 mm in diameter) for flow depths varying from 5.9 to 9.3 mm in field experiments. However, image based techniques are affected by light reflection, inhomogeneous background and lighting that is too bright or too faint. Furthermore, as flow depth further decreases, solid tracers, either floating or submerged in the flow, may be impeded by soil or an impervious surface since flow depth is not uniform because the bathymetry surface is not uniform in field conditions.

In recent years, a thermal tracer technique using an infrared thermographic approach has shown potential for shallow overland flow estimation in both laboratory (e.g. de Lima and Abrantes, 2014a) and field experiments (e.g. de Lima et al., 2015; Schuetz et al., 2012). Like dye tracing technique, surface velocity measurement starts by tracking the leading edge of heated tracer in the measurement window. Instead of using an optical camera or the naked eye which is usually associated with dye tracing technique, thermal imagery is utilized for leading edge detection. However, characterization of the surface (overland) flow kinematics using thermal tracer as particle has only been done by Tauro and Grimaldi (2017), where ice dices ($28 \times 28 \times 23$ mm^3) were used in a natural stream of 0.46 m water depth. No attempt has been made to characterize the surface velocity field of very shallow overland flow using thermal tracer as floating particle, which is normally associated with hillslope hydrology.

With this in mind, the goals of this study are: i) to test a new tracer's capability to measure the velocity of shallow overland flows without rainfall using infrared imaging and PTV algorithms; and ii) to compare the results with velocities and correction factors estimated through the dye tracing technique and velocities estimated through the conventional PTV technique for various discharge and slope conditions.

5.3. Methodology

5.3.1. Laboratory setup

Experiments were conducted on a soil flume 3.0 m long and 0.3 m wide with a feeder tank at the upstream end of the flume as shown in Fig. 5.1a and b. This flume was used in other laboratory studies (e.g. Montenegro et al., 2013; de Lima and Abrantes, 2014b). Tap water was supplied to the upstream feeder tank from head tank, which in turn applied a known discharge over the soil flume surface. The originated flow was not uniform because of the microrelief and slightly uneven soil surface.

The sandy loam soil of 1100 kg m^{-3} bulk density, containing 7 % clay, 9 % silt, 73 % sand and 11 % gravel, was passed through a 15 mm mesh to remove any vegetation or stones. After that, it was placed in the soil flume in form of thin layers and compacted to achieve 100 mm depth. When overland flow is applied on soil surface, the bathymetry shape changes as erosion and deposition processes come into play, which makes it impossible to have a qualitative and quantitative comparison of several techniques for exactly the same bathymetric conditions. In order to ensure that the microrelief on the soil surface was always the same for all experimental runs, a 2 mm crust was formed on the soil surface with a cement mix.

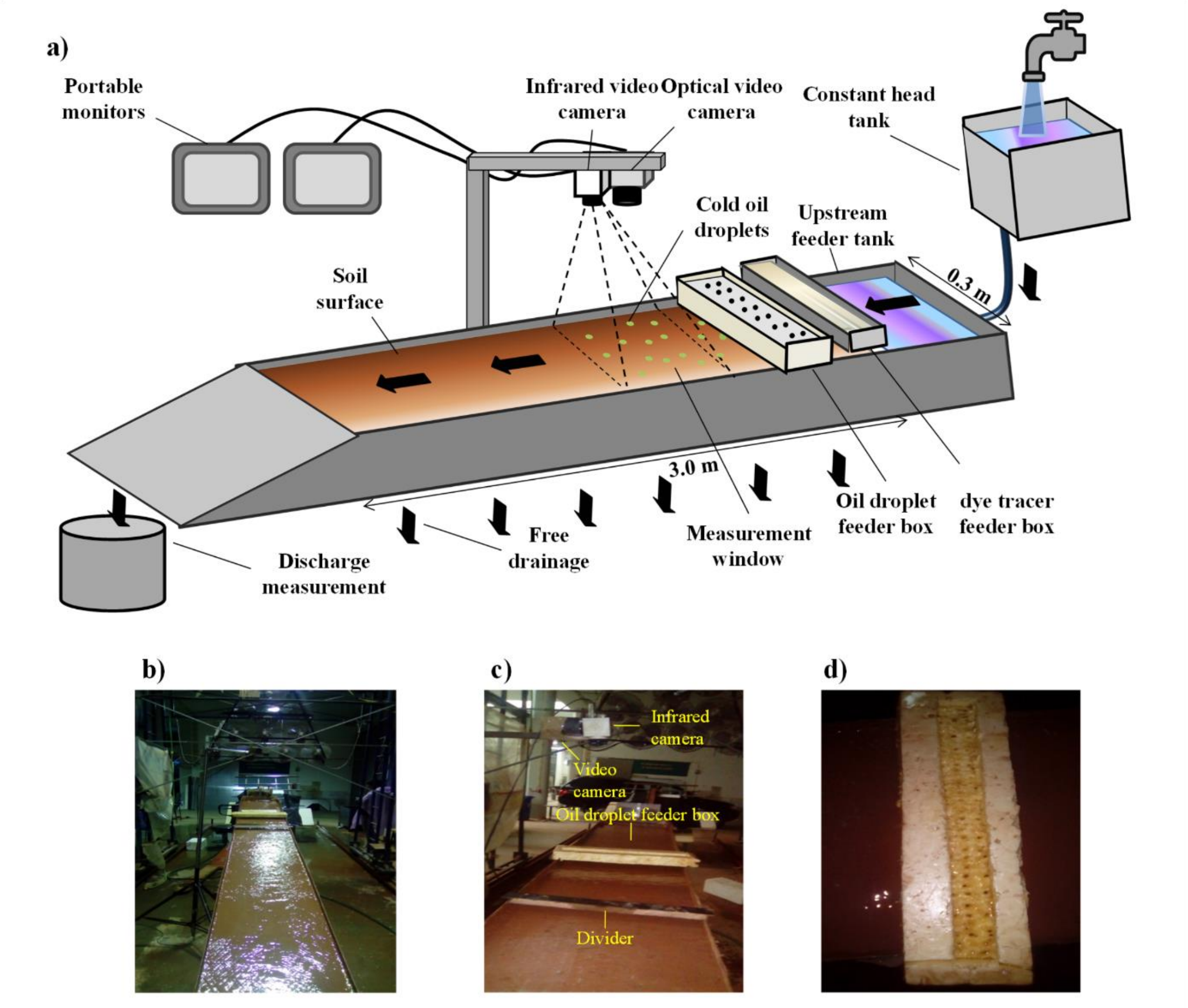

Fig. 5.1. (a) Schematic representation (not to scale), (b) overview, and (c) real representation of the laboratory setup, and (d) oil droplet feeder box used for development of infrared imaging based PTV (PTVi) technique for shallow overland flow.

5.3.2. Tracers

Cold oil droplets

Cold oil droplets were used as a tracer for the infrared imaging PTV (PTVi) technique. SAE15W-40 engine oil was used for this purpose. It has 885.1 kg m^{-3} density, 287.23 mPa s dynamic viscosity at 20 ^{0}C, is not soluble in water but floats on the water surface. Oil was converted into a cold thick paste by placing it in a refrigerator at -4 ^{0}C for two hours. After that, it was poured into the oil droplet feeder box (Fig. 5.1d), placed above the flume. Oil droplet feeder box had 3 rows of approximately 2 mm diameter holes. Oil passed through these holes and fell on the surface of the overland flow in the form of 3.6 ± 0.9 mm diameter droplets. The number of droplets that fell in 30 s was counted and their cumulative weight was then measured. Oil droplet diameter was estimated by means of the following relation:

$$\mathrm{Vol_{oil}} = \frac{4}{3}\pi r^3 \qquad 5.1)$$

where, $\mathrm{Vol_{oil}}$ is the volume of a single oil droplet in mm^3 and r is the equivalent radius of oil droplet in mm.

Each droplet made a partially floating elliptical shaped plume on the moving overland flow surface with length varying between 12 and 20 mm in the flow direction, depending on flow velocity, flow depth and soil surface micro-morphology. Cold oil droplets were applied at the start of the measurement window and they tended to fade away completely on thermal images after 1 m displacement in the case of gentle slope and low discharge experimental conditions, whereas they were visible throughout the downstream end of the flume for high discharges and steep slopes. However, their thermal signature was strong and uniform throughout the measurement window set for all discharge and slope experimental conditions. For each experimental run, 100 mL of cold oil paste was utilized, which yielded oil droplets for 3-4 min.

Floating beads and white dye

For velocity estimation through conventional PTV (PTVc) approach, spherical shaped polystyrene beads of 641 kg m^{-3} density were used. These beads were white and 2 mm in diameter. Non-fat milk of 1003 kg m^{-3} density, which is closer to water density, was used as a dye tracer. The white colour of both tracers was clearly distinguishable on the dark brown overland flow surface.

5.3.3. Tracers detection systems

Thermal videos of overland flow for the PTVi technique were obtained with an Optris PI-160 portable infrared video camera (Optris GmbH, Germany) with an optical resolution of 160 × 120 pixels, a thermal resolution of 0.1^0C, an accuracy of ±2%, 60 Hz in acquisition frequency, a lens with a view field of $23^0 \times 17^0$ and focal length of 10 mm. A GoPro Hero3 camera with a resolution of 1920 × 1080 pixels, acquired frequency of 60 Hz and a lens with field of view of $120^0 \times 70^0$ was used for real time visualization of overland flow for PTVc technique. The two cameras (Fig. 5.1c) were connected side by side to a metal support structure 0.50 m above the flume soil surface, with their perpendicular focal length directed to the field of view (measurement window of 0.3 m × 0.27 m. The measurement window started 1 m from the upstream end of the soil flume. As the cameras were adjacent to each other, their focal angles of view were slightly different.

5.3.4. Experimental procedure

Eleven scenarios with various combinations of discharges and slopes were tested to determine the velocity of shallow overland flows using PTVi and dye tracing techniques. In six of these eleven scenarios, the velocity was also estimated using the PTVc technique, as reported in Table 5.1.

Velocity estimation by each technique for a given scenario was repeated three times, which made a total of 84 experimental runs (33 for PTVi, 33 for dye tracing and 18 for PTVc technique) for eleven scenarios. For each experimental run the overland flow layer was applied to the soil surface via the feeder tank mounted at the upstream end of the soil flume. After stabilizing the flow, discharge and average flow depth measurements were taken periodically before and after each velocity estimation technique was performed, in order to ensure homogeneity of experimental conditions. For all scenarios, flow depth was less than 2 mm, making the flow very shallow.

Table 5.1. Basic characteristics of laboratory experiments conducted on soil flume.

Experiment	Slope (%)	Q (L s^{-1} m^{-1})	Flow depth (mm)	R_e	Technique
A	5	0.44	1.83	1657.02	PTVi, PTVc and dye tracing
B		0.39	1.75	1472.98	PTVi, PTVc and dye tracing
C		0.34	1.67	1304.32	PTVi and dye tracing
D		0.15	1.58	569.21	PTVi and dye tracing
E	10	0.43	1.29	1626.87	PTVi and dye tracing
F		0.31	1.25	1168.98	PTVi and dye tracing
G		0.21	1.17	805.32	PTVi, PTVc and dye tracing
H	7	0.51	1.67	1938.46	PTVi, PTVc and dye tracing
I		0.33	1.58	1246.35	PTVi, PTVc and dye tracing
J		0.18	1.25	675.14	PTVi, PTVc and dye tracing
K	15	0.44	1.33	1656.81	PTVi and dye tracing

PTVi is an infrared-imaging-based PTV technique using cold oil droplets as thermal tracer while PTVc is a conventional PTV technique using polystyrene beads as tracer and optical video camera.

Each experimental run started with dye tracing technique; 10 mL of dye tracer was applied gently and uniformly at 0.2 m distance from the upstream end of soil flume (0.8 m from the measurement window). This was done to minimize any turbulence induced by the tracer on the velocity measurements inside the measurement window. Movement of dye tracer inside the measurement window was monitored using the portable monitor of the optical video camera. If the leading edge of dye tracer was not visible enough to track, the dye tracing technique was repeated. After the dye tracing technique, the PTVc technique was performed. Floating polystyrene particles were applied manually to overland flow 0.2 m from the upstream end of the soil flume, uniformly across the width of the flume. Particle movement and quantity were monitored inside the measurement window by means of the optical video camera's portable monitor. If too few or too many particles were applied, the PTVc technique was repeated. Lastly, the PTVi technique was carried out. Cold oil droplets were applied through the oil droplet feeder box near the measurement window. After some time, oil droplets started to fall. Once a large amount of oil droplets started to fall, a thermographic video was taken for at least two minutes of cold oil droplet movement on the overland flow inside the measurement window.

5.4. Velocity estimation techniques

5.4.1. Volumetric discharge method

Flow depth was measured six times at regular intervals using a micrometer gauge inside the measurement window. Depth measurements were taken together with discharge measurements to estimate the mean flow velocity, which was calculated by simple volumetric relation:

$$\mathrm{V_m} = \frac{\mathrm{Q}}{\mathrm{hb}} \qquad 5.2)$$

where, $\mathrm{V_m}$ is the mean velocity of flow in measurement window (m s^{-1}), Q is discharge (L s^{-1}), h is depth of flow (m) and b is width of measurement window (m). The Reynolds number was calculated by the relationship used by Dunkerley (2001) and Li et al. (1996):

$$\mathrm{R_e} = \frac{4\mathrm{V_m h}}{v} \qquad 5.3)$$

where, $\mathrm{R_e}$ is the Reynolds number, h is flow depth (m) and v is the kinematic viscosity of flow (m^2 s^{-1}).

5.4.2. Dye tracing technique

Optical videos of the dye tracer were analysed using Windows Media Player 11 (Microsoft Corporation, USA) in order to track dye movement. Dye tracer velocity was determined by tracking the leading edge of the tracer from the start of the measurement window to its end, as shown in Fig. 5.2. The correction factor was estimated using the following relation:

$$\alpha_{\mathrm{dye}} = \frac{V_{\mathrm{m}}}{V_{\mathrm{dye}}} \qquad 5.4)$$

where, α_{dye} is the correction factor of the dye tracer and V_{dye} is the velocity of its leading edge (m s^{-1}).

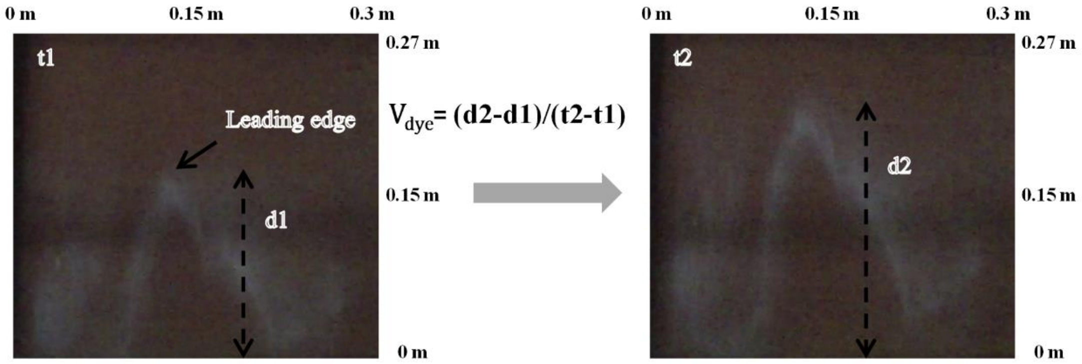

Fig. 5.2. Scheme of procedure used to measure the distance (d in m) covered by leading edge of dye tracer from time t1 to t2 (in seconds) in order to estimate dye tracer's velocity (V_{dye} in m s^{-1}).

5.4.3. PTVi and PTVc techniques

Thermographic videos of oil droplets were analysed using Optris PI Connect software to apply temperature scale limitations which ensured that the acquired images show overland flow in black and oil droplet tracers in white. For this, a temperature threshold value in the range 9.5-12.5 ^{0}C was selected for every experimental run, considering the temperature differences of oil droplets and overland flow. In the case of floating polystyrene particles, real time images acquired through optical videos were converted into greyscale to distinguish tracer particles (white) from overland flow (black).

The PTVlab application developed by Brevis et al. (2011) was used to estimate the velocity fields of very shallow overland flows for the PTVi and PTVc techniques. Velocity field estimation through the PTVi technique involves identifying the oil droplets' plumes' centroids through particle detection algorithms and then finding them in next image by means of temporal matching solution algorithms, as shown in Fig. 5.3. The same procedure was used in the PTVc technique (Fig. 5.4).

Brevis et al. (2011) developed an integrated cross-correlation/relaxation algorithm which was coded in Matlab as a PTVLab application. It employs a Gaussian mask (Takehara and Etoh, 1998) and the dynamic threshold binarization (Ohmi and Li, 2000) algorithms for particle detection. As for solving the temporal matching problem, cross-correlation (CC) (e.g. Uemura et al., 1989; Hassan et al., 1992), the relaxation method (RM) (e.g. Wu and Pairman, 1995; Ohmi and Li, 2000) and an integrated cross-correlation/relaxation algorithm (ICCRM) can be used. The fundamental idea of estimating the velocity of tracer particles by means of a CC algorithm is the correlation of light intensity matrices of interrogation windows centred at each detected particle associated with two images. CC is more reliable than RM for low velocity gradients and can even be used for single particle velocity estimation. As in the PTVi technique, sometimes there were frames in which only one particle was available to trace, and the flow velocity for each slope and discharge condition was also low. This is why CC was chosen to solve the temporal matching problem. The Gaussian mask technique was used for particle detection since it requires less computation time.

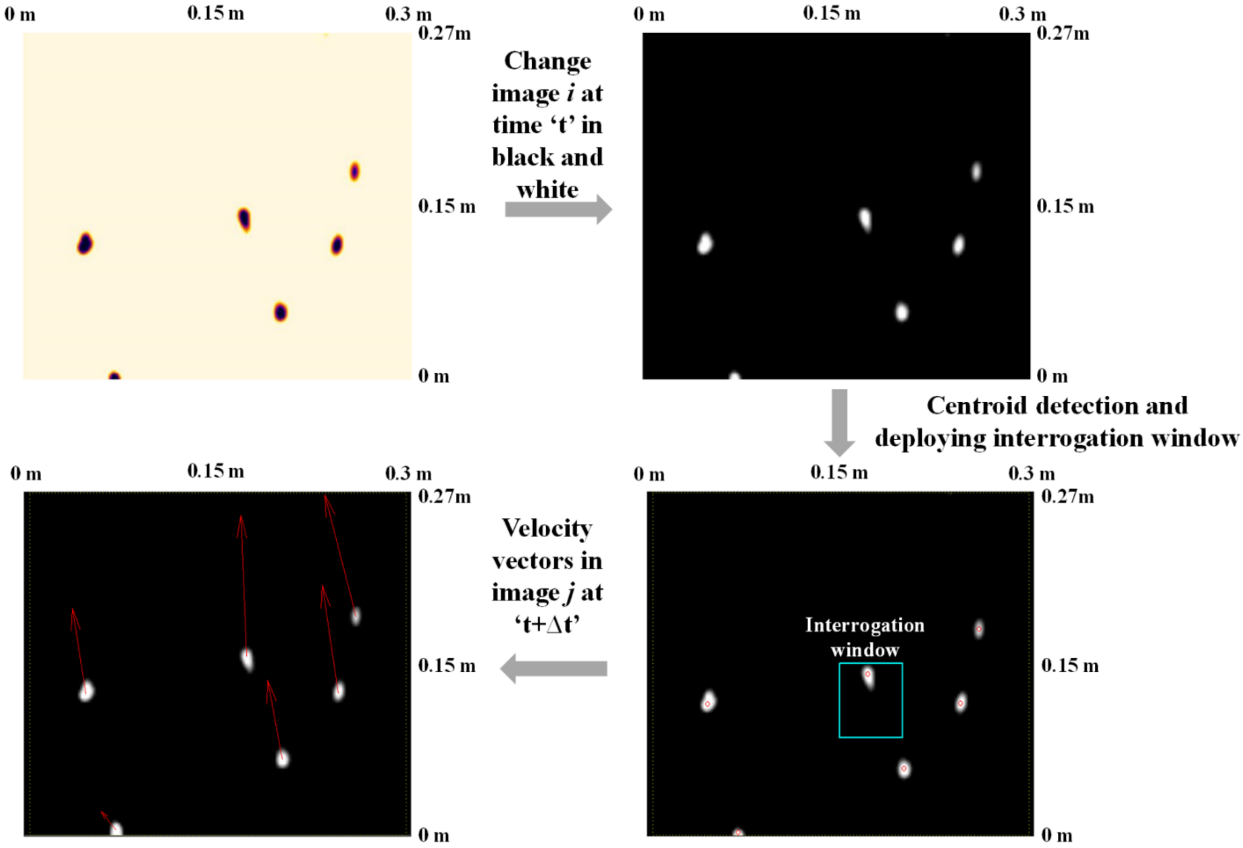

Fig. 5.3. Fundamental concept of velocity vectors estimation for PTVi technique where oil droplets are tracked in two thermographic images *i* and *j*.

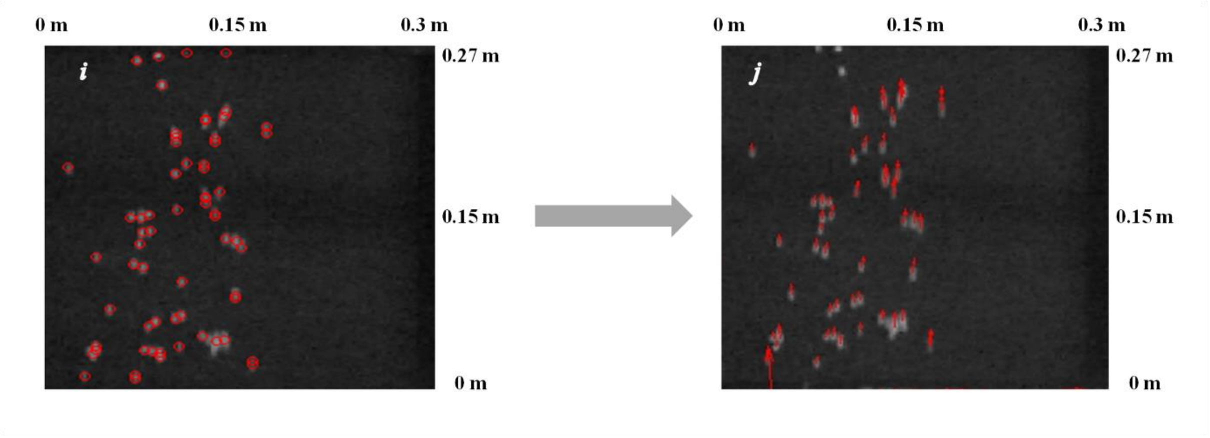

Fig. 5.4. Schematic representation of PTVc technique where centroids of polystyrene beads were detected in image *i* (red circles) and velocity vectors (red arrows) were estimated by detecting their corresponding centroids in image *j*.

The procedure reported by Tauro and Grimaldi (2017) was used to calculate the time averaged particle densities D_{PTVi} and D_{PTVc} for their corresponding PTVi and PTVc techniques, in terms of the ratio between particles detected and image resolution of measurement window. The Gaussian Kernel value was taken as 9 pixels for the oil droplet tracer and 6 pixels for polystyrene beads. Acquired D_{PTVi} and D_{PTVc} (Table 5.2) values were quite similar to the Tauro and Grimaldi (2017) study of flow visualization using ice dices as particle thermal tracer, thus supporting the use of the PTV technique.

Table 5.2. Time-averaged particle densities (particles/total pixels) D_{PTVi} and D_{PTVc} for PTVi and PTVc techniques, respectively.

Experiment	N_{PTVi}	N_{PTVc}	i_{PTVi}	i_{PTVc}	D_{PTVi}	D_{PTVc}
A	673	150	5.4	89.3	3.5×10^{-4}	2.1×10^{-4}
B	765	100	5.8	78.9	3.8×10^{-4}	1.9×10^{-4}
C	865	-	6.5	-	4.2×10^{-4}	-
D	615	-	6.7	-	4.4×10^{-4}	-
E	665	-	4.9	-	3.2×10^{-4}	-
F	725	-	6.4	-	4.2×10^{-4}	-
G	700	131	7.3	133.2	4.8×10^{-4}	3.2×10^{-4}
H	634	100	6.1	98.8	4.0×10^{-4}	2.3×10^{-4}
I	757	100	4.6	103.2	3.0×10^{-4}	2.4×10^{-4}
J	780	150	7.8	150.6	5.1×10^{-4}	3.6×10^{-4}
K	670	-	4.8	-	3.1×10^{-4}	-

i_{PTVi} and i_{PTVc} are average number of particles in their corresponding frames, N_{PTVi} and N_{PTVc}, for PTVi and PTVc techniques, respectively.

The pre-processing step in image processing is to accurately determine the parameter values of the PTV algorithm in order to correctly estimate the magnitude of the velocity vectors. Parameter values are normally determined by changing the parameter values one at a time and comparing the results with those provided by another valid technique in different sections of measurement window. However, in our case, other techniques such as laser Doppler velocimetry and acoustic Doppler velocimetry could not be used due to the very shallow flow depth (< 2 mm). In this situation, the parameter values were determined by manually tracking the oil droplets in the images. The plume lengths of the oil droplets varied between 12-20 mm in the flow direction and they have slightly different velocities according to their size. Plumes measuring 12 mm, 15 mm and 20 mm were taken as references for three experiments (D, F and K) and their velocity was estimated by dividing the distance they covered from the time steps of the oil droplets' tracked thermal images. Same oil droplet images were used to estimate the velocity through the PTV algorithm by changing the parameter values. After obtaining velocity values near to those manually observed, the parameter values were decided as shown in Table 5.3. The same procedure was implemented for the PTVc technique.

Table 5.3. Cross-correlation and Gaussian mask parameter values for PTVi and PTVc techniques.

Parameter	Unit	PTVi technique	PTVc technique
Correlation threshold	-	0.3	0.5
Particle diameter	Pixel	6 or 9	6
Particle intensity threshold	-	70	90
Size of interrogation window	Pixel	24 or 30	20
Minimum correlation value	-	0.3	0.7
Similarity among neighbour particles	%	15	25

After the parameter values, the shallow overland flow velocity was estimated. A series of 600-900 frames were selected for the PTVi technique and 100-150 images were selected for the PTVc technique. A greater number of frames were selected for the PTVi technique because of the lower average number of oil droplets (i_{PTVi}) compared to the average number of polystyrene beads (i_{PTVc}), reported in Table 5.2. This ensured that the velocity field estimation could be done for whole measurement window using the PTVi technique. The amount of oil droplets in each frame could be increased by adding extra holes in the oil droplet feeder box. However, this could allow oil droplets to collide and mix with each other to make larger plumes, which would make it harder for the PTV technique to detect the centroid. If more oil droplets are required for future research, it is recommended that the distance between openings (oil drop formers) and the number of rows should both be increased in the oil feeder box to counter this effect. Two cold, white, wooden sticks, measuring 50 mm longitudinally were used for the metric calibration of both techniques. These sticks were placed inside the measurement window with their longitudinal side facing the flow direction.

Flow velocity ($\mathrm{V_{PTVi}}$) is calculated by taking the average of the time-averaged velocity maps yielded by the PTVi technique. The same procedure was followed for the flow velocity ($\mathrm{V_{PTVc}}$) calculation using the PTVc technique. The correction factor for the PTVi technique was estimated by following relation:

$$\alpha_{\mathrm{PTVi}} = \frac{\mathrm{V_m}}{\mathrm{V_{PTVi}}} \qquad 5.5)$$

where, α_{PTVi} is the correction factor of the PTVi technique and $\mathrm{V_{PTVi}}$ is the average velocity of the time-averaged velocity maps estimated with the PTVi technique (m s^{-1}).

5.5. Results and discussion

5.5.1. Estimated velocities through dye tracing, PTVi and PTVc techniques

Cold oil droplet tracer was used to characterize the shallow overland flow velocity field using the PTVi technique; Fig. 5.5 presents experiment C in terms of time-averaged velocity magnitude map. The map has blank areas which oil droplets did not pass across. As the soil crust was slightly uneven, the resulting flow was not uniform and had a wave-like motion which was visible to the naked eye. Maximum velocities were found closer to the centre of the flume's transversal section from the left side of the flow direction.

The flow velocities measured through dye tracing and the PTVi technique varied from 0.3 to 0.91 m s^{-1} and 0.16 to 0.42 m s^{-1}, respectively. The PTVc technique estimated velocities varied from 0.11 to 0.33 m s^{-1}, as reported in Table 5.4. The Reynolds number varied from 569 to 1938 indicating quasi-laminar flow as described by Li et al. (1997). A comparison of all velocity data measured through PTVi, PTVc and dye tracing techniques with $\mathrm{V_m}$ values estimated through the volumetric discharge method is shown in Fig. 5.6. $\mathrm{V_{dye}}$ values are above the 1:1 line while the $\mathrm{V_{PTVi}}$ and $\mathrm{V_{PTVc}}$ values are closer to it. This suggests that the PTVi and PTVc techniques were more reliable for estimating the mean velocity of shallow overland flows.

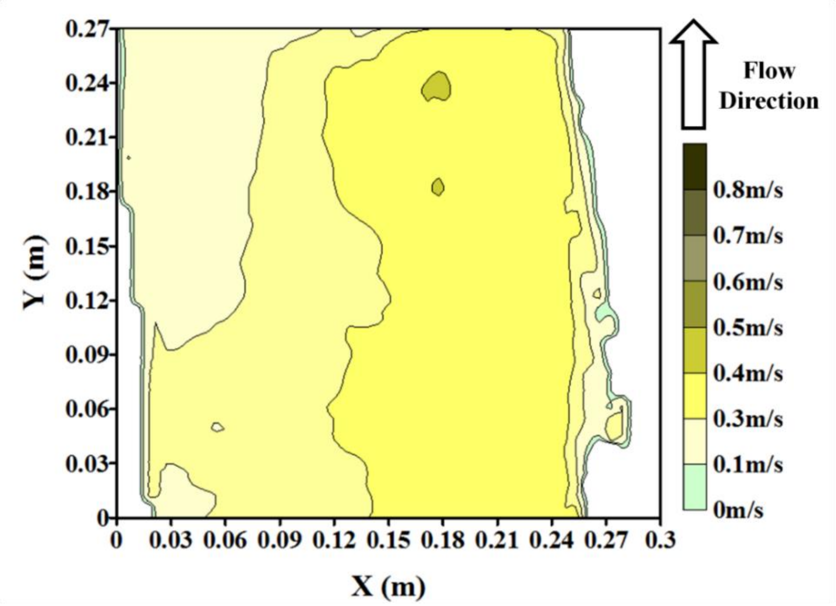

Fig. 5.5. Time averaged velocity maps of experiment C obtained through PTVi technique.

Table 5.4. Mean values of velocities and correction factors estimated through dye tracer, PTVi and PTVc techniques with their standard deviations in brackets.

Experiment	V_m (m s^{-1})	V_{dye} (m s^{-1})	α_{dye}	V_{PTVi} (m s^{-1})	α_{PTVi}	V_{PTVc} (m s^{-1})
A	0.24(0.00)	0.37(0.01)	0.65(0.02)	0.27(0.01)	0.87(0.04)	0.28(0.01)
B	0.22(0.00)	0.41(0.01)	0.55(0.02)	0.28(0.04)	0.79(0.10)	0.26(0.01)
C	0.21(0.00)	0.42(0.01)	0.49(0.02)	0.25(0.02)	0.81(0.06)	-
D	0.09(0.00)	0.30(0.01)	0.31(0.01)	0.16(0.01)	0.59(0.04)	-
E	0.33(0.01)	0.62(0.03)	0.54(0.02)	0.40(0.02)	0.83(0.04)	-
F	0.25(0.00)	0.45(0.01)	0.55(0.02)	0.31(0.02)	0.80(0.06)	-
G	0.18(0.00)	0.42(0.03)	0.43(0.03)	0.23(0.02)	0.78(0.07)	0.15(0.03)
H	0.31(0.00)	0.51(0.02)	0.60(0.02)	0.37(0.01)	0.84(0.03)	0.33(0.01)
I	0.21(0.00)	0.45(0.01)	0.46(0.02)	0.27(0.02)	0.78(0.06)	0.22(0.01)
J	0.14(0.00)	0.39(0.01)	0.37(0.01)	0.20(0.04)	0.70(0.08)	0.11(0.02)
K	0.33(0.01)	0.91(0.11)	0.36(0.06)	0.42(0.04)	0.77(0.08)	-

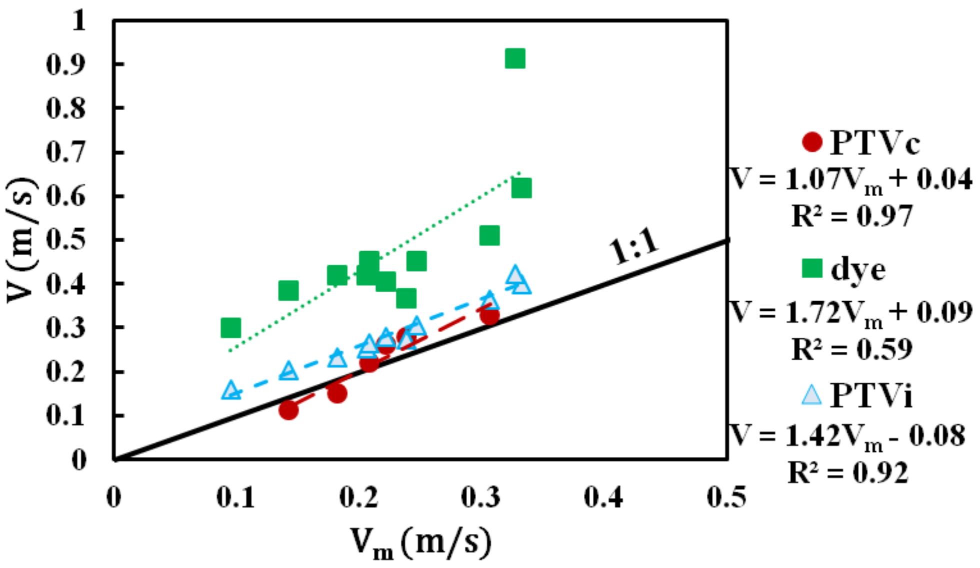

Fig. 5.6. Comparison between shallow flow velocities (V) measured by PTVi, PTVc and dye tracing techniques and mean velocity (V_m) measured through volumetric discharge method for all eleven scenarios. 1:1 line and linear regressions to determine coefficient of determination (R^2) were also plotted.

In the case of a quasi-laminar flow of shallow depth, in millimetres, where the flow is showing the characteristics of turbulent flow but not fully turbulent, the velocity profile shape is parabolic (Zhang et al., 2010). For fully turbulent flows, the velocity profile is nearly uniform throughout the flow depth. This shows that surface velocity is closer to mean velocity in turbulent flow and more so in quasi laminar flow. When dye tracer is applied to quasi laminar overland flow, it introduces turbulence in the flow, which increases flow velocity and makes a parabolic shaped plume on flow surface due to the dispersion and advection processes (Emmett, 1970). The dye tracer's surface velocity (leading edge velocity) is higher than its centroid velocity, generally known as theoretical mean velocity of flow given that the tracer is retained on the flow surface. However, tracking the centroid of the dye plume is difficult if not impossible because it is larger and continually changes shape. Also, the V_m values were estimated without any induction of tracer. This might have led to larger differences in velocity values as compared to the V_{dye} values in quasi-laminar flow in our case and noted by other researchers such as Dunkerley (2001), Zhang et al. (2010) and de Lima and Abrantes (2014a). However, the experimental conditions of these researchers were different from ours, but as a general trend V_{dye} is much higher than V_m in quasi-laminar flow than in turbulent flow.

In the case of oil droplets, elliptical shaped plumes are formed due to turbulent dispersion and they are smaller with a centroid that can be easily detected by the particle detection algorithm. Since they are smaller in size and fewer in number, the induction quantity of oil droplets in overland flow is less, and therefore changes in flow velocity are fewer than for dye tracer. Furthermore, oil droplets stick together and are not soluble in water due to adhesion, while dye tracer is also involved with a diffusion process to some extent. These factors might explain why V_{PTVi} values are closer to V_m values.

Flow velocity estimated through PTVc technique uses floating polystyrene solid particles which are smaller in size and lower in density than cold oil droplet plumes. This led to fewer disturbances in flow hydraulics by polystyrene particles than by cold oil droplet plumes. Also, oil droplets were added on the overland flow surface at the start of the measurement window. Oil droplets formed ripples in the flow due to their fall impact on the overland flow surface. All these factors could help explain why the V_{PTVi} values are higher than the V_{PTVc} values, as shown in Fig. 5.7.

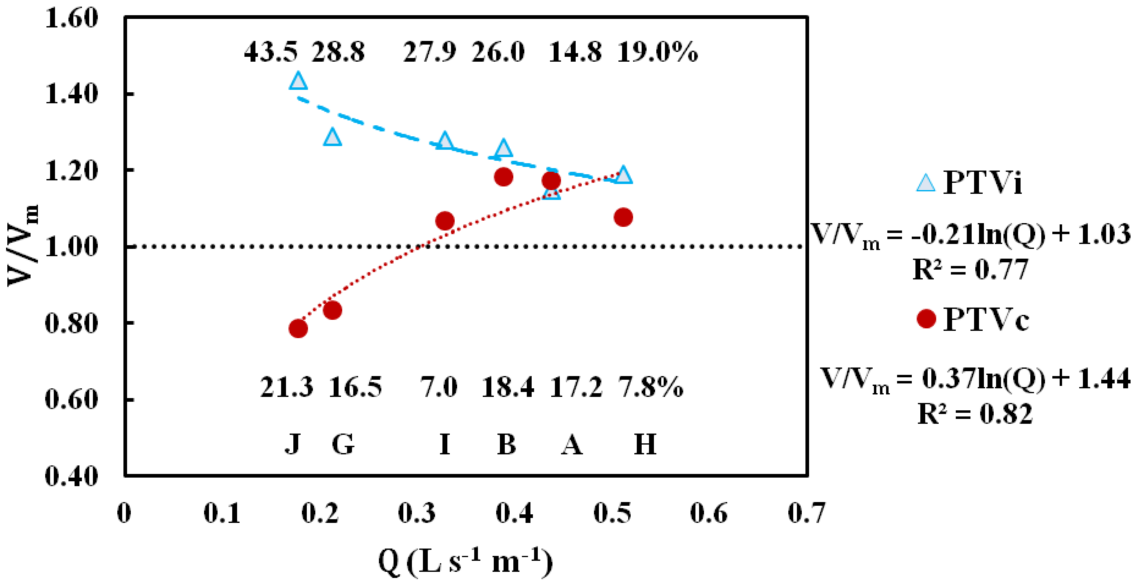

Fig. 5.7. Comparison of shallow flow velocities (V) measured through PTVc and PTVi techniques with mean velocities (V_m) measured through volumetric relation for discharges of experiments (A, B, G, H, I and J) along with their corresponding relative differences $\left(\frac{V-V_m}{V_m}\right)$ in percentage (%) and logarithmic regressions (R^2).

The PTVi technique overestimated the mean flow velocities for lower discharges but tend to come closer to mean velocity for higher discharges. The relative difference of V_{PTVi} with V_m

decreased from 43.5% to 14.8% with an increase in discharge from 0.18 to 0.51 L s^{-1} m^{-1}. However, the PTVc technique underestimated the mean flow velocities for lower discharges (0.18 and 0.21 L s^{-1} m^{-1}) but showed slightly better results than the PTVi technique for higher discharges (0.33 to 0.51 L s^{-1} m^{-1}).

The higher relative difference values of V_{PTVi} with V_m at lower discharges could be attributed to the intrusion of the impact of oil droplet fall and droplet size in shallow flow kinematics which were more noticeable as V_m values were small. As discharge increased, V_m values increased, which led to lower relative differences. In the case of polystyrene beads, some of these floating particles were underwater with their movement at discharges of smaller depths (< 2 mm) being hindered by the friction and shear stress presented by the bed surface. These effects might have been more dominant than the advection caused by the flow, which resulted in an underestimation of mean flow velocity at lower discharges.

5.5.2. Correction factors estimated through dye tracing and PTVi techniques

The correction factors estimated through dye tracing and PTVi techniques were compared for two reasons. First, the tracers of both techniques are liquid and second, flow depth was very small (<2 mm), which permits the assumption that oil droplet movement might also have been affected by a velocity profile lower than surface velocity. Correction factor values varied from 0.31 to 0.65 with mean value of 0.48 for dye tracer, and from 0.59 to 0.87 with a mean value of 0.78 for the PTVi technique (Table 5.4). The measured α_{dye} range did not include Horton's theoretical value of 0.67 for quasi-laminar flow (Horton et al., 1934) and its mean value was somewhat less than 0.67, probably because of very shallow flow. The flow depth varied from 1.17 to 1.83 mm. Emmett (1970) observed that α values tend to decrease the shallower the flow, which was fairly similar in our case. However, α_{PTVi}values were rather larger than the α_{dye}values for every scenario, as shown in Fig. 5.8.

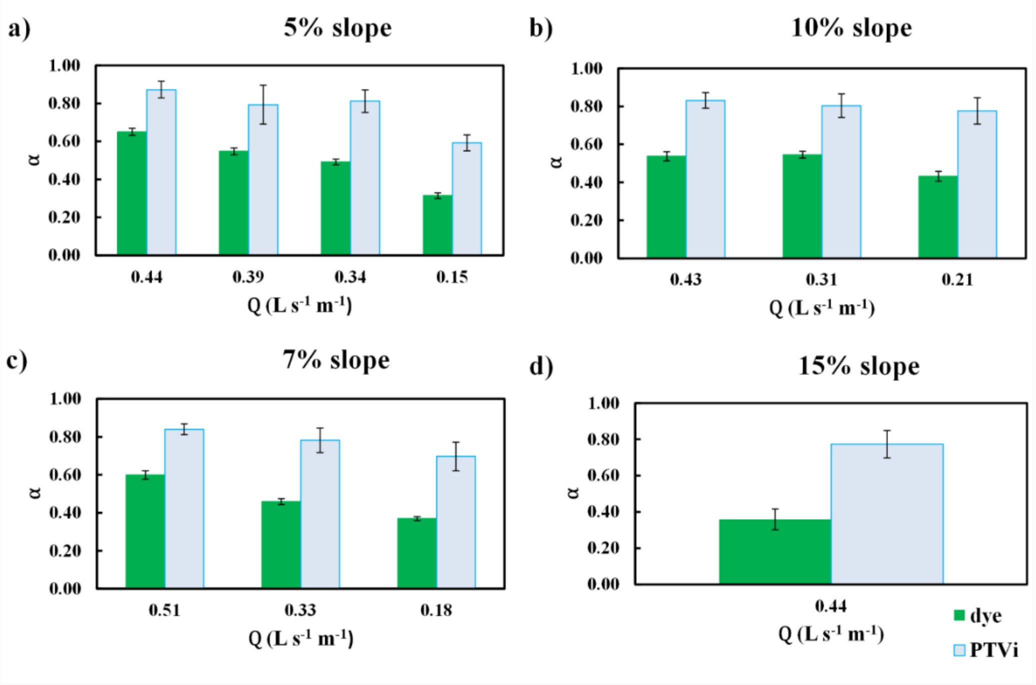

Fig. 5.8. Correction factors (α) estimated through dye tracing and PTVi technique for the eleven scenarios, conducted on a) 5%, b) 10%, c) 7% and d) 15% slopes for different discharge conditions.

The correction factor increased with the Reynolds number for both techniques, as shown in Fig. 5.9a. The same pattern can be seen in Li and Abrahams (1997) and Zhang et al. (2010). However, they were unable to find any significant relationship between the Reynolds number and the correction factor for overland flow in laminar regime. Li and Abrahams (1997) noted the rising trend of the correction factor of salt tracer with the Reynolds number for 5.5^0 and 3.5^0 slopes but found the Reynolds number to be independent of the correction factor for a 1.2^0 slope, for which a large set of data was acquired and suggested relation was independent due to inconsistency. Zhang et al (2010) observed the dye tracer over a length of 2 m. In our study, a relation was obtained probably because of the small observational area (measurement window) and less observed data. However, it must be noted that goal of this study was to compare the PTVi technique with the dye tracing technique and to determine the feasibility of the PTVi technique. The best fit-relation was for the PTVi technique (R^2=0.74), which suggests that as flow becomes turbulent, the correction factor will come closer to value 1 and be able to mimic the mean flow velocity for a depth of less than 2 mm. Further study on this is required.

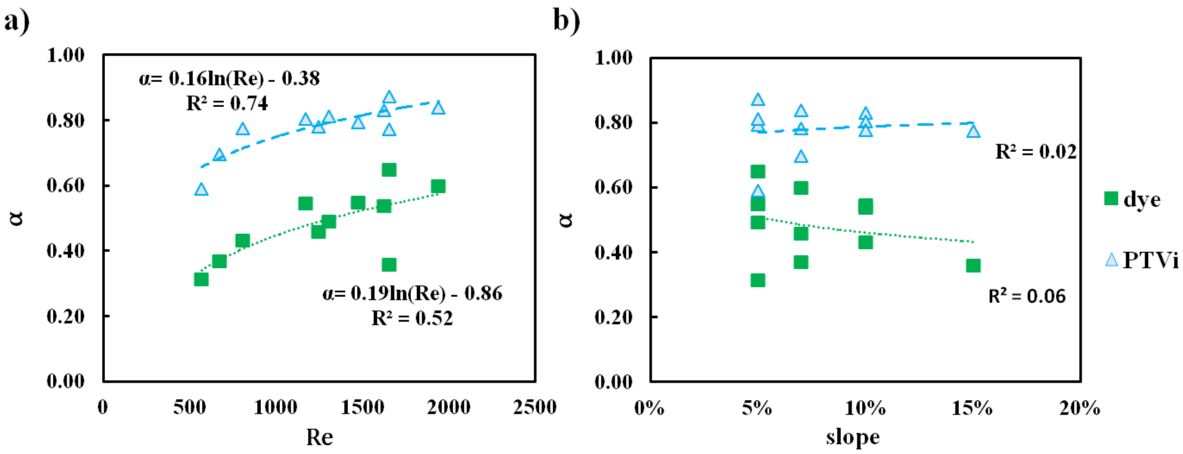

Fig. 5.9. Relationship of a) Reynolds number R_e and b) slope with correction factor α estimated through dye tracing and PTVi technique with their corresponding coefficient of determination (R^2) values obtained through logarithmic regression.

We did not find any significant relation between the slope gradient and correction factors for the dye tracing and PTVi techniques (Fig. 5.9b), contrary to Zhang et al. (2010) who found the slope varied inversely to the correction factor for the Re range from 664 to 5899. However, they did not suggest any relation in the quasi-laminar flow regime. Also, in our study, constant series of discharges were not applied to each slope, which may have resulted in no relation differing from Zhang et al. (2010), who applied the same series of discharges to each studied slope.

5.5.3. Errors and restrictions in the dye tracing, PTVi and PTVc techniques

According to Flury and Wai (2003), density closer to that of water, high visibility and low toxicity are the characteristics of a suitable tracer. Density is not an issue for any of these three techniques, but detection of the leading edge of dye tracer is an issue, even with the use of an optical camera (Fig. 5.10a). This problem meant that dye tracing experiments sometimes had to be repeated from three to six times for a given scenario to obtain three reliable values. Increasing the volume of dye tracer might solve the visibility issue. However, it will also affect flow hydraulics further by introducing a wave and more turbulence in overland flow, resulting in an additional overestimation of velocities, as found by de Lima and Abrantes (2014a). These high velocities will result in further underestimation of α_{dye}. Using an optical tachometer or a higher resolution optical camera would be more helpful in detecting the leading edge of the dye tracer than increasing the dye tracer volume.

The PTVc technique requires significant illumination of its tracer relative to background and is more affected by light reflection. Even under laboratory conditions, it sometimes becomes difficult to obtain good experimental conditions for the PTVc technique. In addition, polystyrene beads were unable to propagate properly on lower discharges and the consequent lower depths and this resulted in the underestimation of velocities in our study, as shown in Fig. 5.10b. This suggests that the applicability of polystyrene beads (2 mm diameter) on lower discharges of lower depth and uneven bathymetry (normally found in field conditions) is restricted. Using smaller particles will help to solve this problem but it will also require better optical camera and lighting conditions.

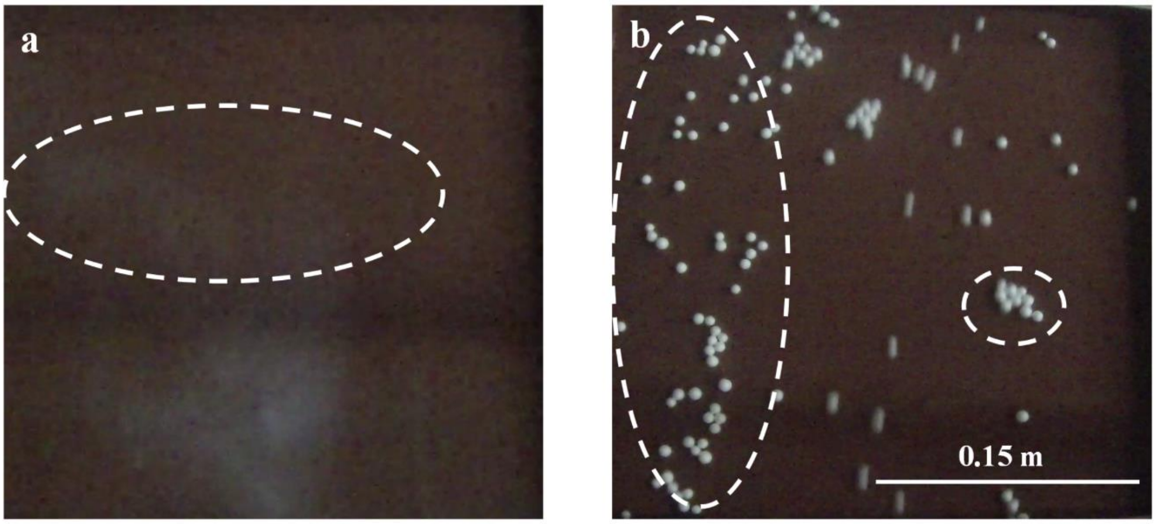

Fig. 5.10. (a) Failed detection of leading edge (in white circle) of small amount (10 mL) of dye tracer for experiment A and (b) stagnation of polystyrene beads (in white circles) at lower discharge of experiment J resulting in underestimation of shallow overland flow mean velocity by PTVc technique.

The PTVi technique's performance is dependent on the temperature differences of tracer and flow. This technique does not require illumination and could be performed in the day time or at night. The PTVi technique's tracer is easily visible courtesy of thermal imagery, but certain errors and restrictions are also associated with cold oil droplet tracer. Because the oil droplet is a liquid it sometimes changes shape and its temperature continuously increases as it propagates on the flow surface. These phenomena affect a given tracer's intensity and diameter value in the PTV algorithm, which in turn results in failure to detect particles, as shown in Fig. 5.11. It is recommended that tracer detection should be done at a lower intensity threshold so that the tracer can be detected at the lowest possible temperature difference between tracer and overland flow. Furthermore, oil droplet toxicity and its applicability in field conditions are its other disadvantages. Although the tracer can be transported on field sites in ice boxes studies are needed regarding its applicability in field conditions relative to its performance and transportation hurdles. Also, the feasibility of this tracer using the PTVi technique on agitated turbulent flows under rainfall need to be tested.

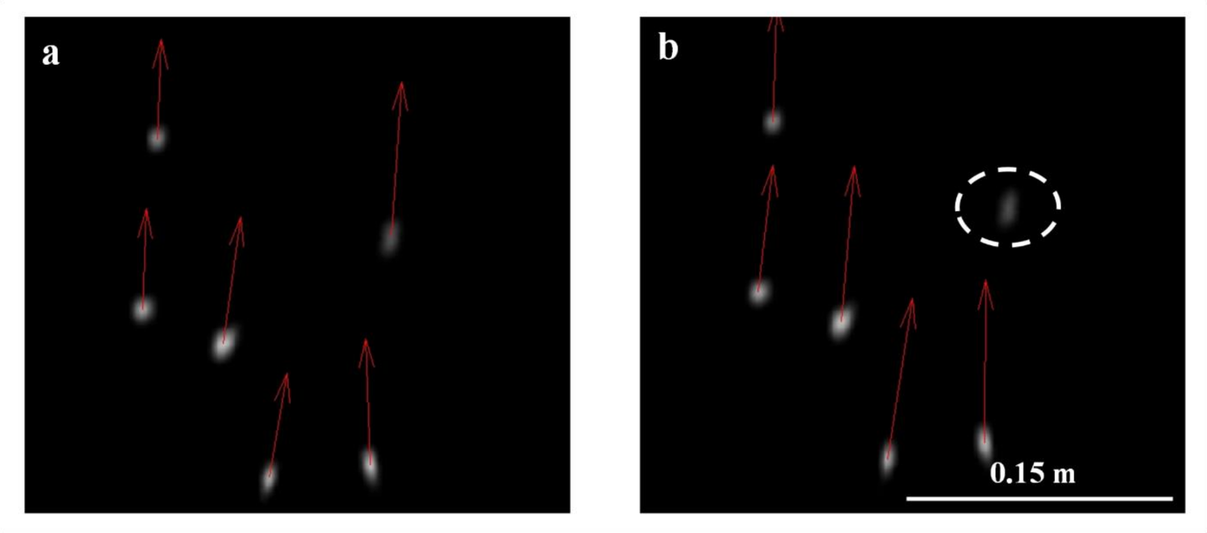

Fig. 5.11. Shape and intensity of oil droplet (in white circle) changes in two corresponding frames (a) and (b), resulting in non-detection of oil droplet's centroid.

Indeed, expertise in image processing is required for both the PTVi and PTVc techniques in order to determine the optimum values of parameters such as interrogation window size, intensity threshold and correlation value, etc. The dye tracing technique, however, does not require that kind of expertise level but, since it is a crude method, it overestimates mean flow velocity to a greater extent, especially in the case of quasi-laminar flow. In view of this, this research proposes to test the capability of a single oil droplet to estimate the flow velocity of very shallow flows under different slope, depth, discharge and bathymetry conditions. As it is far less intrusive and more readily visible through thermal imagery, an oil droplet could be tracked manually without the use of sophisticated tracking algorithms. Also, it may induce almost negligible toxicity in shallow environmental flows because of its smaller size.

5.6. Conclusions

In this study, the capacity of cold oil droplets as a tracer to estimate the velocity of shallow overland flows (without rainfall impact) using infrared-image-based particle tracking velocimetry (PTV) technique was tested. This new approach was compared with dye tracing and the conventional PTV technique. Polystyrene beads were used as a tracer for the conventional PTV technique, while an optical camera was used to detect the dye tracer and polystyrene beads. The following conclusions have been drawn:

i. The infrared-based PTV technique's estimated velocities were closer to mean velocities measured through the volumetric discharge method than were those given by the dye tracing method. The correction factor estimated through the infrared-based PTV technique was closer to 1 (α_{PTVi}= 0.78) than that (α_{dye}= 0.48) of the dye tracing technique.

ii. Visibility of oil droplet plumes was clearer than the leading edge of the dye tracer.

iii. At higher discharges (0.33 to 0.51 L s^{-1} m^{-1}), the conventional PTV technique's estimated velocities were slightly closer to the mean velocities than those of the infrared-based PTV technique. However, on lower discharges (0.18 and 0.21 L s^{-1} m^{-1}), the conventional PTV technique underestimated the mean velocities as some polystyrene beads became trapped on the soil surface; the infrared-based PTV technique does not face this problem.

iv. The illumination conditions of the tracer with respect to background and light reflection from the water surface do not affect the infrared-based PTV technique. Visibility of the oil droplet tracer is only dependent on the temperature difference of the water and oil droplet, which enables it to perform in bad light conditions, such as at night.

Cold oil droplet tracer has shown potential to characterize shallow (< 2 mm depth) overland flow kinematics in a quasi-laminar flow regime. However, further studies are needed to ascertain the feasibility of this tracer using the infrared-based PTV technique on agitated turbulent flows with rainfall. Certain disadvantages are associated with the infrared-based PTV technique's tracer, especially its applicability in field conditions and any potential toxicity.

6. Laboratory testing of a one-dimensional cascade model for runoff and soil erosion on converging and diverging plane surfaces

6.1. Abstract

A one-dimensional numerical overland flow model that uses the cascade plane theory is developed for the estimation of rainfall induced runoff and soil erosion on converging and diverging plane surfaces. The model is comprised of three components: (i) soil infiltration component uses Horton's infiltration equation, (ii) overland flow component uses the kinematic wave approximation of the one-dimensional Saint-Venant shallow water equations for a cascade of planes, and (iii) soil erosion component is based on the sediment transport continuity equation. The model's performance was evaluated by comparing numerical results with observed data, which were collected in controlled laboratory conditions. The laboratory setup was comprised of a rainfall simulator and a soil flume of planar circular sector geometry, of 2.02 m length and limited by 0.10 m and 2.10 m arc lengths, that led to the formation of converging and diverging flow conditions. Four independent experiments were conducted on converging and diverging flow surface conditions for different combinations of slope and rainfall. Overall, simulated hydrographs and sedigraphs were found to be in good agreement with the observed ones, showing the efficiency of the model when applied to convergent and divergent surfaces under controlled laboratory conditions.

6.2. Introduction

Rainfall induced soil erosion is a serious environmental threat, responsible for the arable lands' fertility reduction, crop yield depression, surface runoff intensification and harmful pollutants transportation to the freshwater bodies. Therefore, soil conservation is vital for sustainable agriculture, which involves estimation of soil loss and identification of critical areas for implementation of soil conservation measures.

Mathematical models are cost-effective tools to understand soil erosion, evaluate different soil and water conservation practices in different climatic conditions and assist developing policies for future climate scenarios. However, there is not a universal model that can accurately describe and predict soil erosion at all temporal and spatial scales. The focus of this study is a physically based process model that uses mass conservation equations to describe the sediments detachment, transportation, and deposition processes (e.g. Lopes, 1987; Smith et al., 1995).

The kinematic wave (KW) theory has been a widely accepted technique for modelling overland flow. One-dimensional (1D) KW approximations have been applied and found to be satisfactory on small slopes (e.g. de Lima and Singh, 2002; Isidoro and de Lima, 2013; Singh and de Lima, 2018).

Sediment transport data are required to test the skills of many soil erosion models. Such data in the consideration of different factors such as rainfall characteristics, slope geometry, soil characteristics, land cover, etc, can be obtained from field plots and laboratory soil flumes. Numerous researchers had evaluated their physically based soil erosion and transport models in controlled laboratory conditions, mostly focussing on the square or rectangular plane soil surface geometries (e.g. Liu et al., 2006; Deng et al., 2008; An and Liu, 2009; Arguelles et al., 2014; Abrantes et al., 2021). However, soil surface geometry found in nature is complex. Several researchers (e.g. Rieke-Zapp and Nearing, 2005; de Lima et al., 2018; Mujtaba et al., 2019) studied in the laboratory the soil erosion response on different surface profile curvatures (convex, plane and concave) of converging, diverging and plane shaped soil surfaces. To our knowledge, no physically based 1D model has been proposed that can estimate rainfall induced soil erosion on converging and diverging surfaces.

The objective of this paper was to develop a 1D cascade model for estimating rainfall induced runoff and soil erosion on converging and diverging plane surfaces and test it based on controlled laboratory experiments that used a soil flume and a rainfall simulator.

6.3. Proposed cascade model

Soil erosion is a complex phenomenon that might be affected by the soil surfaces' geometry/geomorphology. The presented 1D cascade model for estimating rainfall induced runoff and soil erosion represents the soil surface geometry as a cascade of rectangular planes. It has three components i.e. (i) Horton's equation for soil infiltration computation; (ii) the KW approximation of the 1D Saint-Venant shallow water equations for overland flow generation; and (iii) 1D sediment transport equation for soil loss calculation.

6.3.1. Infiltration model

Horton (1933, 1938, 1941) introduced an exponential decay equation to describe the infiltration rate variation with time after a soil surface is exposed to constant rainfall as:

$$f_c(t) = f_1 + (f_0 - f_1)e^{-kt} \qquad 6.1)$$

where, $f_c(t)$ is the infiltration rate at any time t, f_0 is the initial infiltration rate when rainfall starts (at t=0), f_1 is the final or equilibrium infiltration rate and k is the exponential time decay coefficient. Cumulative infiltration F at any time t is:

$$F = \int_0^t f_c(t)dt = f_1 t + \frac{(f_0 - f_1)}{k}\,(1 - e^{-kt}) \qquad 6.2)$$

Using Equation 6.1 to eliminate t in Equation 6.2, the resultant equation becomes:

$$F = \frac{f_0 - f_c}{k} - \frac{f_1}{k}\ln\left(\frac{f_c - f_1}{f_0 - f_1}\right) \qquad 6.3)$$

Prior to ponding, cumulative infiltration is $F = It$, where I is the mean rainfall intensity. Ponding occurs when infiltration rate equals to the rainfall intensity I. Making $f_c = I$ in Equation 6.3, one gets:

$$F_p = \frac{f_0 - I}{k} - \frac{f_1}{k}\ln\left(\frac{I - f_1}{f_0 - f_1}\right) \qquad 6.4)$$

where, F_p is the cumulative infiltration at ponding time t_p, which is:

$$t_p = \frac{F_p}{I} = \frac{f_0 - I}{kI} - \frac{f_1}{kI}\ln\left(\frac{I - f_1}{f_0 - f_1}\right) \qquad 6.5)$$

6.3.2. Overland flow model

Overland flow on any given plane is described by the KW estimate of the 1D Saint-Venant equation (Singh, 1996):

$$\frac{\partial h}{\partial t} + \frac{1}{W}\frac{\partial Q}{\partial x} = r \qquad 6.6)$$

where, h is water depth, W is runoff width, Q is runoff discharge, r is rainfall excess intensity, t is time and x is distance in the flow direction.

KW equation assumes that friction slope equals to bed slope; so, by using existing open channel flow equations, a relationship between discharge Q and water depth h at any point on a plane can be expressed as:

$$Q = \alpha W h^{\beta} \tag*{6.7)}$$

where, α is the KW resistance parameter and β is the Bakhmeteff dimensionless coefficient assumed equal to 5/3. Parameter α is related to Manning roughness coefficient n and can be calculated as $\alpha = n\,S^{1/2}$, where S is the bed slope of a plane.

By substituting Equation 6.7 in Equation 6.6, the KW equation can be rewritten as:

$$\frac{\partial h}{\partial t} + \beta\alpha h^{\beta-1}\frac{\partial h}{\partial x} = r \tag*{6.8)}$$

A cascade of rectangular n-planes that represents converging or diverging surfaces exposed to rainfall is shown in Fig. 6.1. Conceptually, these n-planes could vary in their lengths, widths, and slope. Here, the numerical scheme for overland flow computation is described for the converging cascade planes, as an example. The governing equation for overland flow is derived (Equation 6.8) using the second-order single-step Lax–Wendroff numerical scheme, expressed in finite difference form as (Singh, 1996):

$$h_j^{i+1} = h_j^i + \Delta t\left(r_j^i - \beta\alpha\frac{h_{j+1}^{i\beta-1}+h_{j-1}^{i\beta-1}}{2}\frac{h_{j+1}^i-h_{j-1}^i}{2\Delta x}\right) + \frac{(\Delta t)^2}{2}\frac{r_j^{i+1}-r_j^i}{\Delta t} - \beta\alpha\frac{(\Delta t)^2}{2\Delta x}\left[\frac{h_{j+1}^{i\beta-1}+h_j^{i\beta-1}}{2}\left(\frac{r_{j+1}^i+r_j^i}{2} - \beta\alpha\frac{h_{j+1}^{i\beta-1}+h_j^{i\beta-1}}{2}\frac{h_{j+1}^i-h_j^i}{\Delta x}\right) - \frac{h_j^{i\beta-1}+h_{j-1}^{i\beta-1}}{2}\left(\frac{r_j^i+r_{j-1}^i}{2} - \beta\alpha\frac{h_j^{i\beta-1}+h_{j-1}^{i\beta-1}}{2}\frac{h_j^i-h_{j-1}^i}{\Delta x}\right)\right] \tag*{6.9)}$$

where, i and j represents the grid points in time and space, respectively.

For the downstream boundary of each plane, the following first order scheme is used (Singh, 1996):

$$h_{jL}^{i+1} = h_{jL}^i + \Delta t\left(r_{jL}^i - \beta\alpha\,\frac{h_{jL}^{i\beta-1}+h_{jL-1}^{i\beta-1}}{2}\,\frac{h_{jL}^i-h_{jL-1}^i}{\Delta x}\right) \qquad \text{for } x = L \tag*{6.10)}$$

where, h_{jL} refers to the last point in space x and L is the length of each plane along the flow direction. Initial condition of every plane is given as:

$$h(x,0) = 0 \qquad \text{for } 0 \le x \le L \tag*{6.11)}$$

Upstream boundary condition for the first plane k is given as:

$h_k(0,t) = 0$ for $0 \le t \le \infty$ 6.12)

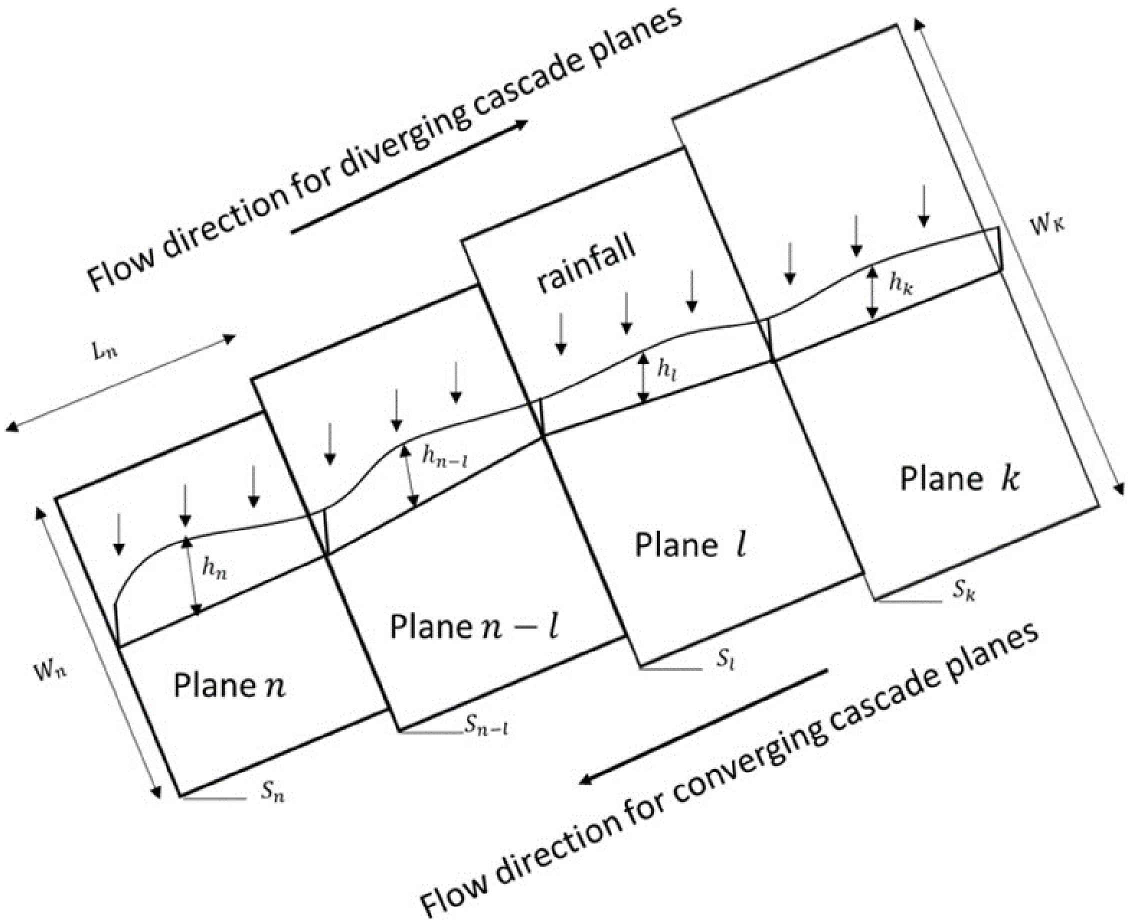

Fig. 6.1. Sketch and notation used for the cascade of n-planes that is used to represent converging (sloping to the left) or diverging (sloping to the right) cascades.

For the rest of cascade planes, the discharge leaving the downstream boundary of each plane enters the upstream boundary of next plane and serves to establish the boundary condition required for computation of the water depth of that plane. A computation of upstream boundary condition for the plane n is given as an example:

$Q_{n-l}(0,x) = \alpha_{n-l} W_{n-l} h_{n-l}^{\beta}(0,x)$ for $0 \le x \le L$ 6.13)

$h_n(0,x) = \left(\frac{Q_{n-l}}{\alpha_n W_n}\right)^{1/\beta}$ for $0 \le x \le L$ 6.14)

The numerical scheme needs to maintain the Courant number for stability, i.e.

$$\frac{\Delta t}{\Delta x} < \frac{1}{\alpha \beta h^{\beta-1}(x,t)} \qquad 6.15)$$

6.3.3. Soil erosion model

The rainfall induced soil erosion involves the processes of sediment detachment, transportation and deposition (Foster, 1982). Sediment detachment and transportation can occur by the impact of rainfall drops and shear stress of overland flow, known as interrill and rill erosion. The deposition process reflects the settling down of eroded sediments. These processes are defined in the 1D continuity equation of sediment transport (Bennett, 1974; Foster, 1982):

$$\frac{\partial ch}{\partial t} + \frac{\partial cq}{\partial x} = e_R - d + e_I \qquad 6.16)$$

where, h is water depth, q is discharge per unit width, c is sediment concentration in overland flow, e_R is rill erosion rate, d is sediment deposition rate and e_I is interrill erosion rate, t is time and x is distance in the flow direction. Parameter e_I is (Lane and Shirley, 1985):

$$e_I = K_I \, I \, r \qquad 6.17)$$

where, K_I is the interrill coefficient, I is rainfall intensity and r is rainfall excess intensity. Rill erosion occurs when sediments are unable to resist the shear stress of overland flow and its rate can be expressed as (Croley, 1982; Foster, 1982):

$$e_R = K_R \, \tau_e^b \qquad 6.18)$$

where, K_R is a soil detachability factor for shear stress, τ_e is the average "effective" shear stress assuming broad shallow flow, and b is an exponent in the range 1.0 to 2.0.

Deposition rate d is expressed as (Mehta, 1983):

$$d = \in c \, V_s \qquad 6.19)$$

where, $\in$ is a dimensionless coefficient depending on soil and fluid properties, c is sediment concentration in overland flow and V_s is the settling velocity of sediment particle that can be expressed as:

$$V_s = W_o \sqrt{\frac{(\gamma_s - \gamma)}{\gamma} g d_s} \qquad 6.20)$$

with

$$W_o = \sqrt{\frac{2}{3} + \frac{36\nu^2}{g\,d_s^3\left(\frac{\gamma_S}{\gamma}-1\right)}} - \sqrt{\frac{36\nu^2}{g\,d_s^3\left(\frac{\gamma_S}{\gamma}-1\right)}} \qquad 6.21)$$

where, γ_s and γ is specific weight of sediment and water, respectively, ν is kinematic viscosity of water, g is acceleration due to gravity and d_s is size of settling sediment.

The numerical procedure proposed to solve the sediment continuity equation (Equation 6.16) uses the four point-implicit scheme (Lopes and Lane 1988):

$$\frac{\phi}{\Delta t}\left[(ch)_{j+1}^{i+1} - (ch)_{j+1}^{i}\right] + \frac{1-\phi}{\Delta t}\left[(ch)_{j}^{i+1} - (ch)_{j}^{i}\right] + \frac{\omega}{\Delta x}\left[(cq)_{j+1}^{i+1} - (cq)_{j}^{i}\right] + \frac{1-\omega}{\Delta x}\left[(ch)_{j+1}^{i} - (cq)_{j}^{i}\right] = \omega\left[\phi e_{R_{j+1}}^{i+1} + (1-\phi)e_{R_j}^{i+1}\right] + (1-\omega)\left[\phi e_{R_{j+1}}^{i} + (1-\phi)e_{R_j}^{i}\right] - \omega\left[\phi d_{j+1}^{i+1} + (1-\phi)\,d_j^{i+1}\right] - (1-\omega)\left[\phi d_{j+1}^{i} + (1-\phi)\,d_j^{i}\right] + \omega e_I^{i+1} + (1-\omega)\,e_I^{i} \qquad 6.22)$$

where, ϕ is the weighting factor for space and ω is the weighting factor for time. If $\phi = 1$ and $\omega = 0$, the numerical scheme becomes explicit and needs Courant number (Equation 6.15) to be maintained for stability. If $\phi = 0.5$ and $\omega > 0.5$, the scheme becomes implicit and is unconditionally stable; but, for accuracy, Courant number must be maintained. For our simulations, we used $\phi = 0.5$ and $\omega = 0.6$. This made the numerical scheme to be stable for the computation of small volumes of runoff and sediment, normally associated with laboratory conditions, which were used in this study to test the performance of the model.

Initial and upstream boundary conditions on each cascade plane are (Lopes, 1987):

$$c(x, t_p) = \frac{K_I\,I\,(t_p)\,r(t_p)}{\epsilon V_s + r(t_p)} \quad \text{for } x \geq 0 \qquad 6.23)$$

$$c(0, t) = \frac{K_I\,I\,(t)\,r(t)}{\epsilon V_s + r(t)} \quad \text{for } t \geq t_p \qquad 6.24)$$

These boundary conditions imply that the numerical scheme will start to compute sediment concentration from ponding time. The downstream boundary condition was considered open for every cascade plane.

6.4. Model testing procedure

6.4.1. Experimental data

Data for testing the model were obtained from laboratory experiments conducted on a soil flume with simulated rainfall (Fig. 6.2) under controlled conditions of intensities and fluxes. The rainfall simulator's sprinkler was equipped with a single jet nozzle installed at 2.2 m above the soil flume's surface and producing a full cone spray. This simulator was also already used in many other studies (e.g. de Lima et al., 2012; Montenegro et al., 2013; Carvalho et al., 2014; Mujtaba et al., 2019). The rainfall spatial distribution was calculated by placing rain gauges 0.15 m apart from each other on the soil flume and measuring the collected rainfall volume during a 2 min rainfall event.

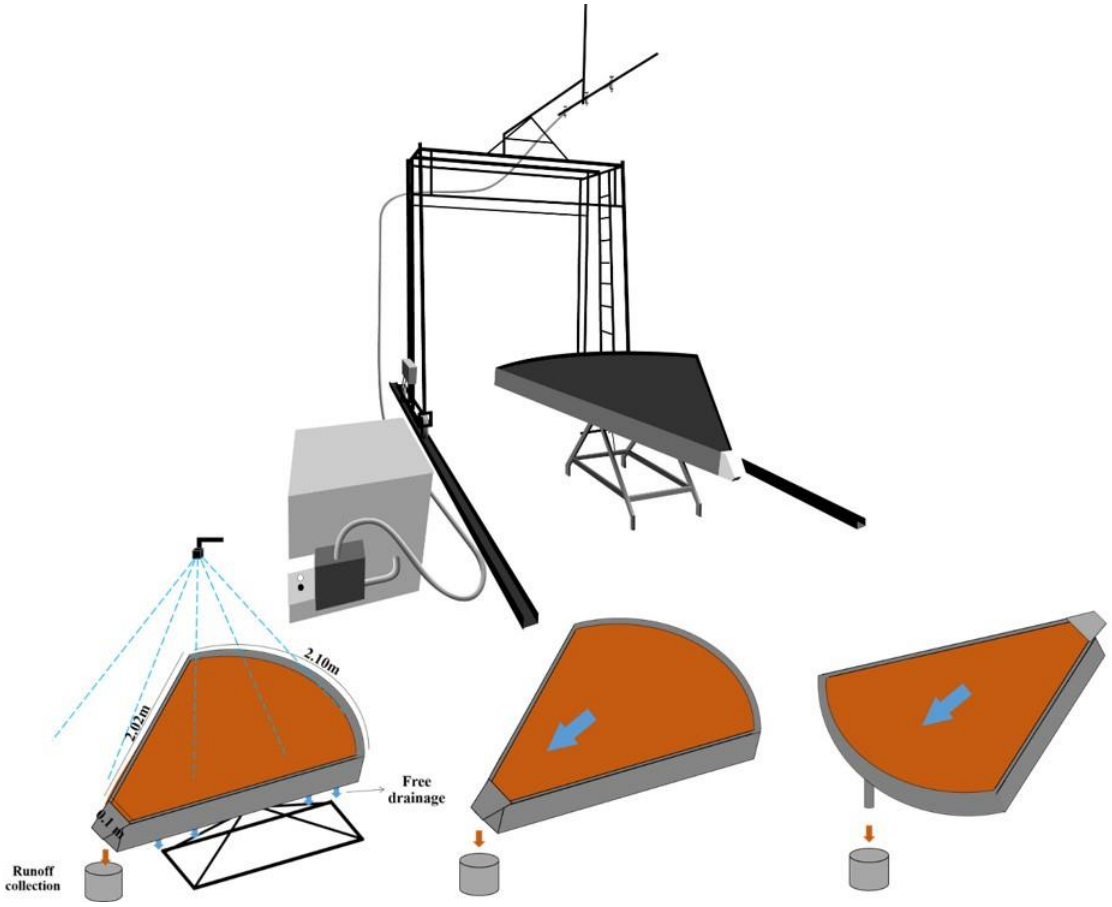

Fig. 6.2. Laboratory setup used in the experiments, comprised of a rainfall simulator and a soil flume (top and bottom-left); the flume has outlets on both ends, for the converging (bottom-middle) and the diverging surface (bottom-right) experiments.

The soil flume presents a planar circular sector geometry of 2.02 m length and limited by 0.10 m and 2.10 m arc lengths; that led to the formation of converging and diverging flow conditions. Flume's depth was 0.12 m. The flume was made of zinc-coated iron metal sheets; a geotextile rug was placed over the iron mesh at the bottom of the soil flume for free drainage. The flume had runoff collection outlets at both ends. By tilting the flume in opposite directions, the setup allowed to perform experiments on both converging and diverging plane surfaces. After sieving through a 5 mm mesh, soil (sandy loam) was spread manually in the flume, in layers, and compacted gently with a steel plate;

the soil surface was levelled using a wooden blade. The soil depth was 0.1 m. Before each experiment, soil was saturated gently until ponding occurred. The experiment was conducted after letting the soil to drain for 1.5 h, assuring soil moisture at approximately field capacity at the beginning of each run. The soil was removed after each experiment ended and was replaced by air dried soil. Soil saturation procedure was repeated for each experiment.

A total of four experiments i.e. two on converging and two on diverging plane surfaces were done. The corresponding data on the applied mean rainfall intensity and slope of the converging and diverging plane surfaces are given in Table 6.1. Rainfall duration for each experiment was 7 min. Higher rainfall intensity and steep gradient ensured high soil erosion prone conditions and lower rainfall intensity associated with gentle gradient guaranteed low soil loss conditions on both surface geometries. This was done to check the model’s capability to simulate these two diverse erosion situations.

Table 6.1. Manually optimized infiltration and soil erosion parameters used in numerical simulations that were fitted to the observed hydrographs and sedigraphs.

Exp.	Soil surface	Rain intensity (mm h^{-1})	Slope (%)	Infiltration parameters			Soil erosion parameters	
				f_0 (m s^{-1})	f_1 (m s^{-1})	k	K_I (kg s m^{-4}) (×10^7)	K_R (kg m N$^{-1.5}$ s^{-1})
1	Conv.	66.1	20	2.5×10^{-5}	3.0×10^{-6}	0.060	1.2	0.52
2	plane	37.4	5	1.25×10^{-5}	3.5×10^{-6}	0.009	1.5	0.8
3	Div.	65.8	20	0.50×10^{-5}	5.5×10^{-6}	0.030	15	0.45
4	plane	37.3	5	1.34×10^{-5}	4.0×10^{-6}	0.007	1.5	3.12

Runoff samples were collected at the outlet of the flume for 10 sec at 1 min intervals, from initiation of runoff until the end of rainfall (7 min). Two more samples were collected at 10 sec intervals after rainfall stopped. The runoff samples were weighted, oven dried at 80°C for 24 h and weighted again to estimate runoff and soil loss.

6.4.2. Numerical simulation criteria

For numerical simulations, the surface was represented by a cascade of four planes (Fig. 6.3), with an area of 2.2 m^2, which was approximately equal to the surface area of the soil flume (2.24 m^2). Each plane had constant length L of 0.5 m along the flow direction. Variation was in widths W of the planes. For a given cascade (converging or diverging), all planes had similar slope. Since the rainfall spatial distribution over the flume was not uniform, the rainfall distribution simulated on the cascade planes was also not even (Fig. 6.4).

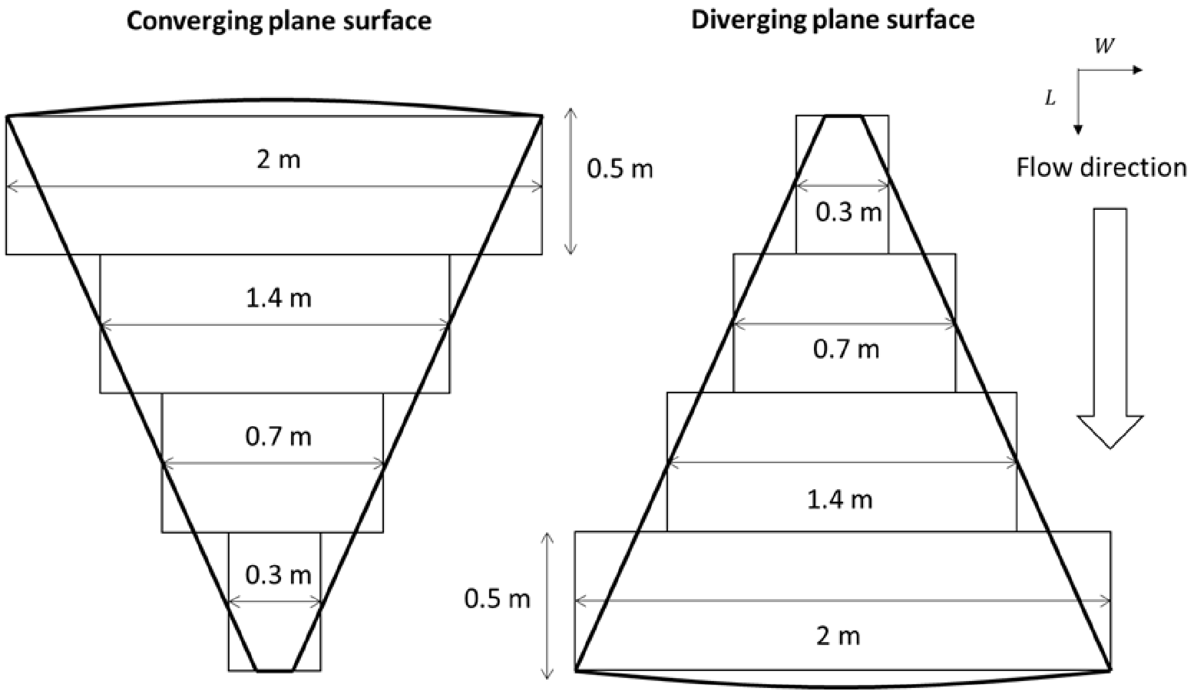

Fig. 6.3. Schematic sketch illustrating the approximate representation of the soil flume surface planar geometry by converging and diverging cascade planes of equal length L, of 0.5 m. Width W of each plane is also given.

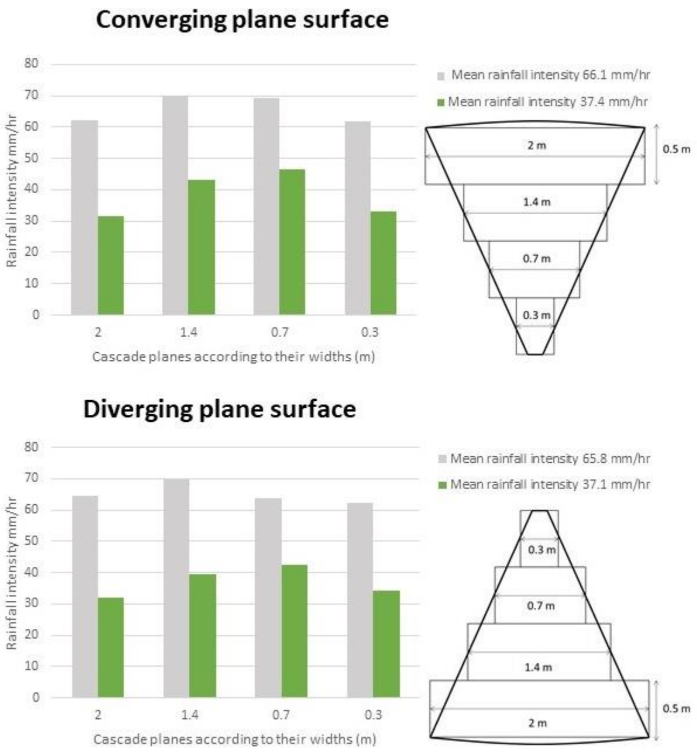

Fig. 6.4. Variation of mean rainfall intensity on the planes of the converging and diverging cascades, which simulate the soil surface geometry of the flumes.

The infiltration and soil erosion parameters for each numerical simulation that were optimized by trial and error to fit the observed hydrographs and sedigraphs are listed in Table 6.1. The rest of soil erosion parameters were constant for every simulation and are listed in Table 6.2; this can be justified because some are physical data and some did not affect much the model results.

Table 6.2. Soil erosion parameters that were constant for all numerical simulations.

Parameter	value	units
b	1.5	-
$\in$	0.5	-
γ_s	15650	N/m^3
γ	9980	N/m^3
d_s	0.0004	m
ν	1.3x10^{-6}	m^2/s

6.5. Model evaluation

The skill of the model in simulating runoff peak, total runoff volume, soil loss peak and total sediment mass was assessed using the Percentage of Deviation, $Dev(\%)$:

$$Dev(\%) = \frac{Sim-Obs}{Obs} \times 100 \qquad 6.25)$$

where Obs and Sim represent the observed and simulated data, respectively.

The goodness of fit of the shape of the hydrographs and sedigraphs was evaluated using the Nash-Sutcliffe coefficient of efficiency (NS):

$$NS = 1 - \frac{\sum_{t=1}^{n}(Obs_t-Sim_t)^2}{\sum_{t=1}^{n}(Obs_t-Obs^m)^2} \qquad 6.26)$$

where Obs_t and Sim_t represent the observed and simulated data at time t, Obs^m is mean observed data and n is the total number of data points (n=9, in our experiments). The range of NS values lies from -∞ to 1. As the NS value approaches 1, the model's prediction efficiency gets better. If the NS value is 1, the model's predicted values are the perfect fit to observed data.

6.6. Results

Simulated and observed hydrographs and sedigraphs for different rainfall intensity and slope combinations on converging and diverging plane surfaces are presented in Figs. 6.5 and 6.6. The numerical model's simulated hydrographs had good adjustment with the observed ones, also suggested by the NS values close to 1 (Fig. 6.5). Simulated hydrographs' rising limbs fitted well to the corresponding observed values. However, delay response was seen in the simulated hydrographs' recession limbs.

Overall, the presented model was capable to reproduce the main characteristics of sediment transport: all the simulated sedigraphs had good comparison with the observed ones. This was also suggested by NS values always higher than 0.7 (Fig. 6.6). However, the cascade model revealed better capability to simulate runoff rates than the soil loss rates.

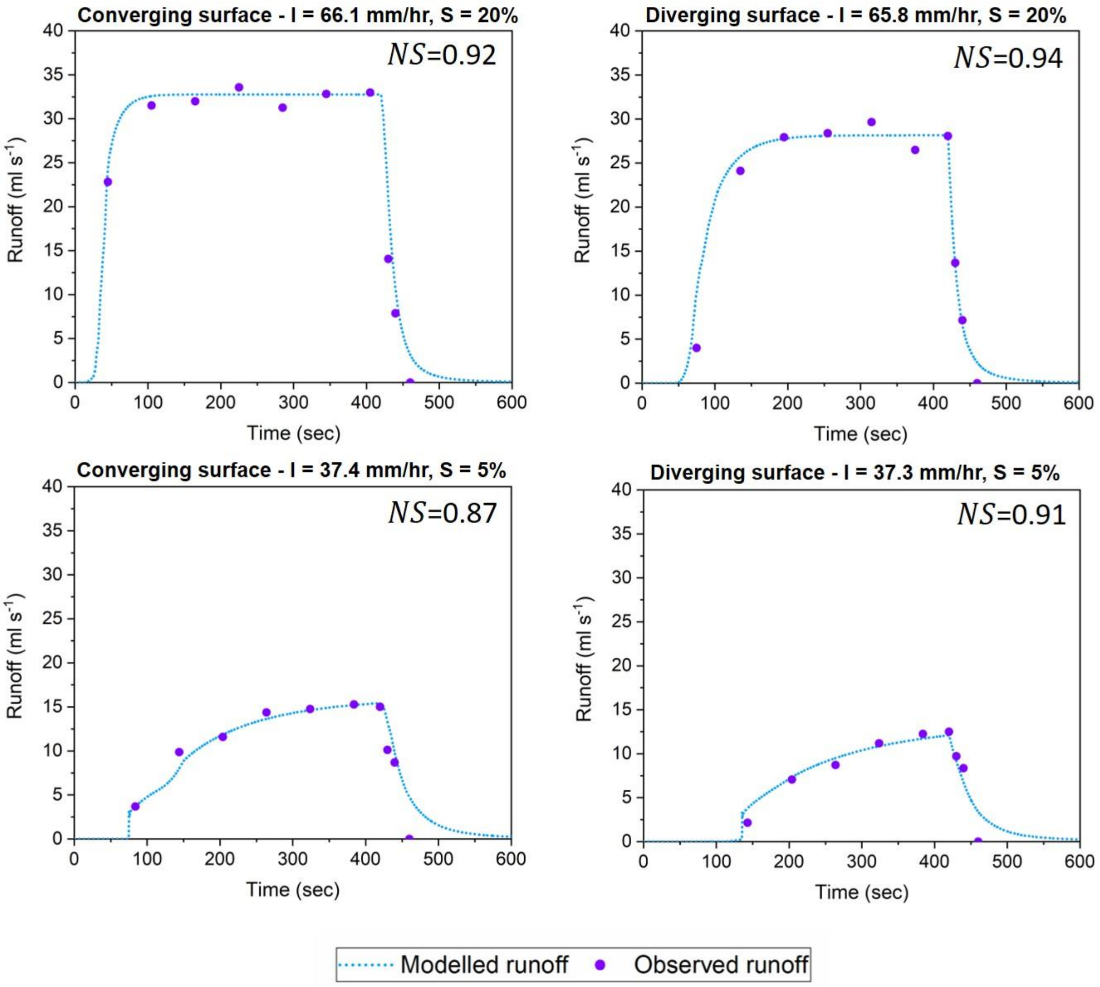

Fig. 6.5. Observed and simulated hydrographs on converging and diverging surfaces for different combinations of rainfall and slope. Nash-Sutcliffe coefficients are also given.

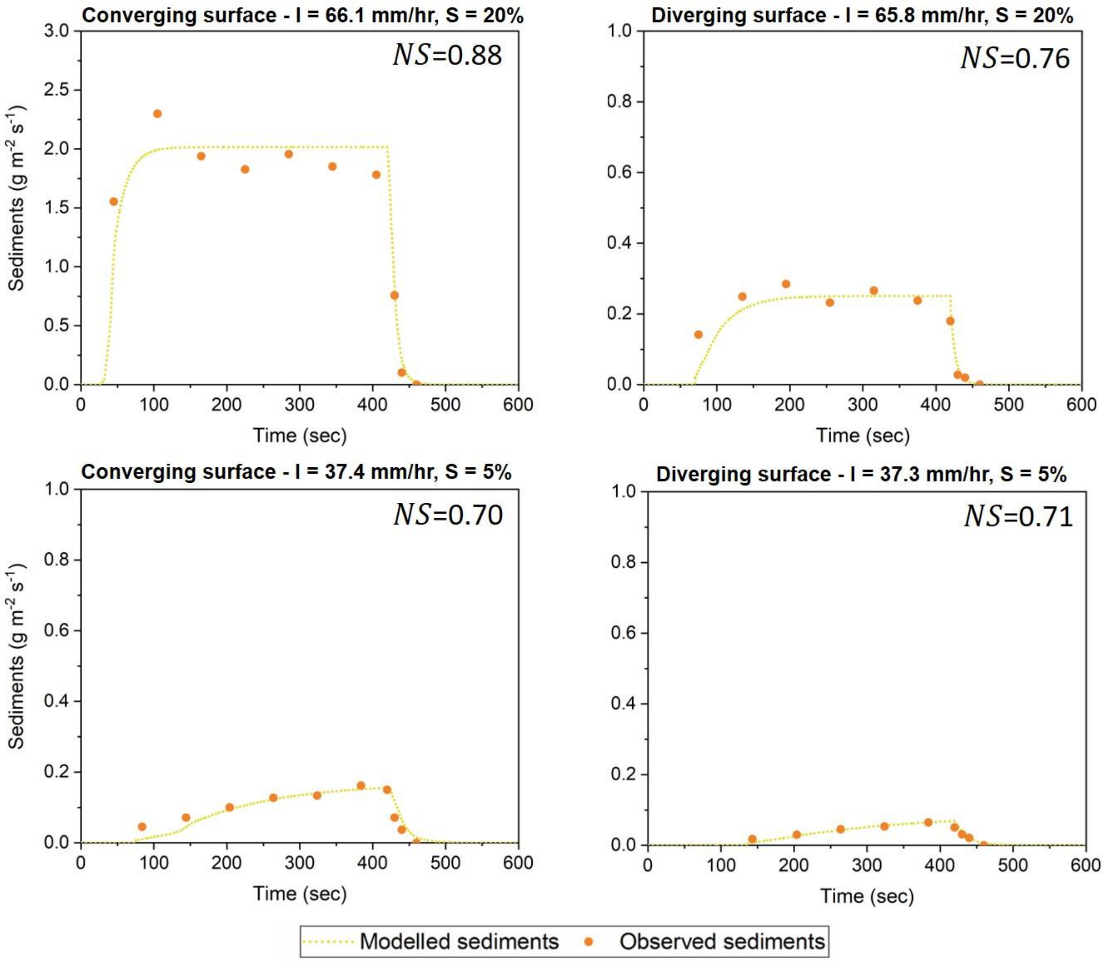

Fig. 6.6. Observed and simulated sedigraphs on converging and diverging surfaces for different combinations of rainfall and slope. Note that the left top figure has different Y-axis scale. Nash-Sutcliffe coefficients are also given.

The simulated and observed runoff peaks, runoff volumes, soil loss peaks and total soil losses along with the corresponding $Dev(\%)$ values are given in Tables 6.3 and 6.4, showing that model performed reasonably well. However, there were two cases (total runoff in experiment 4 and total soil loss in experiment 2) where $Dev(\%)$ values were higher, both for lower rainfall intensity and gentle slope, corresponding to low runoff volumes and sediment transport yield.

Table 6.3. Observed and simulated runoff peak and volumes for all experiments on converging and diverging surfaces; Percentage of Deviation $Dev(\%)$ is also presented.

Exp.	Soil surface	Rain intensity (mm h^{-1})	Slope (%)	Data	Runoff peak (mL s^{-1})	$Dev(\%)$	Total runoff volume (L)	$Dev(\%)$
1	Conv. plane	66.1	20	Obs.	32.97	-0.64	10.42	0.61
				Sim.	32.76		10.48	
2		37.4	5	Obs.	15.28	0.96	2.48	-12.22
				Sim.	15.43		2.17	
3	Div. plane	65.8	20	Obs.	29.66	-5.05	7.50	8.18
				Sim.	28.16		8.12	
4		37.3	5	Obs.	12.49	-3.20	0.89	49.56
				Sim.	12.09		1.32	

Table 6.4. Observed and simulated soil loss peak and total soil loss for all experiments on converging and diverging surfaces; Percentage of Deviation $Dev(\%)$ is also presented.

Exp.	Soil surface	Rain intensity (mm h^{-1})	Slope (%)	Data	Soil loss peak (g m^2 s^{-1})	$Dev(\%)$	Total soil loss (g)	Dev (%)
1	Conv. plane	66.1	20	Obs.	2.30	-12.31	1598.14	0.83
				Sim.	2.02		1611.48	
2		37.4	5	Obs.	0.16	-3.82	70.59	-27.66
				Sim.	0.16		51.06	
3	Div. plane	65.8	20	Obs.	0.27	-5.66	179.93	-3.37
				Sim.	0.25		173.87	
4		37.3	5	Obs.	0.06	6.85	19.12	-3.70
				Sim.	0.07		18.41	

In our study, the numerical model was tested with observed data (only one-time events, no replicates). Therefore, experimental errors (soil preparation, rainfall simulator handling and runoff sampling) cannot be ruled out in these runs. Future work should consider different conditions (for example, rainfall intensities, slopes, surface shapes and dimensions, soil types) in order to further evaluate the model skills. Also, larger number of observed simulations should be tested.

6.7. Conclusions

A 1D cascade model for the estimation of rainfall induced runoff and soil erosion on two soil surface geometries (converging plane and diverging plane) was proposed and tested using a soil flume and a rainfall simulator. A total of four experiments, two on each surface for different combinations of slope and rainfall intensity, were conducted to verify the model's capabilities. Overall, the simulated hydrographs and sedigraphs compared well with the observed ones, as suggested by the Nash-Sutcliffe coefficients of efficiency (NS). However, the model's ability to simulate the observed hydrographs ($NS > 0.87$) was better than to simulate the sedigraphs ($NS > 0.70$).

The concept of using cascades in the presented model accommodates the spatial changes in soil surface geometry. However, when flow moves from one cascade to another one, it abruptly changes (shock wave phenomenon) due to change in cascade geometry; this might affect the shape of hydrographs. Therefore, the number of cascade planes used for any specific study area needs to be increased until abrupt oscillations are diminished.

The presented model is thought to be a useful step towards simulating overland flow generation and sediment transport in convergent and divergent plane surfaces, and it avoids the use of more complex 2D models. Future studies should evaluate the capability of this model to simulate runoff and sediment loss processes on different curvatures (convex and concave) of different soil surface shapes (converging, linear and diverging) under different rainfall intensities, soil types and slopes.

7. Conclusions and Final Remarks

This thesis is in Civil Engineering, in the specific area of Hydraulics, Water Resources and Environment, and focuses namely on surface-subsurface hydrological processes and their impact on rock fragments. Although, specific conclusions are presented in previous chapters (3 to 6), the first part of this final remarks summarizes briefly the overall conclusions drawn in the thesis. The second part presents some suggestions for future research.

7.1. Conclusions

This doctoral thesis was focused on two main objectives. The first one was to create further understanding of rock fragments impact on surface-subsurface hydrological processes at plot and hillslope catchment scales. Second one dealt with the development of innovative shallow flow velocity measuring techniques and mathematical models related to rainfall-induced soil erosion processes. Following are the general conclusions drawn according to the objectives listed in Chapter 1:

i. To evaluate the influence of different distribution patterns of rock fragment surface cover and soil surface geometry on runoff and soil loss through laboratory experiments.

Laboratory experiments under simulated rainfall were conducted on three different distribution patterns of rock fragment covers placed on the surface of two soil surface geometries (converging plane and diverging plane). For the same rainfall input, rock fragment cover percentage and slope gradient, all rock fragment distribution patterns increased the runoff and soil loss with respect to bare (rock free) soil surface, on both converging and diverging surfaces. However, total soil loss of all experiments conducted on converging surfaces was much higher than on diverging surfaces. This was due to much higher unit stream power at the downstream end of the flume for all scenarios on converging surfaces than that on diverging surfaces. This explained the suggestion given in Chapter 3 that the understudied soil surface geometries played a more influential role on soil erosion than different distribution patterns of specific percentage of rock fragment surface cover.

ii. To study the role of stony soils in runoff response of a small mountain catchment through numerical simulations.

The simulated subsurface runoff response from stony soils was compared with observed surface runoff response at mountainous catchment's outlet in Chapter 4. This was done to explore the central idea that reduced water retention of stony soils can have similar effect on catchment runoff formation as the commonly accepted and more often studied preferential flow. Soil hydraulic parameters applied in Hydrus-2D single porosity model for soil water response simulations were obtained by the Representative Elementary Volume (REV) approach and by the inverse modelling (IM) with Hydrus-1D model. The REV approach to derive soil hydraulic parameters was more suitable for subsurface runoff modelling in stony soils than the IM approach.

iii. To test the capabilities of a new thermal tracer for velocity estimation of shallow overland flows.

In Chapter 5, a new particle thermal tracer (cold oil droplets) using infrared-based particle tracking velocimetry (PTV) technique was compared with dye tracing and the conventional PTV technique (polystyrene beads as tracer and optical video camera) to measure velocities of shallow overland flows (< 2mm depth) under controlled laboratory conditions without rainfall. The results suggested that the infrared-based and conventional PTV techniques were more reliable for estimating the mean velocity of shallow overland flows than the dye tracing technique. The infrared-based PTV technique showed some advantages over conventional PTV and dye tracing techniques due to its tracer's prominent visibility and independency from lighting conditions. The visibility of oil droplets' plumes by the infrared camera was clearer than the leading edge of the dye tracer by the optical camera. The conventional PTV technique required significant illumination of its tracer relative to background and is more affected by light reflection. The infrared-based PTV technique was not affected by the lighting conditions since, the visibility of the oil droplet tracer was only dependent on the temperature difference of the water and oil droplet. Furthermore, polystyrene beads tracer was unable to propagate properly on low discharges and the consequent lower flow depths. In our study, this resulted in the underestimation of mean velocities at low discharges by the conventional PTV. The infrared-based PTV technique tracer did not encounter this problem.

iv. To develop a one-dimensional rainfall induced soil erosion numerical model based on cascade plane theory.

A one-dimensional cascade model for the estimation of rainfall induced runoff and soil erosion on converging and diverging surfaces is developed in Chapter 6. The model has three components i.e., (i) Horton's equation for soil infiltration computation; (ii) the kinematic wave approximation of the one-dimensional Saint-Venant shallow water equations for overland flow generation; and (iii) one-dimensional sediment transport equation for soil loss calculation. The model's simulations were validated by the measured data collected in controlled laboratory conditions. Overall, the simulated hydrographs and sedigraphs had good comparison with the observed ones. However, the model's ability to simulate the observed runoff hydrographs was better than to simulate the sedigraphs. The model's calibration procedure can be difficult and time consuming as it relies on a 'classical' trial and error method for parameters optimization.

7.2. Future Work

Future research could include:

- Investigate the runoff and soil loss response on different curvatures (convex and concave) of different soil surface shapes (converging, linear and diverging) and for different types of soil in the presence of different distribution patterns and percentages of rock fragment cover (on or embedded in soil);
- Test the capabilities of Representative Elementary Volume approach, described in this thesis, to simulate soil water response in stony soils under different initial soil moisture conditions, soil characteristics, rainfall intensities and slope angles;
- Test the capacity of the proposed thermal tracer (cold oil droplets) using infrared-based particle tracking velocimetry (PTV) technique to measure velocities of rainfall-induced shallow overland flows in field and laboratory conditions;
- Evaluate the performance of the cascade model presented in this thesis to simulate runoff and sediment loss on different curvatures (convex and concave) of different soil surface shapes (converging, linear and diverging) under different rainfall intensities, soil types and slopes;
- Apply the automatic solution of parameters optimization for the calibration of the cascade model presented in this thesis to simulate runoff and sediment loss processes.

8. References

Abban, B.K.B., Papanicolaou, A.N. (Thanos), Giannopoulos, C.P., Dermisis, D.C., Wacha, K.M., Wilson, C.G., Elhakeem, M., 2017. Quantifying the changes of soil surface microroughness due to rainfall impact on a smooth surface. Nonlinear Process. Geophys. 24, 569–579. https://doi.org/10.5194/npg-24-569-2017

Abrahams, A.D., Parsons, A.J., Luk, S.-H.S. -H, 1986. Field measurement of the velocity of overland flow using dye tracing. Earth Surf. Process. Landforms 11, 653–657. https://doi.org/10.1002/esp.3290110608

Abrahams, A.D., Atkinson, J.F., 1993. Relation between grain velocity and sediment concentration in overland flow. Water Resour. Res. 29 (9), 3021-3028. https://doi.org/10.1029/93WR00771

Abrantes, J.R.C.B., Moruzzi, R.B., de Lima, J.L.M.P., Silveira, A., Montenegro, A.A.A., 2019. Combining a thermal tracer with a transport model to estimate shallow flow velocities. Phys. Chem. Earth 109, 59–69. https://doi.org/10.1016/j.pce.2018.12.005

Abrantes, J.R.C.B., Moruzzi, R.B., Silveira, A., de Lima, J.L.M.P., 2018a. Comparison of thermal, salt and dye tracing to estimate shallow flow velocities: Novel triple-tracer approach. J. Hydrol. 557, 362–377. https://doi.org/10.1016/j.jhydrol.2017.12.048

Abrantes, J.R.C.B., Prats, S.A., Keizer, J.J., de Lima, J.L.M.P., 2018b. Effectiveness of the application of rice straw mulching strips in reducing runoff and soil loss: Laboratory soil flume experiments under simulated rainfall. Soil Tillage Res. 180, 238–249. https://doi.org/10.1016/j.still.2018.03.015

Abrantes J.R.C.B., Simões N.E., de Lima J.L.M.P., Montenegro A.A.A., 2021. Two-dimensional (2D) numerical modelling of rainfall induced overland flow, infiltration and soil erosion: comparison with laboratory rainfall-runoff simulations on a two-directional slope soil flume. J. Hydrol. Hydromechanics 69, 140-150. https://doi.org/10.2478/johh-2021-0003

Abu-Zreig, M.M., Tamimi, A., Alazba, A.A., 2011. Soil Erosion Control and Moisture Conservation of Arid Lands with Rock fragment Cover. Arid Land Res. Manag., 25 (3), 294-307. https://doi.org/10.1080/15324982.2011.565859

Adekalu, K.O., Olorunfemi, I.A., Osunbitan, J.A., 2007. Grass mulching effect on infiltration, surface runoff and soil loss of three agricultural soils in Nigeria. Bioresour. Technol. 98, 912–917. https://doi.org/10.1016/j.biortech.2006.02.044

Agiralioglu, N., 1985. A comparison of water lag times for converging and plane surfaces. Nord. Hydrol. 16, 169–176.

Ahn, S., Doerr, S.H., Douglas, P., Bryant, R., Hamlett, C.A.E., McHale, G., Newton, M.I., Shirtcliffe, N.J., 2013. Effects of hydrophobicity on splash erosion of model soil particles by a single water drop impact. Earth Surf. Process. Landforms 38, 1225–1233. https://doi.org/10.1002/esp.3364

Aickin, M., Gensler, M., 1996. Adjusting for multiple testing when reporting research results: the Bonferroni vs Holm methods. Am. J. Public. Health. 86, 726–728. https://doi.org/10.2105/ajph.86.5.726

Aksoy H., Kavvas, M.L., 2005. A review of hillslope and watershed scale erosion and sediment transport models. Catena 64, 247–271. https://doi.org/10.1016/j.catena.2005.08.008

Al-Qinna, M., Scott, H.D., Brye, K.R., Brahana, J.V., Sauer, T.J., Sharpley, A., 2014. Coarse fragments affect soil properties in a mantled-karst landscape of the Ozark Highlands. Soil Sci. 179, 42–50. https://doi.org/10.1097/SS.0000000000000034

An Y., Liu Q.Q., 2009. Two-dimensional hillslope scale soil erosion model. J. Hydrol. Eng. 14, 690–697. https://doi.org/10.1061/(ASCE)HE.1943-5584.0000032

Angulo-Martínez, M., Beguería, S., Kyselý, J., 2016. Use of disdrometer data to evaluate the relationship of rainfall kinetic energy and intensity (KE-I). Sci. Total Environ. 568. https://doi.org/10.1016/j.scitotenv.2016.05.223

Angulo-Martínez, M., Beguería, S., Navas, A., Machín, J., 2012. Splash erosion under natural rainfall on three soil types in NE Spain. Geomorphology 175–176, 38–44. https://doi.org/10.1016/j.geomorph.2012.06.016

Arguelles A.C.C., Jung M., Mallari K.J.B, Pak G., Aksoy H., Kavvas L.M., Eris E., Yoon J., Lee Y., Hong S., 2014. Evaluation of an erosion-sediment transport model for a hillslope using laboratory flume data. J. Arid Land 6, 647–655. https://doi.org/10.1007/s40333-014-0066-9

Arnold, J., Williams JR, N.A., 1991. SWRRB; a basin scale simulation model for soil and water resources management. cabdirect.org 20.

Bachmair, S., Weiler, M. 2011. New Dimensions of Hillslope Hydrology, in: Levia, D.F., (Eds), Forest Hydrology and Biogeochemistry. Synthesis of Past Research and Future Directions. Ecological Studies, Springer, pp. 455-482.

Barthlott, W., Mail, M., Bhushan, B., Koch, K., 2017. Plant surfaces: Structures and functions for biomimetic innovations. Nano-Micro Lett. https://doi.org/10.1007/s40820-016-0125-1

Bass, H.G., 1971. Introduction to Engineering Measurements, McGraw-Hill Educ. USA.

Bauer, S.W., 1974. A modified horton equation for infiltration during intermittent rainfall. Hydrol. Sci. Bull. 19, 219–225. https://doi.org/10.1080/02626667409493900

Bauer, T., Strauss, P., Grims, M., Kamptner, E., Mansberger, R., Spiegel, H., 2015. Long-term agricultural management effects on surface roughness and consolidation of soils. Soil Tillage Res. 151, 28–38. https://doi.org/10.1016/j.still.2015.01.017

Beguería, S., Angulo-Martínez, M., Gaspar, L., Navas, A., 2015. Detachment of soil organic carbon by rainfall splash: Experimental assessment on three agricultural soils of Spain. Geoderma 245–246, 21–30. https://doi.org/10.1016/j.geoderma.2015.01.010

Beibei, Z., Ming'an, S., Hongbo, S., 2009. Effects of rock fragments on water movement and solute transport in a Loess Plateau soil. Comptes Rendus - Geosci. 341, 462–472. https://doi.org/10.1016/j.crte.2009.03.009

Bennett, J.P., 1974. Concepts of mathematical modeling of sediment yield. Water Resour. Res. 10. https://doi.org/10.1029/WR010i003p00485

Bentley, W.A., 1904. STUDIES OF RAINDROPS AND RAINDROP PHENOMENA. Mon. Weather Rev. 32, 450–456. https://doi.org/10.1175/15200493(1904)32<450:sorarp>2.0.co;2

Beven, K., Germann, P., 1982. Macropores and water flow in soils. Water Resour. Res. https://doi.org/10.1029/WR018i005p01311

Bhatt, R., Khera, K.L., 2006. Effect of tillage and mode of straw mulch application on soil erosion in the submontaneous tract of Punjab, India. Soil Tillage Res. 88, 107–115. https://doi.org/10.1016/j.still.2005.05.004

Biddoccu, M., Guzmán, G., Capello, G., Thielke, T., Strauss, P., Winter, S., Zaller, J.G., Nicolai, A., Cluzeau, D., Popescu, D., Bunea, C., Hoble, A., Cavallo, E., Gómez, J.A., 2020. Evaluation of soil erosion risk and identification of soil cover and management factor (C) for RUSLE in European vineyards with different soil management. Int. Soil Water Conserv. Res. https://doi.org/10.1016/j.iswcr.2020.07.003

Bizzi, S., Lerner, D.N., 2015. The use of stream power as an indicator of channel sensitivity to erosion and deposition processes. River Res. Appl. 31, 16-27. https://doi.org/10.1002/rra.2717

Botter, G., Rinaldo, A., 2003. Scale effect on geomorphologic and kinematic dispersion. Water Resour. Res. 39, 1286. https://doi.org/10.1029/2003WR002154

Box, J. E., 1981. The effects of surface slaty fragments on soil erosion by water. Soil Sci. Soc. Am. J., 45, 111-116. https://doi.org/10.2136/sssaj1981.03615995004500010024x

Bouwer, H., Rice, R.C., 1984. Hydraulic Properties of Stony Vadose Zones. Ground Water 22, 696–705. https://doi.org/10.1111/j.1745-6584.1984.tb01438.x

Brandão, C., Rodrigues, R., Pinto da Costa, J., 2001. Analise de fenómenos extremos – precipitações intensas em Portugal continental. Direcção dos Serviços de Recursos Hídricos, Instituto da Agua, Lisboa, 64 p.

Brevis, W., Nino, Y., Jirka, G.H., 2011. Integrating cross-correlation and relaxation algorithms for particle tracking velocimetry. Experiments in Fluids 50, 135–147. https://doi.org/10.1007/s00348-010-0907-z

Brooks, E.S., Dobre, M., Elliot, W.J., Wu, J.Q., Boll, J., 2016. Watershed-scale evaluation of the Water Erosion Prediction Project (WEPP) model in the Lake Tahoe basin. J. Hydrol. 533, 389–402. https://doi.org/10.1016/j.jhydrol.2015.12.004

Brunner, M.I, Viviroli, D., Furrer, R., Seibert, J., Favre, A.C., 2018. Identification of flood reactivity regions via the functional clustering of hydrographs. Water Resour. Res. 54(3), 1852-1867. https://doi.org/10.1002/2017WR021650

Buchter, B., Hinz, C., Flühler, H., 1994. Sample size for determination of coarse fragment content in a stony soil. Geoderma 63, 265–275. https://doi.org/10.1016/0016-

7061(94)90068-X

Bullard, J.E., Ockelford, A., Strong, C.L., Aubault, H., 2018. Impact of multi-day rainfall events on surface roughness and physical crusting of very fine soils. Geoderma 313, 181–192. https://doi.org/10.1016/j.geoderma.2017.10.038

Bunte, K., Poesen, J., 1993. Effects of rock fragment covers on erosion and transport of noncohesive sediment by shallow overland flow. Water Resour. Res. 29, 1415–1424. https://doi.org/10.1029/92WR02706

Coppola, A., Dragonetti, G., Comegna, A., Lamaddalena, N., Caushi, B., Haikal, M. A., Basile, A., 2013. Measuring and modeling water content in stony soils. Soil Till. Res. 128, 9–22. https://doi.org/10.1016/j.still.2012.10.006

Carvalho, S.C.P., de Lima, J.L.M.P., de Lima, M.I.P., 2014. Using meshes to change the characteristics of simulated rainfall produced by spray nozzles. Int. Soil Water Conserv. Res. 2, 67 - 78. https://doi.org/10.1016/S2095-6339(15)30007-1

Cawson, J.G., Nyman, P., Smith, H.G., Lane, P.N.J., Sheridan, G.J., 2016. How soil temperatures during prescribed burning affect soil water repellency, infiltration and erosion. Geoderma 278, 12–22. https://doi.org/10.1016/j.geoderma.2016.05.002

Cerdà, A., 2001. Effects of rock fragment cover on soil infiltration, interrill runoff and erosion. Eur. J. Soil Sci. 52, 59–68. https://doi.org/10.1046/j.1365-2389.2001.00354.x

Chen, L., Sela, S., Svoray, T., Assouline, S., 2016. Scale dependence of Hortonian rainfall-runoff processes in a semiarid environment. Water Resour. Res. 52, 5149–5166. https://doi.org/10.1002/2015WR018315

Chen, H., Liu, J., Zhang, W., Wang, K., 2012. Soil hydraulic properties on the steep karst hillslopes in northwest Guangxi, China. Environ. Earth Sci. 66, 371–379.

https://doi.org/10.1007/s12665-011-1246-y

Chen, S., Xie, Z., Wang, Y., Wei, X. 2, 2005. Moisture Storage Effect of Gravel Mulch with Different Grain Size on Watermelon field. J. Desert Res. 25, 433–436.

Collischonn, W., Fleischmann, A., Paiva, R.C.D., Mejia, A., 2017. Hydraulic causes for basin hydrograph skewness. Water Resour. Res. 53, 10603-10618. https://doi.org/10.1002/2017WR021543

Comina, C., Lasagna, M., De Luca, D.A., Sambuelli, L., 2014. Geophysical methods to support correct water sampling locations for salt dilution gauging. Hydrol. Earth Syst. Sci. 18, 3195–3203. https://doi.org/10.5194/hess-18-3195-2014

Cook, H.F., Valdes, G.S.B., Lee, H.C., 2006. Mulch effects on rainfall interception, soil physical characteristics and temperature under Zea mays L. Soil Tillage Res. 91, 227–235. https://doi.org/10.1016/j.still.2005.12.007

Cousin, I., Nicoullaud, B., Coutadeur, C., 2003. Influence of rock fragments on the water retention and water percolation in a calcareous soil. Catena 53, 97–114. https://doi.org/10.1016/S0341-8162(03)00037-7

Croley T.E., 1982. Unsteady overland sedimentation. J. Hydrol. 56, 325-346. https://doi.org/10.1016/0022-1694(82)90021-X

D’Souza, V.P.C., Morgan, R.P.C., 1976. A laboratory study of the effect of slope steepness and curvature on soil erosion. J. Agric. Eng. Res. 21, 21–31. https://doi.org/10.1016/0021-8634(76)90095-0

Dane, J.H., Hopmans, J.W., 2002. Pressure plate extractor, in: Dane, J.H., Topp, G.C., (Eds.), Methods of Soil Analysis, Part 4, Physical Methods. SSSA Book Series 5, SSSA, Madison, WI, pp. 688–690.

de Figueiredo, T., Poesen, J., 1998. Effects of surface rock fragment characteristics on interrill runoff and erosion of a silty loam soil, in: Soil and Tillage Research. Elsevier B.V., pp. 81–95. https://doi.org/10.1016/S0167-1987(98)80110-4

de Lima, J.L.M.P., Abrantes, J.R.C.B., 2014a. Using a thermal tracer to estimate overland and rill flow velocities. Earth Surf. Process. Landforms 39. https://doi.org/10.1002/esp.3523

de Lima, J.L.M.P., Abrantes, J.R.C.B., 2014b. Can infrared thermography be used to estimate soil surface microrelief and rill morphology? Catena 113, 314–322. https://doi.org/10.1016/j.catena.2013.08.011

de Lima, R., Abrantes, J.R.C.B., de Lima, J.L.M.P., de Lima, M.I.P., 2015. Using thermal tracers to estimate flow velocities of shallow flows: laboratory and field experiments. J. Hydrol. Hydromechanics 63 (3), 255-262. https://doi.org/10.1515/johh-2015-0028

de Lima, J.L.M.P., Carvalho, S.C.P., P. de Lima, M.I., 2012. Rainfall simulator experiments on the importance o of when rainfall burst occurs during storm events on runoff and soil loss. Zeitschrift für Geomorphol. Suppl. Issues 57, 91–109. https://doi.org/10.1127/0372-8854/2012/s-00096

de Lima, J.L.M.P., Isidoro, J.M.G.P., de Lima, M.I.P., Singh, V.P., 2018. Longitudinal Hillslope Shape Effects on Runoff and Sediment Loss: Laboratory Flume Experiments. J. Environ. Eng. 144. https://doi.org/10.1061/(asce)ee.1943-7870.0001302

de Lima, J.L.M.P., Singh, V.P., 2002. The influence of the pattern of moving rainstorms on overland flow. Adv. Water Resour. 25, 817–828. https://doi.org/10.1016/S0309-1708(02)00067-2

de Lima, J.L.M.P., Singh, V.P., de Lima, M.I.P., 2003. The influence of storm movement on water erosion: Storm direction and velocity effects. Catena 52, 39–56. https://doi.org/10.1016/S0341-8162(02)00149-2

Deng, Z.Q., de Lima, J.L.M.P., Jung, H.S., 2008. Sediment transport rate-based model for rainfall-induced soil erosion. Catena. 76 (1), 54–62. https://doi.org/10.1016/j.catena.2008.09.005

Denis, A., Stevens, A., van Wesemael, B., Udelhoven, T., Tychon, B., 2014. Soil organic carbon assessment by field and airborne spectrometry in bare croplands: Accounting for soil surface roughness. Geoderma 226–227, 94–102. https://doi.org/10.1016/j.geoderma.2014.02.015

Dobriyal, P., Badola, R., Tuboi, C., Hussain, S.A., 2017. A review of methods for monitoring streamflow for sustainable water resource management. Appl. Water Sci. 7, 2617–2628. https://doi.org/10.1007/s13201-016-0488-y

Dobriyal, P., Qureshi, A., Badola, R., Hussain, S.A., 2012. A review of the methods available for estimating soil moisture and its implications for water resource management. J. Hydrol. 458–459, 110–117. https://doi.org/10.1016/j.jhydrol.2012.06.021

Dunkerley, D., 2001. Estimating the mean speed of laminar overland flow using dye injection uncertainty on rough surfaces. Earth Surf. Process. Landforms 26 (4), 363-374. https://doi.org/10.1002/esp.185

Efthimiou, N., Lykoudi, E., Psomiadis, E., 2020. Inherent relationship of the USLE, RUSLE topographic factor algorithms and its impact on soil erosion modelling. Hydrol. Sci. J. 65, 1879–1893. https://doi.org/10.1080/02626667.2020.1784423

Emmett, W.W., 1970. The hydraulics of overland flow on hill slope. US Geological Professional Paper 18, 662–668.

Flury, M., Wai, N.N., 2003. Dyes as tracers for vadose zone hydrology. Rev. Geophys. 41. https://doi.org/10.1029/2001RG000109

Foltz, R.B., Wagenbrenner, N.S., 2010. An evaluation of three wood shred blends for post-fire erosion control using indoor simulated rain events on small plots. Catena 80, 86–94. https://doi.org/10.1016/j.catena.2009.09.003

Foster, G.R., 2004. Terraces and Terracing, in: Encyclopedia of Soils in the Environment. Elsevier Inc., pp. 135–143. https://doi.org/10.1016/B0-12-348530-4/00249-6

Foster G.R., 1982. Modeling the erosion process, in: Haan C.T., Johnson H.P., Brakensiek D.C. (Eds), Hydrologic modeling of small watersheds. American Society for Agricultural Engineers 5, pp. 259-380.

Fuchs, N., Petrjanoff, I., 1937. Microscopic examination of fog-, cloud-and rain-droplets. Nature 139, 111–112. https://doi.org/10.1038/139111b0

Gabellani, S., Silvestro, F., Rudari, R., Boni, G., 2008. General calibration methodology for a combined Horton-SCS infiltration scheme in flash flood modeling. Nat. Hazards Earth Syst. Sci. 8. https://doi.org/10.5194/nhess-8-1317-2008

García Moreno, R., Saa Requejo, A., Tarquis Alonso, A.M., Barrington, S., Díaz, M.C., 2008. Shadow analysis: A method for measuring soil surface roughness. Geoderma 146, 201–208. https://doi.org/10.1016/j.geoderma.2008.05.026

Gholami, L., Sadeghi, S.H., Homaee, M., 2013. Straw Mulching Effect on Splash Erosion, Runoff, and Sediment Yield from Eroded Plots. Soil Sci. Soc. Am. J. 77, 268–278. https://doi.org/10.2136/sssaj2012.0271

Gilley, J.E., Kottwitz, E.R., 1996. Random roughness assessment by the pin and chain method. Appl. Eng. Agric. 12, 39–43.

Gilliot, J.M., Vaudour, E., Michelin, J., 2017. Soil surface roughness measurement: A new fully automatic photogrammetric approach applied to agricultural bare fields. Comput.

Electron. Agric. 134, 63–78. https://doi.org/10.1016/j.compag.2017.01.010

Gleason, J.R., 1999. An accurate, non-iterative approximation for studentized range quantiles. Comput. Stat. Data Anal. 31 (2), 147-158. https://doi.org/10.1016/S01679473(99)00002-X

Gómez, J.A., Nearing, M.A., 2005. Runoff and sediment losses from rough and smooth soil surfaces in a laboratory experiment. Catena 59, 253–266. https://doi.org/10.1016/j.catena.2004.09.008

Gordillo-Rivero, Á.J., García-Moreno, J., Jordán, A., Zavala, L.M., Granja-Martins, F.M., 2014. Fire severity and surface rock fragments cause patchy distribution of soil water repellency and infiltration rates after burning. Hydrol. Process. 28, 5832–5843. https://doi.org/10.1002/hyp.10072

Green, H.W., Ampt, G.A., 1911. Studies on soil physics: Flow of air and water through soils. J. Aric. Sci. 4, 11–24. https://doi.org/10.1017/S0021859600001441

Guo, T., Wang, Q., Li, D., Zhuang, J., 2010. Effect of surface stone cover on sediment and solute transport on the slope of fallow land in the semi-arid loess region of northwestern China. J. Soils Sediments 10, 1200–1208. https://doi.org/10.1007/s11368-010-0257-8

Han, Y., Fan, Y., Xin, Z., Wang, L., Cai, Q., Wang, X., 2016. Effects of wetting rate and simulated rain duration on soil crust formation of red loam. Environ. Earth Sci. 75, 1–9. https://doi.org/10.1007/s12665-015-4901-x

Han, Z., Wang, X., Song, D., Li, X., Huang, P., Ma, M., 2019. Response of soil erosion and sediment sorting to the transport mechanism on a steep rocky slope. Earth Surf. Process. Landforms 44, 2467–2478. https://doi.org/10.1002/esp.4675

Hansen, B., Schjønning, P., Sibbesen, E., 1999. Roughness indices for estimation of depression storage capacity of tilled soil surfaces. Soil Tillage Res. 52, 103–111. https://doi.org/10.1016/S0167-1987(99)00061-6

Hassan, Y.A., Blanchat, T.K., Seeley, C.H., 1992. PIV flow visualization using particle tracking techniques. Meas. Sci. Technol. 3, 633–642. http://dx.doi.org/10.1088/0957-0233/3/7/001

Herschy, R.W., 2008. Streamflow measurement: Third edition, Streamflow Measurement: Third Edition. CRC Press. https://doi.org/10.1201/9781482265880

Hlaváčiková, H., Holko, L., Danko, M., Novák, V., 2019. Estimation of macropore flow characteristics in stony soils of a small mountain catchment. J. Hydrol. 574, 1176–1187. https://doi.org/10.1016/j.jhydrol.2019.05.009

Hlaváčiková, H., Novák, V., Holko, L., 2014. On the role of rock fragments and initial soil water content in the potential subsurface runoff formation. J. Hydrol. Hydromechanics 63, 71–81. https://doi.org/10.1515/johh-2015-0002

Hlaváčiková, H., Novák, V., Kostka, Z., Danko, M., Hlavčo, J., 2018. The influence of stony soil properties on water dynamics modeled by the HYDRUS model. J. Hydrol. Hydromechanics 66, 181–188. https://doi.org/10.1515/johh-2017-0052

Hlaváčiková, H., Novák, V., Šimůnek, J., 2016. The effects of rock fragment shapes and positions on modeled hydraulic conductivities of stony soils. Geoderma 281, 39–48. https://doi.org/10.1016/j.geoderma.2016.06.034

Holko, L., Bičárová, S., Hlavčo, J., Danko, M., Kostka, Z., 2018. Isotopic hydrograph separation in two small mountain catchments during multiple events. Cuadernos de Investigación Geográfica 44 (2), 453-473. https://doi.org/10.18172/cig.3344

Holko, L., Sleziak, P. Danko, M., Bičárová, S., Pociask-Karteczka, J., 2020a. Analysis of changes in hydrological cycle of a pristine mountain catchment. 1. Hydrometric data. J. Hydrol. Hydromechanics 68(2), 180-191. https://doi.org/10.2478/johh-2020-0010

Holko, L., Danko, M., Sleziak, P., 2020b. Analysis of changes in hydrological cycle of a pristine mountain catchment. 2. Isotopic data, trend and attribution analyses. J. Hydrol. Hydromechanics 68(2), 192-199. https://doi.org/10.2478/johh-2020-0011

Holko, L., Kostka, Z., Šanda, M., 2011. Assessment of frequency and areal extent of overland flow generation in a forested mountain catchment. Soil Water Res. https://doi.org/10.17221/33/2010-swr

Holko L., Lepistő, A., 1997. Modelling the hydrological behaviour of a mountainous catchment using TOPMODEL. J. Hydrol. 196, 361–377. https://doi.org/10.1016/S0022-1694(96)03237-4

Holko, L., Kostka, Z., 2010. Hydrological processes in mountains – knowledge gained in the Jalovecky Creek catchment, Slovakia. IAHS Publication 336, 84–89.

Horton, R.E., 1941. An Approach Toward a Physical Interpretation of Infiltration-Capacity. Soil Sci. Soc. Am. J. 5. https://doi.org/10.2136/sssaj1941.036159950005000c0075x

Horton, R.E., 1933. The Rôle of infiltration in the hydrologic cycle. Eos, Trans. Am. Geophys. Union 14, 446–460. https://doi.org/10.1029/TR014i001p00446

Horton, R.E., Leach, H.R., Vliet, V.R., 1934. Laminar sheet flow. Transactions of the American Geophysical Union 15, 393–404. https://doi.org/10.1029/TR015i002p00393

Horton R.E., 1938. The interpretation and application of runoff plane plot experiments with reference to soil erosion problems. Soil Sci. Soc. Am. J. 1, 401-437. https://doi.org/10.2136/sssaj1939.036159950003000C0066x

Hosseini, M., Pelayo, O.G., Vasques, A., Ritsema, C., Geissen, V., Keizer, J.J., 2017. The short-term effectiveness of surfactant seed coating and mulching treatment in reducing post-fire runoff and erosion. Geoderma 307, 231–237. https://doi.org/10.1016/j.geoderma.2017.08.008

Hu, G.G.-R.G., Li, X.X.Y., 2019. Subsurface Flow, in: Li, X., Vereecken, H. (Eds.), Vereecken (Eds.), Observation and Measurement, Ecohydrology. Springer Berlin Heidelberg, Berlin, Heidelberg, pp. 1–23.

Huang, Y., Chen, X., Li, F., Zhang, J., Lei, T., Li, J., Chen, P., Wang, X., 2018. Velocity of water flow along saturated loess slopes under erosion effects. J. Hydrol. 561, 304–311. https://doi.org/10.1016/j.jhydrol.2018.03.070

Hudson, N.W., 1993. Field measurement of soil erosion and runoff. FAO Soils Bulletins, vol. 68. Silsoe Associates, Amptill, Bedford UK.

Isidoro J.M.G.P., de Lima J.L.M.P., 2013. An analytical closed form solution for 1D kinematic overland flow under moving rainstorms. J. Hydrol. Eng. 18, 1148–1156. https://doi.org/10.1061/(ASCE)HE.1943-5584.0000740

Issaka, S., Ashraf, M.A., 2017. Impact of soil erosion and degradation on water quality: a review. Geol. Ecol. Landscapes 1, 1–11. https://doi.org/10.1080/24749508.2017.1301053

Iverson, R.M., 1980. Processes of accelerated pluvial erosion on desert hillslopes modified by vehicular traffic. Earth Surf. Process. 5, 369–388. https://doi.org/10.1002/esp.3760050407

Jean, J.S., Ai, K.F., Shih, K., Hung, C.C., 2000. Stone cover and slope factors influencing hillside surface runoff and infiltration: Laboratory investigation. Hydrol. Process. 14, 1829–1849. https://doi.org/10.1002/1099-1085(200007)14:10<1829::aid-hyp66>3.0.co;2-%23

Jia, R., Gao, Y., Liu, L., Yang, H., Zhao, Y., 2020. Effect of sand burial on the subcritical water repellency of a dominant moss crust in a revegetated area of the Tengger Desert, Northern China. J. Hydrol. Hydromechanics 68, 279–284. https://doi.org/10.2478/johh-2020-0025

Jin, K., Cornelis, W.M., Gabriels, D., Baert, M., Wu, H.J., Schiettecatte, W., Cai, D.X., De Neve, S., Jin, J.Y., Hartmann, R., Hofman, G., 2009. Residue cover and rainfall intensity effects on runoff soil organic carbon losses. Catena 78, 81–86. https://doi.org/10.1016/j.catena.2009.03.001

Jodeau, M., Hauet, A., Paquier, A., Le Coz, J., Dramais, G., 2008. Application and evaluation of LS-PIV technique for the monitoring of river surface velocities in high flow conditions. Flow Meas. Instrum. 19, 117–127. https://doi.org/10.1016/j.flowmeasinst.2007.11.004

Jomaa, S., Barry, D.A., Brovelli, A., Heng, B.C.P., Sander, G.C., Parlange, J.Y., Rose, C.W., 2012a. Rain splash soil erosion estimation in the presence of rock fragments. Catena 92, 38–48. https://doi.org/10.1016/j.catena.2011.11.008

Jomaa, S., Barry, D.A., Heng, B.C.P., Brovelli, A., Sander, G.C., Parlange, J.Y., 2012b. Influence of rock fragment coverage on soil erosion and hydrological response: Laboratory flume experiments and modeling. Water Resour. Res. 48. https://doi.org/10.1029/2011WR011255

Jomaa, S., Barry, D.A., Heng, B.C.P., Brovelli, A., Sander, G.C., Parlange, J.Y., 2013. Effect of antecedent conditions and fixed rock fragment coverage on soil erosion dynamics through multiple rainfall events. J. Hydrol. 484, 115–127. https://doi.org/10.1016/j.jhydrol.2013.01.021

Jordán, A., Zavala, L.M., Gil, J., 2010. Effects of mulching on soil physical properties and runoff under semi-arid conditions in southern Spain. Catena 81, 77–85. https://doi.org/10.1016/j.catena.2010.01.007

Jung, Y.Y., Koh, D.C., Lee, J., Tsujimura, M., Yun, S.T., Lee, K.S., 2020. Mean transit time and subsurface flow paths in a humid temperate headwater catchment with granitic bedrock. J. Hydrol. 587, 124942. https://doi.org/10.1016/j.jhydrol.2020.124942

Kantoush, S.A., Schleiss, A.J., Sumi ,T., Murasaki, M., 2011. LSPIV implementation for environmental flow in various laboratory and field cases. J. Hydro-Environ. Res. 5, 263-276. https://doi.org/10.1016/j.jher.2011.07.002

Kathiravelu, G., Lucke, T., Nichols, P., 2016. Rain drop measurement techniques: A review. Water (Switzerland) 8, 29. https://doi.org/10.3390/w8010029

Katra, I., Lavee, H., Sarah, P., 2008. The effect of rock fragment size and position on topsoil moisture on arid and semi-arid hillslopes. Catena 72, 49–55. https://doi.org/10.1016/j.catena.2007.04.001

Kenny, L.B., Westendorf, M., Williams, C.A., 2018. Managing manure, erosion, and water quality in and around horse pastures, in: Sharpe, P. (Eds), Horse Pasture Management. Academic Press, pp. 245-259. https://doi.org/10.1016/B978-0-12-812919-7.00014-7

Kinnell, P.I.A., 2005. Raindrop-impact-induced erosion processes and prediction: A review. Hydrol. Process. 19, 2815–2844. https://doi.org/10.1002/hyp.5788

Koestel, J., Larsbo, M., Jarvis, N., 2020. Scale and REV analyses for porosity and pore connectivity measures in undisturbed soil. Geoderma 366, 114206. https://doi.org/10.1016/j.geoderma.2020.114206

Kostka, Z., 2009. Runoff response to rainfall event in the mountain catchment. Acta Hydrologica Slovaca 10(1), 130−139. (In Slovak with English abstract).

Lane L.J., Shirley E.D., 1985. Erosion and sediment yield equations: solutions for overland flow. In: Workshop on USLE Replacement, Natural Soil Erosion Laboratory, West Lafayette, Indiana, pp. 22.

Le Coz, J., Camenen, B., Peyrard, X., Dramais, G., 2012. Uncertainty in open-channel discharges measured with the velocity-area method. Flow Meas. Instrum. 26, 18–29. https://doi.org/10.1016/j.flowmeasinst.2012.05.001

Leelamanie, D.A.L., Nishiwaki, J., 2019. Water repellency in Japanese coniferous forest soils as affected by drying temperature and moisture. Biologia (Bratisl). 74, 127–137. https://doi.org/10.2478/s11756-018-0157-8

Lei, T., Xia, W., Zhao, J., Liu, Z., Zhang, Q., 2005. Method for measuring velocity of shallow water flow for soil erosion with an electrolyte tracer. Journal of Hydrology 301, 139–145. https://doi.org/10.1016/j.jhydrol.2004.06.025

Li, L., Nearing, M.A., Nichols, M.H., Polyakov, V.O., Larrabee Winter, C., Cavanaugh, M.L., 2020. Temporal and spatial evolution of soil surface roughness on stony plots. Soil Tillage Res. 200, 104526. https://doi.org/10.1016/j.still.2019.104526

Li, X.Y., 2003. Gravel-sand mulch for soil and water conservation in the semiarid loess region of northwest China. Catena. https://doi.org/10.1016/S0341-8162(02)00181-9

Li, X.Y., 2002. Effects of gravel and sand mulches on dew deposition in the semiarid region of China. J. Hydrol. 260, 151–160. https://doi.org/10.1016/S0022-1694(01)00605-9

Li, X.Y., Gong, J.D., Gao, Q.Z., Li, F.R., 2001. Incorporation of ridge and furrow method of rainfall harvesting with mulching for crop production under semiarid conditions. Agric. Water Manag. 50, 173–183. https://doi.org/10.1016/S0378-3774(01)00105-6

Li, H., Sivapalan, M., 2011. Effect of spatial heterogeneity of runoff generation mechanisms on the scaling behavior of event runoff responses in a natural river basin. Water Resour. Res. 47. https://doi.org/10.1029/2010WR009712

Li, G., Abrahams, A.D., 1997. Effect of saltating sediment load on the determination of the mean velocity of overland flow. Water Resour. Res. 33 (2), 341–347. https://doi.org/10.1029/96WR02937

Li, G., Abrahams, A.D., Atkinson, J.F., 1996. Correction factors in the determination of mean velocity of overland flow. Earth Surf. Process. Landforms 21, 509–515. https://doi.org/10.1002/(SICI)1096-9837(199606)21:6<509::AID-ESP613>3.0.CO;2-Z

Li, Z.B., Lu, X.K., Ding, F.W., 2002. Experimental study on dynamic processes of soil erosion on loess slope. J. Soil. Water Conserv. 16 (2), 5–7.

Liu, Q. Q., Xiang, H., Singh, V. P., 2006. A simulation model for unified interrill erosion and rill erosion on hillslopes. Hydrol. Process. 20, 469–486. https://doi.org/10.1002/hyp.5915

Liu, D., She, D., 2017. Can rock fragment cover maintain soil and water for saline-sodic soil slopes under coastal reclamation? Catena 151, 213–224. https://doi.org/10.1016/j.catena.2016.12.020

Loosvelt, L., 2007. Scale dependent influence of rock fragment cover on soil infiltration, runoff and sediment yield in arid zones of Chile (Doctoral Dissertation). Univeristy of Gent, Gent, Belgium.

Lopes V.L., 1987. A numerical model of watershed erosion and sediment yield (Doctoral Dissertation). University of Arizona, Tucson, USA.

Lopes V.L., Lane L.J., 1988. Modeling sedimentation processes in small watersheds. IAHS Publications 174, 497-508.

Lowe, E.J., 2007. Rain drops. Q. J. R. Meteorol. Soc. 18, 242–245. https://doi.org/10.1002/qj.4970188404

Lowe, M.A., McGrath, G., Leopold, M., 2021. The Impact of Soil Water Repellency and Slope upon Runoff and Erosion. Soil Tillage Res. 205, 104756. https://doi.org/10.1016/j.still.2020.104756

Lu, P., Xie, X., Wang, L., Wu, F., 2017. Effects of different spatial distributions of physical soil crusts on runoff and erosion on the Loess Plateau in China. Earth Surf. Process. Landforms 42, 2082–2089. https://doi.org/10.1002/esp.4175

Luk, S.H., Merz, W., 1992. Use of the salt tracing technique to determine the velocity of overland flow. Soil Technol. 5, 289–301.

Lv, J., Luo, H., Hu, J., Xie, Y., 2019. The effects of rock fragment content on the erosion processes of spoil heaps: a laboratory scouring experiment with two soils. J. Soils Sediments 19, 2089–2102. https://doi.org/10.1007/s11368-018-2193-y

Ma, D. H., Shao, M. A., 2008. Simulating infiltration into stony soils with a dual-porosity model. Eur. J. Soil Sci. 59, 950–959. https://doi.org/10.1111/j.1365-2389.2008.01055.x

Ma, D.H., Shao, M.A., Zhang, J.B., Wang, Q.J., 2010. Validation of an analytical method for determining soil hydraulic properties of stony soils using experimental data. Geoderma 159, 262–269. https://doi.org/10.1016/j.geoderma.2010.08.001

Ma, R.M., Li, Z.X., Cai, C.F., Wang, J.G., 2014. The dynamic response of splash erosion to aggregate mechanical breakdown through rainfall simulation events in Ultisols (subtropical China). Catena 121, 279-287. https://doi.org/10.1016/j.catena.2014.05.028

MacVicar, B.J., Beaulieu, E., Champagne, V., Roy, A.G., 2007. Measuring water velocity in highly turbulent flows: Field tests of an electromagnetic current meter (ECM) and an acoustic Doppler velocimeter (ADV). Earth Surf. Process. Landforms 32, 1412–1432. https://doi.org/10.1002/esp.1497

Mandal, U.K., Rao, K. V., Mishra, P.K., Vittal, K.P.R.R., Sharma, K.L., Narsimlu, B., Venkanna, K., 2005. Soil infiltration, runoff and sediment yield from a shallow soil with varied stone cover and intensity of rain. Eur. J. Soil Sci. 56, 435–443. https://doi.org/10.1111/j.1365-2389.2004.00687.x

Mao, J., Nierop, K.G.J., Rietkerk, M., Sinninghe Damsté, J.S., Dekker, S.C., 2016. The influence of vegetation on soil water repellency-markers and soil hydrophobicity. Sci. Total Environ. 566–567, 608–620. https://doi.org/10.1016/j.scitotenv.2016.05.077

Martinez-Zavala, L., Jordan, A., 2008. Effect of rock fragment cover on interrill soil erosion from bare soils in Western Andalusia, Spain. Soil Use Manage. 24, 108–117. doi:10.1111/j.1475-2743. 2007.00139.x.

Martínez-Mena, M., Carrillo-López, E., Boix-Fayos, C., Almagro, M., García Franco, N., Díaz-Pereira, E., Montoya, I., de Vente, J., 2020. Long-term effectiveness of sustainable land management practices to control runoff, soil erosion, and nutrient loss and the role of rainfall intensity in Mediterranean rainfed agroecosystems. Catena 187, 104352. https://doi.org/10.1016/j.catena.2019.104352

Mayor, Á.G., Bautista, S., Bellot, J., 2009. Factors and interactions controlling infiltration, runoff, and soil loss at the microscale in a patchy Mediterranean semiarid landscape. Earth Surf. Process. Landforms 34, 1702–1711. https://doi.org/10.1002/esp.1875

Mehta A.J., 1983. Characterization tests for cohesive sediments. In: Proc. of the Conference on Frontiers in Hydraulic Engineering. ASCE/MIT, Cambridge, Mass, pp. 79-84.

Mehuys, G.R., Stolzy, L.H., Letey, J., 1975. Temperature distributions under stones submitted to a diurnal heat wave. Soil Sci. 437–441. https://doi.org/10.1097/00010694-197512000-00005

Merritt, W.S., Letcher, R.A., Jakeman, A.J., 2003. A review of erosion and sediment transport models. Environ. Model. Softw. 18, 761–799. https://doi.org/10.1016/S1364-8152(03)00078-1

Mohammed, S., Alsafadi, K., Talukdar, S., Kiwan, S., Hennawi, S., Alshihabi, O., Sharaf, M., Harsanyie, E., 2020. Estimation of soil erosion risk in southern part of Syria by using RUSLE integrating geo informatics approach. Remote Sens. Appl. Soc. Environ. 20, 100375. https://doi.org/10.1016/j.rsase.2020.100375

Montenegro, A.A.A., Abrantes, J.R.C.B., De Lima, J.L.M.P., Singh, V.P., Santos, T.E.M., 2013. Impact of mulching on soil and water dynamics under intermittent simulated rainfall. Catena 109, 139–149. https://doi.org/10.1016/j.catena.2013.03.018

Mujtaba, B., de Lima, J.L.M.P., 2018. Laboratory testing of a new thermal tracer for infrared-based PTV technique for shallow overland flows. Catena 169, 69-79. https://doi.org/10.1016/j.catena.2018.05.030

Mujtaba, B., Hlaváčiková, H., Danko, M., De Lima, J.L.M.P., Holko, L., 2020. The role of stony soils in hillslope and catchment runoff formation. J. Hydrol. Hydromechanics 68(2), 144–154. https://doi.org/10.2478/johh-2020-0012

Mujtaba B., de Lima J.L.M.P., de Lima M.I.P., Vargas M.M., 2019. Importance of the hydraulics of converging and diverging flows on soil erosion override effects of rock fragment cover patterns: experimental assessment. Zeitschrift für Geomorphol. 62, 183–197. https://doi.org/10.1127/zfg/2019/0578

Mupangwa, W., Twomlow, S., Walker, S., Hove, L., 2007. Effect of minimum tillage and mulching on maize (Zea mays L.) yield and water content of clayey and sandy soils. Phys. Chem. Earth 32, 1127–1134. https://doi.org/10.1016/j.pce.2007.07.030

Nachtergaele, J., Poesen, J., Van Wesemael, B., 1998. Gravel mulching in vineyards of southern Switzerland. Soil Tillage Res. 46, 51–59. https://doi.org/10.1016/S0167-1987(98)80107-4

Nearing, M. A., Norton, L.D., Bulgakov, D.A., Larionov, G.A., West, L.T., Dontsova, K.M., 1997. Hydraulics and erosion in eroding rills. Water Resour. Res. 33(4), 865-876.

https://doi.org/10.1029/97WR00013

Nearing, M.A., Yin, S. qing, Borrelli, P., Polyakov, V.O., 2017. Rainfall erosivity: An historical review. Catena 157, 357-362. https://doi.org/10.1016/j.catena.2017.06.004

Nikora, V., Nokes, R., Veale, W., Davidson, M., Jirka, G.H. 2007. Large-scale turbulent structure of uniform shallow free-surface flows. Environ. Fluid Mech. 7, 159-172. https://doi.org/10.1007/s10652-007-9021-z

Novák, V., Kňava, K., Šimůnek, J., 2011. Determining the influence of stones on hydraulic conductivity of saturated soils using numerical method. Geoderma 161, 177–181. https://doi.org/10.1016/j.geoderma.2010.12.016

Ohmi, K., Li, H., 2000. Particle tracking velocimetry with new algorithms. Measurement Science and Technology 11 (6), 603–616.

Pan, C., Shangguan, Z., 2006. Runoff hydraulic characteristics and sediment generation in sloped grassplots under simulated rainfall conditions. J. Hydrol. 331, 178–185. https://doi.org/10.1016/j.jhydrol.2006.05.011

Pannkuk, C.D., Robichaud, P.R., 2003. Effectiveness of needle cast at reducing erosion after forest fires. Water Resour. Res. 39. https://doi.org/10.1029/2003WR002318

Papierowska, E., Szatyłowicz, J., Ruta, M., Łachacz, A., Gnatowski, T., Stańczyk, T., 2020. Water repellency of soils on unpaved roads in coniferous forests. Catena 195, 104784. https://doi.org/10.1016/j.catena.2020.104784

Philip, J.R., 1957. The theory of infiltration: 1. The infiltration equation and its solution. Soil Sci. 83, 345–358. https://doi.org/10.1097/00010694-195705000-00002

Planchon, O., Esteves, M., Silvera, N., Lapetite, J.M., 2000. Raindrop erosion of tillage induced microrelief: Possible use of the diffusion equation. Soil Tillage Res. 56, 131–144. https://doi.org/10.1016/S0167-1987(00)00134-3

Poesen, J., Ingelmo-Sanchez, F., Mucher, H., 1990. The hydrological response of soil surfaces to rainfall as affected by cover and position of rock fragments in the top layer. Earth Surf. Process. Landforms 15, 653–671. https://doi.org/10.1002/esp.3290150707

Poesen, J.W.A., Lavee, H., 1991. Effects of size and incorporation of synthetic mulch on runoff and sediment yield from interrils in a laboratory study with simulated rainfall. Soil Tillage Res. 21, 209–223. https://doi.org/10.1016/0167-1987(91)90021-O

Poesen, J., Ingelmo-Sanchez, F., 1992. Runoff and sediment yield from topsoils with different porosity as affected by rock fragment cover and position, Catena. 19(5), 451–474. doi:10.1016/0341-8162(92)90044-C.

Prats, S., Abrantes, J.R.C.B., Crema, I.P., Keizer, J.J., de Lima, J.L.M.P., 2015. Testing the effectiveness of three forest residue mulch application schemes for reducing post-fire runoff and soil erosion using indoor simulated rain. FLAMMA 6, 113–116.

Prats, S.A., Abrantes, J.R., Crema, I.P., Keizer, J.J., de Lima, J.L., 2017. Runoff and soil erosion mitigation with sieved forest residue mulch strips under controlled laboratory conditions. For. Ecol. Manage. 396, 102–112. https://doi.org/10.1016/j.foreco.2017.04.019

Ran, Q., Su, D., Li, P., He, Z., 2012. Experimental study of the impact of rainfall characteristics on runoff generation and soil erosion. J. Hydrol. 424–425, 99–111. https://doi.org/10.1016/j.jhydrol.2011.12.035

Ran, Q., Wang, F., Li, P., Ye, S., Tang, H., Gao, J., 2018. Effect of rainfall moving direction on surface flow and soil erosion processes on slopes with sealing. J. Hydrol. 567, 478–488. https://doi.org/10.1016/j.jhydrol.2018.10.047

Richards, L.A., 1931. Capillary conduction of liquids through porous mediums. J. Appl. Phys. 1, 318–333. https://doi.org/10.1063/1.1745010

Rieke-Zapp, D.H., Nearing, M.A., 2005. Slope Shape Effects on Erosion. Soil Sci. Soc. Am. J. 69, 1463-1471. https://doi.org/10.2136/sssaj2005.0015

Robichaud, P.R., Wagenbrenner, J.W., Pierson, F.B., Spaeth, K.E., Ashmun, L.E., Moffet, C.A., 2016. Infiltration and interrill erosion rates after a wildfire in western Montana, USA. Catena 142, 77–88. https://doi.org/10.1016/j.catena.2016.01.027

Rodrigo-Comino, J., García-Díaz, A., Brevik, E.C., Keestra, S.D., Pereira, P., Novara, A., Jordán, A., Cerdà, A., 2017. Role of rock fragment cover on runoff generation and sediment yield in tilled vineyards. Eur. J. Soil Sci. 68, 864–872. https://doi.org/10.1111/ejss.12483

Römkens, M.J.M., Helming, K., Prasad, S.N., 2002. Soil erosion under different rainfall intensities, surface roughness, and soil water regimes. Catena 46,103–123. https://doi.org/10.1016/S0341-8162(01)00161-8

Roundy, B.A., Abbott, L.B., Livingston, M., 1997. Surface soil water loss after summer rainfall in a semidesert grassland. Arid Soil Res. Rehabil. 11, 49–62. https://doi.org/10.1080/15324989709381458

Ruiz-Sinoga, J. D., Romero-Diaz, A., Ferre-Bueno, E., Martínez-Murillo, J. F., 2010. The role of soil surface conditions in regulating runoff and erosion processes on a metamorphic hillslope (southern Spain) soil surface conditions, runoff and erosion in southern Spain. Catena. 80, 131–139. https://doi.org/10.1016/j.catena.2009.09.007

Ruy, S., Findeling, A., Chadoeuf, J., 2006. Effect of mulching techniques on plot scale runoff: FDTF modeling and sensitivity analysis. J. Hydrol., 326, 277–294. https://doi.org/10.1016/j.jhydrol.2005.11.003

Sabzevari, T., Noroozpour, S., 2014. Effects of hillslope geometry on surface and subsurface flows. Hydrogeol. J. 22, 1593–1604. https://doi.org/10.1007/s10040-014-1149-6

Sabzevari, T., Saghafian, B., Talebi, A., Ardakanian, R., 2013. Time of concentration of surface flow in complex hillslopes. J. Hydrol. Hydromechanics 61, 269–277. https://doi.org/10.2478/johh-2013-0034

Sabzevari, T., Talebi, A., 2019. Effect of hillslope topography on soil erosion and sediment yield using USLE model. Acta Geophys. 67, 1587–1597. https://doi.org/10.1007/s11600-019-00361-8

Saleh, A., 1993. Soil roughness measurement: chain method. J. Soil Water Conserv. 48(6), 527–529.

Salem, H.M., Meselhy, A.A., 2021. A portable rainfall simulator to evaluate the factors affecting soil erosion in the northwestern coastal zone of Egypt. Nat. Hazards 105, 2937–2955. https://doi.org/10.1007/s11069-020-04432-8

Saretta, E., de Camargo, A.P., Botrel, T.A., Pinto, M.F., Katsurayama, G.T., Frizone, J.A., 2016. Development and evaluation of an automated system for testing current meters. Rev. Bras. Eng. Agric. e Ambient. 20, 181–187. https://doi.org/10.1590/1807-1929/agriambi.v20n2p181-187

Salter, P.J., Haworth, F., 1961. The available-water capacity of a sandy loam soil. J. Soil Sci. 12, 335–342. doi:10.1111/j.1365-2389.1961.tb00923.x

Scherer, U., Zehe, E., Träbing, K., Gerlinger, K., 2012. Prediction of soil detachment in agricultural loess catchments: Model development and parameterisation. Catena 90, 63–75. https://doi.org/10.1016/j.catena.2011.11.003

Schuetz, T., Weiler, M., Lange, J., Stoelzle, M., 2012. Two-dimensional assessment of solute transport in shallow waters with thermal imaging and heated water. Adv. Water Resour. 43, 67-75. https://doi.org/10.1016/j.advwatres.2012.03.013

Sela, S., Svoray, T., Assouline, S., 2012. Soil water content variability at the hillslope scale: Impact of surface sealing. Water Resour. Res. 48, W03522. https://doi.org/10.1029/2011WR011297

Shi, Z.J., Wang, Y.H., Yu, P.T., Xu, L.H., Xiong, W., Guo, H., 2008. Effect of rock fragments on the percolation and evaporation of forest soil in the Liupan Mountains, China. Shengtai Xuebao/ Acta Ecol. Sin. 28, 6090–6098. https://doi.org/10.1016/s1872-2032(09)60014-7

Sidorchuk, A., Schmidt, J., Cooper G., 2008. Variability of shallow flow velocity and soil aggregate transport observed with digital videography. Hydrol. Process. 22, 4035–4048. https://doi.org/10.1002/hyp.7006

Šimůnek, J., van Genuchten, M. T., 1996. Estimating unsaturated soil hydraulic properties from tension disc infiltrometer data by numerical inversion. Water Resour. Res. 32, 2683 – 2696. https://doi.org/10.1029/96WR01525

Šimůnek, J., Wendroth, O., van Genuchten, M. T., 1998. A parameter estimation analysis of the evaporation method for determining soil hydraulic properties. Soil Sci. Soc. Amer. J. 62, 894 – 905.

Šimůnek, J., Šejna, M., Saito, H., Sakai, M., van Genuchten, M. T., 2013. The HYDRUS-1D Software Package for Simulating the One-Dimensional Movement of Water, Heat, and Multiple Solutes in Variably-Saturated Media (Version 4.17). Department of Environmental Sciences, University of California Riverside, Riverside, CA, USA, pp. 308.

Šimůnek, J., van Genuchten, M.T., Šejna, M., 2008. Development and applications of the HYDRUS and STANMOD software packages and related codes. Vadose Zone J. 7, 587–600. https://doi.org/10.2136/vzj2007.0077

Singh V.P., 1996. Kinematic Wave Modelling in Water Resources: Surface-Water Hydrology. John Wiley and Sons Ltd, Chichester, UK.

Smets, T., Poesen, J., Bochet, E., 2008. Impact of plot length on the effectiveness of different soil-surface covers in reducing runoff and soil loss by water. Prog. Phys. Geogr**.** (32), 654–677. https://doi.org/10.1177/0309133308101473

Smets, T., López-Vicente, M., Poesen, J., 2011. Impact of subsurface rock fragments on runoff and interrill soil loss from cultivated soils. Earth Surf. Process. Landforms. https://doi.org/10.1002/esp.2220

Smith, R.E., 1972. The infiltration envelope: Results from a theoretical infiltrometer. J. Hydrol. 17, 1–22. https://doi.org/10.1016/0022-1694(72)90063-7

Smith, R.E., Parlange, J. -Y, 1978. A parameter-efficient hydrologic infiltration model. Water Resour. Res. 14, 533–538. https://doi.org/10.1029/WR014i003p00533

Smith R.E., Goodrich D.C., Woolhiser D.A., Unkrich C.L., 1995. KINEROS - a kinematic runoff and erosion model, in: Singh V.P. (Eds), Computer models of watershed hydrology. Water Resources Publications, pp. 697-732.

Souza, E.S., Antonino, A.C.D., Heck, R.J., Montenegro, S.M.G.L., Lima, J.R.S., Sampaio, E.V.S.B., Angulo-Jaramillo, R., Vauclin, M., 2014. Effect of crusting on the physical and hydraulic properties of a soil cropped with Castor beans (Ricinus communis L.) in the northeastern region of Brazil. Soil Tillage Res. 141, 55–61. https://doi.org/10.1016/j.still.2014.04.004

Stenberg, L., Tuukkanen, T., Finér, L., Marttila, H., Piirainen, S., Kløve, B., Koivusalo, H., 2016. Evaluation of erosion and surface roughness in peatland forest ditches using pin meter measurements and terrestrial laser scanning. Earth Surf. Process. Landforms 41, 1299–1311. https://doi.org/10.1002/esp.3897

Takehara, K., Etoh, T., 1998. A study on particle identification in PTV particle mask correlation method. J. Vis. 1 (3), 313–323. https://doi.org/10.1007/BF03181412

Talebi, A., Troch, P.A., Uijlenhoet, R., 2008. A steady-state analytical slope stability model for complex hillslopes. Hydrol. Process. 22, 546–553. https://doi.org/10.1002/hyp.6881

Tatard, L., Planchon, O., Wainwright, J., Nord, G., Favis-Mortlock, D., Silvera, N., Ribolzi, O., Esteves, M., Huang, C.H., 2008. Measurement and modelling of high-resolution flow-velocity data under simulated rainfall on a low-slope sandy soil. J. Hydrol. 348, 1–12. https://doi.org/10.1016/j.jhydrol.2007.07.016

Tauro, F., Grimaldi, S., 2017. Ice dices for monitoring stream surface velocity. J. Hydro-Environment Res. 14, 143–149. https://doi.org/10.1016/j.jher.2016.09.001

Tauro, F., Piscopia, R., Grimaldi, S., 2017. Streamflow Observations From Cameras: Large-Scale Particle Image Velocimetry or Particle Tracking Velocimetry? Water Resour. Res. 53, 10374–10394. https://doi.org/10.1002/2017WR020848

Tauro, F., Grimaldi, S., Petroselli, A., Rulli, M.C., Porfiri, M., 2012. Fluorescent particle tracer for surface flow measurements: a proof of concept in a semi-natural hillslope. Hydrol. Earth Syst. Sci. 16, 2973-2983. https://doi.org/10.5194/hess-16-2973-2012

Tesař, M., Šír, M., Syrovátka, O., Pražák, J., Lichner, Ľ., Kubík, F., 2001. Soil water regime in head water regions - observation, assessment and modelling. J. Hydrol. Hydromechanics 49, 355–375.

Tetegan, M., Pasquier, C., Besson, A., Nicoullaud, B., Bouthier, A., Bourennane, H., Desbourdes, C., King, D., Cousin, I., 2012. Field-scale estimation of the volume percentage of rock fragments in stony soils by electrical resistivity. Catena 92, 67–74. https://doi.org/10.1016/j.catena.2011.09.005

Torri, D., Poesen, J., Monaci, F., Busoni, E., 1994. Rock fragment content and fine soil bulk density. Catena 23, 65–71. https://doi.org/10.1016/0341-8162(94)90053-1

Tromp-Van Meerveld, H.J., McDonnell, J.J., 2006a. Threshold relations in subsurface stormflow: 1. A 147-storm analysis of the Panola hillslope. Water Resour. Res. 42, W02410. https://doi.org/10.1029/2004WR003778

Tromp-Van Meerveld, H.J., McDonnell, J.J., 2006b. Threshold relations in subsurface stormflow: 2. The fill and spill hypothesis. Water Resour. Res. 42, W02411. https://doi.org/10.1029/2004WR003800

Tromp-Van Meerveld, H.J., Parlange, J.-Y.Y., Barry, D.A., Tromp, M.F., Sander, G.C., Walter, M.T., Parlange, M.B., 2008. Influence of sediment settling velocity on mechanistic soil erosion modeling. Water Resour. Res. 44, W06401. https://doi.org/10.1029/2007WR006361

Turton, D.J., Haan, C.T., Miller, E.L., 1992. Subsurface flow responses of a small forested catchment in the Ouachita mountains. Hydrol. Process. 6, 111–125. https://doi.org/10.1002/hyp.3360060110

Uemura, T., Yamamoto, F., Ohmi, K., 1989. High-speed algorithm of image analysis for real time measurement of a two-dimensional velocity distribution. Flow visualization ASME FED 85, 129–134.

Uijttewaal, W.S.J., Jirka, G.H., 2003. Grid turbulence in shallow flows. J. Fluid Mech. 489, 325–344. https://doi.org/10.1017/S0022112003005020

Valentin, C., 1994. Surface sealing as affected by various rock fragment covers in West Africa. Catena 23, 87–97. https://doi.org/10.1016/0341-8162(94)90055-8

vanGenuchten, M.T., 1980. A closed-form equation for predicting the hydraulic conductivity of unsaturated soils. Soil Sci. Soc Am. J. 44, 987–996. https://doi.org/10.2136/sssaj1980.03615995004400050002x

Verbist, K.M.J., Cornelis, W.M., Torfs, S., Gabriels, D., 2013. Comparing Methods to Determine Hydraulic Conductivities on Stony Soils. Soil Sci. Soc. Am. J. 77, 25–42. https://doi.org/10.2136/sssaj2012.0025

Vermang, J., Norton, L.D., Huang, C., Cornelis, W.M., da Silva, A.M., Gabriels, D., 2015. Characterization of Soil Surface Roughness Effects on Runoff and Soil Erosion Rates under Simulated Rainfall. Soil Sci. Soc. Am. J. 79, 903–916. https://doi.org/10.2136/sssaj2014.08.0329

Wang, C., Wang, B., Wang, Yunqi, Wang, Yujie, Zhang, W., Yan, Y., 2020. Impact of near-surface hydraulic gradient on the interrill erosion process. Eur. J. Soil Sci. 71, 598– 614. https://doi.org/10.1111/ejss.12905

Wang, X., Li, Z., Cai, C., Shi, Z., Xu, Q., Fu, Z., Guo, Z., 2012. Effects of rock fragment cover on hydrological response and soil loss from Regosols in a semi-humid environment in South-West China. Geomorphology 151–152, 234–242. https://doi.org/10.1016/j.geomorph.2012.02.008

Wegehenkel, M., Wagner, A., Amoriello, T., Fleck, S., Messenburg, H., 2017. Impact of stoniness correction of soil hydraulic parameters on water balance simulations of forest plots. J. Plant Nutr. Soil Sci. 180, 71–86. https://doi.org/10.1002/jpln.201600244

Weitbrecht, V., Kuhn, G., Jirka G.H., 2002. Large scale PIV-measurements at the surface of shallow water flows. Flow Meas. Instrum. 13, 237–45. https://doi.org/10.1016/S0955-5986(02)00059-6

Weiler, M., McDonnell, J.J., Tromp-Van Meerveld, I., Uchida, T., 2006. Subsurface Stormflow, in: Anderson, M.G., McDonnell, J.J. (Eds), Encyclopedia of Hydrological Sciences. John Wiley & Sons, pp. 1–14. https://doi.org/10.1002/0470848944.hsa119

Weninger, T., Filipović, V., Mešić, M., Clothier, B., Filipović, L., 2019. Estimating the extent of fire induced soil water repellency in Mediterranean environment. Geoderma 338, 187–196. https://doi.org/10.1016/j.geoderma.2018.12.008

Wilcox, B. P., Wood, M. K., Tromble, J. M., 1988. Factors influencing infiltrability of semiarid mountain slopes, J. Range Manage. 41, 197-206. https://doi.org/10.2307/3899167

Wilcox, B.P., Newman, B.D., Brandes, D., Davenport, D.W., Reid, K., 1997. Runoff from a semiarid ponderosa pine hillslope in New Mexico. Water Resour. Res. 33(10), 2301–2314. https://doi.org/10.1029/97WR01691

Winder, P., Paulson, K.S., 2012. The measurement of rain kinetic energy and rain intensity using an acoustic disdrometer. Meas. Sci. Technol. 23, 15801. https://doi.org/10.1088/0957-0233/23/1/015801

Winder, P.N., Paulson, K.S., 2013. Direct and indirect measurement of rain drop size distributions using an acoustic water tank disdrometer. Meas. Sci. Technol. 24, 65801–65812. https://doi.org/10.1088/0957-0233/24/6/065801

Wirtz, S., Seeger, M., Ries, J.B., 2012. Field experiments for understanding and quantification of rill erosion process. CATENA 91, 21-34. https://doi.org/10.1016/j.catena.2010.12.002

Woche, S.K., Goebel, M.O., Kirkham, M.B., Horton, R., Van Der Ploeg, R.R., Bachmann, J., 2005. Contact angle of soils as affected by depth, texture, and land management. Eur. J. Soil Sci. 56, 239–251. https://doi.org/10.1111/j.1365-2389.2004.00664.x

Wu, B., Wang, Z., Zhang, Q., Shen, N., 2018. Distinguishing transport-limited and detachment-limited processes of interrill erosion on steep slopes in the Chinese loessial region. Soil Tillage Res. 177, 88-96. https://doi.org/10.1016/j.still.2017.12.005

Wu, Q., Wang, L., Wu, F., 2016. Effects of structural and depositional crusts on soil erosion on the Loess Plateau of China. Arid L. Res. Manag. 30, 432–444. https://doi.org/10.1080/15324982.2016.1157837

Wu, S., Chen, L., Wang, N., Li, Jing, Li, Jiake, 2020. Two-dimensional rainfall-runoff and soil erosion model on an irregularly rilled hillslope. J. Hydrol. 580, 124346. https://doi.org/10.1016/j.jhydrol.2019.124346

Wu, Y.S., Li, X.R., Hasi-Eerdun, Yin, R.P., Liu, T.J., 2020. Surface roughness response of biocrust-covered soil to mimicked sheep trampling in the Mu Us sandy Land, northern China. Geoderma 363, 114146. https://doi.org/10.1016/j.geoderma.2019.114146

Wu, Q., Pairman, D., 1995. A relaxation labeling technique for computing sea surface velocities from sea surface temperature. IEEE Trans. Geosci. Remote Sens. 33, 216–220. https://doi.org/10.1109/36.368206.

Xia, L., Song, X., Fu, N., Cui, S., Li, L., Li, H., Li, Y., 2018. Effects of rock fragment cover on hydrological processes under rainfall simulation in a semi-arid region of China. Hydrol. Process. 32, 792–804. https://doi.org/10.1002/hyp.11455

Xiao, H., Liu, G., Abd-Elbasit, M.A.M., Zhang, X.C., Liu, P.L., Zheng, F.L., Zhang, J.Q., Hu, F.N., 2017. Effects of slaking and mechanical breakdown on disaggregation and splash erosion. Eur. J. Soil Sci. 68, 797–805. https://doi.org/10.1111/ejss.12482

Yan, L., Lei, T., Zhang, J., Zhang, Q., Liqin, Q., 2015. Finite element method for one-dimensional rill erosion simulation on a curved slope. Int. Soil Water Conserv. Res. 3, 28– 41. https://doi.org/10.1016/j.iswcr.2015.03.001

Yang, D.M., Fang, N.F., Shi, Z.H., 2020. Correction factor for rill flow velocity measured by the dye tracer method under varying rill morphologies and hydraulic characteristics. J. Hydrol. 591, 125560. https://doi.org/10.1016/j.jhydrol.2020.125560

Young, R.A., Mutchler, C.K., 1969. Soil movement on irregular slopes. Water Resour. Res. 5(5), 1084– 1089. https://doi.org/10.1029/WR005i005p01084

Young, R.A., Onstad, C.A., Bosch, D.D., Anderson, W.P., 1989. AGNPS: A nonpoint-source pollution model for evaluating agricultural watersheds. J. Soil Water Conserv. 44, 168-173.

Zambon, N., Johannsen, L.L., Strauss, P., Dostal, T., Zumr, D., Cochrane, T.A., Klik, A., 2021. Splash erosion affected by initial soil moisture and surface conditions under simulated rainfall. Catena 196, 104827. https://doi.org/10.1016/j.catena.2020.104827

Zavala, L.M., Jordán, A., Bellinfante, N., GIL, J., 2010. Relationships between rock fragment cover and soil hydrological response in a Mediterranean environment. Soil Sci. Plant Nutr. 56, 95–104. https://doi.org/10.1111/j.1747-0765.2009.00429.x

Zhang, Q., Lei, T., Zhao, J., 2008. Estimation of the detachment rate in eroding rills in flume experiments using an REE tracing method. Geoderma 147, 8-15. https://doi.org/10.1016/j.geoderma.2008.07.002

Zhang, X.C. J., Zheng, F.L., Chen, J., Garbrecht, J.D., 2020. Characterizing detachment and transport processes of interrill soil erosion. Geoderma 376, 114549. https://doi.org/10.1016/j.geoderma.2020.114549

Zhang, G.H., Luo, R.T., Cao, Y., Shen, R.S., Zhang, X.C., 2010. Correction factor to dye-measured flow velocity under varying water and sediment discharges. J. Hydrol. 389, 205–213. https://doi.org/10.1016/j.jhydrol.2010.05.050

Zhao, L., Huang, C., Wu, F., 2016. Effect of microrelief on water erosion and their changes during rainfall. Earth Surf. Process. Landforms 41, 579–586. https://doi.org/10.1002/esp.3844

Zhongjie, S., Lihong, X., Yanhui, W., Xiaohui, Y., Zhiqing, J., Hao, G., Wei, X., Pengtao, Y., Zhongjie Shi, 2012. Effect of rock fragments on macropores and water effluent in a forest soil in the stony mountains of the Loess Plateau, China. African J. Biotechnol. 11, 9350-9361. https://doi.org/10.5897/ajb12.145

Zhou, H., Peng, X., Darboux, F., 2013. Effect of Rainfall Kinetic Energy on Crust Formation and Interrill Erosion of an Ultisol in Subtropical China. Vadose Zo. J. 12, 1-9. https://doi.org/10.2136/vzj2013.01.0010

Zonta, J.H., Martinez, M.A., Pruski, F.F., da Silva, D.D., dos Santos, M.R., 2012. Efeito da Aplicação Sucessiva de Precipitações pluviais com Diferentes Perfis na Taxa de Infiltração de Água no Solo. Rev. Bras. Cienc. do Solo 36, 377–388. https://doi.org/10.1590/S0100-06832012000200007